From Binary to Ternary Fluid Systems

ALVIN CHEE MING SHEK

From Binary to Ternary Fluid Systems

Alvin Chee Ming Shek

A thesis presented for the degree of

Doctor of Philosophy

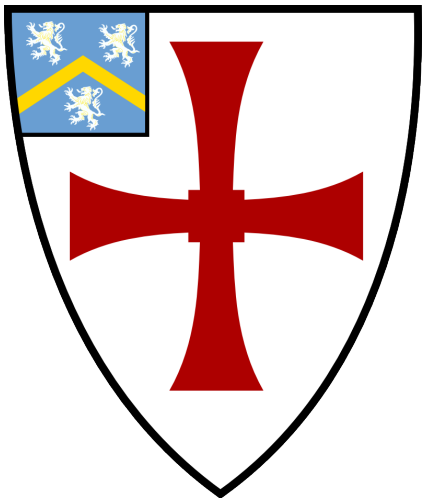

Soft Matter and Functional Interfaces Centre for Doctoral Training

The University of Durham

United Kingdom

29th September 2022

From Binary to Ternary Fluid Systems

Alvin Chee Ming Shek

Abstract

This thesis focuses on key interfacial phenomena where the presence of three fluid phases or components lead to new effects which are absent in their binary system equivalents. We study three ternary fluid phenomena related to the formation of capillary bridges, de-wetting of droplets and phase separation of mixtures.

Firstly, we numerically study two-component capillary bridges formed when a liquid droplet is placed in between two liquid-infused surfaces (LIS). Two-component liquid bridges can exhibit a range of different morphologies where the liquid droplet is directly in contact with two, one, or none of the LIS substrates. We also characterize the capillary force, maximum separation, and effective spring constant and find that they are influenced by the shape and size of the lubricant ridge. Importantly, we argue that LIS are not only "slippery" parallel to the surface, but they are also "sticky" perpendicular to the surface.

Secondly, we investigate a novel de-wetting phenomenon whereby droplet lift-off is driven by an incoming film of another immiscible liquid. This mechanism exploits the lifting force arising from the triple contact line between the droplet, film and surrounding air. We find droplet detachment from the substrate can occur with film thickness that is comparable to the droplet size. As such, we believe this mechanism is potentially interesting for developing a sustainable and more environmentally friendly way to clean.

Thirdly, we explore the spontaneous phase separation of ternary fluid mixtures, both when all the surface tensions are equal and when they have different values. By combining systematic computer simulations over the full range of the composition space and theoretical analysis on the eigenvalues

and eigenvectors of the unstable modes, here we identify four fundamental phase separation pathways. In particular, we highlight a dominant but so-far overlooked mechanism involving enrichment and instability of the minor component at the fluid-fluid interface.

Another key contribution of the thesis is the development of suitable computational schemes for modelling ternary fluids, required to pursue the phenomena described above. Here, we employ a combination of Surface Evolver and Lattice Boltzmann Method.

Acknowledgements

I first must thank my supervisor Prof. Halim Kusumaatmaja who introduced me to the group and guided me through the PhD. I must also thank several of my colleagues during my time here from the Soft Matter Group in Durham Physics, in particular Dr. Jack Panter, who also contributed to some of the work in this thesis, Dr. Ningning Wang, who developed some of the numerical methods used in this thesis, Dr. Marianna Pepona who I collaborated with for work not presented in this thesis, Dr. Hugh Barlow, Clara Despard and Raymond Christianto for enlightened discussions. Furthermore I must thank Dr. Ciro Semprebon of Northumbria University, who guided me through the use of Surface Evolver. I also thank Dr. Yonas Gizaw and Dr. Steve Page from Procter and Gamble who in collaboration develop new ideas to explore and develop, especially our work presented here on Ternary De-Wetting. Finally, I must acknowledge the Soft Matter and Functional Interfaces Centre for Doctoral Training, without which I would not had had the opportunity to study for my PhD.

Contributions

Chapter 4 Ternary De-Wetting was pursued in collaboration with Dr. Jack Panter. For completeness and clarity of the scientific narrative, I chose to present all the results in this thesis. To be more precise the sections and subsections have been labelled previous result for the work done primarily by Dr. Jack Panter. The results captured in figures below were mainly done by Dr. Jack Panter:

- Fig. 4.2
- Fig. 4.3
- Fig. 4.4
- Fig. 4.5
- Fig. 4.6

Contents

Declaration

The work in this thesis is based on research carried out at the Department of Physics, University of Durham, England. No part of this thesis has been submitted elsewhere for any other degree or qualification, and it is the sole work of the author unless referenced to the contrary in the text.

Some of the work presented in this thesis has been published in journals and conference proceedings - the relevant publications are listed below.

Publications

Shek, A. C. M., Semprebon, C., Panter, J. R., & Kusumaatmaja, H. (2021). Capillary Bridges on Liquid-Infused Surfaces. Langmuir, 37(2), 908-917.

Shek, A. C. M., & Kusumaatmaja, H. (2022). Spontaneous phase separation of ternary fluid mixtures. Soft Matter, 18(31), 5807-5814.

I have also contributed to the following publication outside the work in this thesis,

Pepona, M., Shek, A. C. M., Semprebon, C., Krüger, T., & Kusumaatmaja, H. (2021). Modeling ternary fluids in contact with elastic membranes. Physical Review E, 103(2), 022112.

Chapter 1

Introduction

Multi fluid systems are ubiquitous in the physical environment across various physical scales, including but not exclusive to: fluid inclusions of minerals [1, 2, 3] at the micro scale; oil deposits and spills [4, 5, 6], at everyday scales; to more extreme examples such as interactions between different particle species in plasma [7, 8, 9] present on Earth's magnetosphere and stellar entities, at astronomical scales. They are also present in many biological systems ranging from smaller to larger physical scales: within cells [10, 11, 12]; between cells and different tissue structures [13, 14, 15]; to larger scales such as wet adhesion between insect feet and surfaces [16, 17, 18]. Such multi-fluid systems are also relevant to many industrial applications including: the formation and stability of complex emulsions for in drug delivery [19, 20] and in the food industry[21, 22, 23]; in supercritical fluid extraction [24, 25, 26] to remove impurities or extract desired minerals from solvent solutions; and in the microscopic structure of metallic alloys which can affect the mechanical strength and resistance to wear of such composites[27, 28, 29, 30].

To study fluids we must first consider which length scale is relevant to study the desired physical scenario. In the nanometre scale, molecular dynamics theory and simulations are usually necessary to capture the key physical aspects [31, 32, 33]. In this thesis, where we consider everyday length scales around the millimetre to centimetre range, we will study fluid flows through continuum models, where the

fluid dynamics can be modelled by the Navier Stokes equation [34].

For our purposes, it is important to draw special attention to the interfaces which can occur during multi-component fluid flow. There are two types of interfaces which can occur with fluid flows, fluid-solid interfaces and fluid-fluid interfaces. Fluid-solid interactions can occur in single fluid systems, while, necessarily fluid-fluid interfaces are only possible in multi-fluid systems. In this thesis, we will interchangeably use the terms surface energy, surface tension and interfacial tension.

Transitioning from a single fluid to binary fluid system we introduce the fluid-fluid interface. Naturally as more and more fluids are present more types of fluid-fluid interfaces are possible. The number of fluid-fluid interfaces in a N-component fluid systems is given by $N(N-1)/2$. For example there is only one type of fluid-fluid interface between two fluids characterised by the associated interfacial energy. However, for the ternary system there are three such possible interfaces, while for quarternary systems 6 such interfaces are possible.

Binary fluid systems have been studied and understood for a variety of physical scenarios, including droplets [35, 36, 19], capillary bridges [37, 38, 39], de-wetting from surfaces [40, 41, 42].

In this thesis, we are interested in how some of these scenarios differ if an additional fluid phase/component is introduced. We discuss key concepts in binary fluids in the next section, followed by those for ternary fluids, and give a short preliminary overview here.

As a short preliminary, we will be studying both how multiple fluids interact with solid surfaces and how fluids interact with solid surfaces. We will be studying fluids wetting surfaces, and as such it is crucial to have an understanding of key concepts, such as the Young's contact angle, contact angle hysteresis, and wetting states on textured surfaces. Capillary bridges are discussed to highlight all these interactions, and are the key feature studied in Chapter 3: Sticky SLIPS . We will

also discuss contact line motion and briefly discuss various methods on how this is modelled. In our thesis, we use the diffuse interface model approach, but we also highlight other common methods. The conditions at which phase separation occurs in a binary fluid mixture is explored and the resulting structures which can occur are also highlighted.

When discussing ternary fluids, we will introduce the Neumann angles, a key bulk fluid feature, which play a key role in all the results in this thesis. We also explore how contact angles are restricted in ternary systems via the Girifalco-Good relation. The structures which can form in three fluid interactions are also highlighted. These concepts are then employed in studying equilibrium and dynamic scenarios.

While some of these concepts focus on thermodynamic equilibrium situations such as Young's contact angle, they are also relevant in modelling dynamic scenarios, e.g.the Young's contact angle is used to model the fluid solid interaction, in dynamically wetting scenarios. And as we will observe later the various Neumann angles play important roles even in dynamical situations. We will then discuss the key questions to be addressed in this thesis.

1.1 Key Concepts in Binary Fluids

We now go into details about the concepts of binary fluid systems relevant to our thesis.

1.1.1 Young's Contact Angle

We will first describe the Young's contact angle, θ_Y, which describes the contact line between two fluids, say liquid l and gas g, meeting at a smooth solid surface, s. Mathematically this is defined as,

$$\cos\theta_Y = \frac{\gamma_{gs} - \gamma_{ls}}{\gamma_{lg}}, \tag{1.1}$$

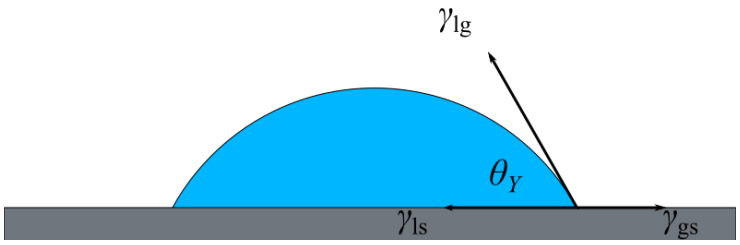

Figure 1.1: The liquid droplet, (blue), rests on a solid (grey) substrate, with θ showing the Young's contact angle. The various surface and interfacial energies are also highlighted.

where γ_{gs} and γ_{ls} are the surface energies between the gas and solid, and liquid and solid, and γ_{lg} is the interfacial energy between the two fluids. Fig. 1.1 shows a schematic diagram for how the surface and interfacial energies relate to the Young's contact angle, which affects the resulting shape of the droplet.

From our definition of the Young's contact angle we can also define the wetting or spreading parameter of a fluid, l, on a surface, s, is given by $S = \gamma_{gs} - (\gamma_{ls} + \gamma_{lg})$. If $S \geq 0$ then the liquid will completely wet the solid, mathematically this can be understood as the point beyond which the Young's contact angle reaches zero. For $S < 0$, the Young's contact angle has value between $0° < \theta_Y < 180°$.

1.1.2 Contact Angle Hysteresis

The Young's contact angle is strictly valid for a droplet at equilibrium on smooth and homogeneous surfaces. In dynamical situations, where the droplet is moving, multiplicity in the contact angles usually results. In such scenarios, we can consider advancing and receding contact angles, which are no longer the same, θ_{adv} and θ_{rec}. One way to infer them is by quasi-statically varying the droplet volume placed on the surface. θ_{adv} and θ_{rec} are the largest and smallest contact angles before the contact line depins. Another way is to consider the front and back contact angles of a droplet just before it moves when placed on a tilted surface. Fig. 1.2 shows a schematical diagram of the advancing and receding angles, along with the tilt angle, θ_{tilt}. The difference between the advancing and receding angles can be thought of

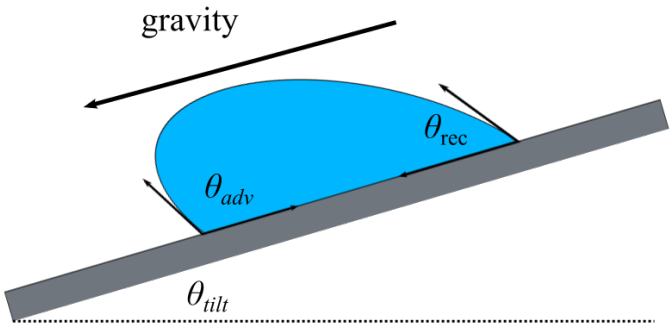

Figure 1.2: The liquid droplet (blue) slides on a solid (grey) substrate, with θ_{adv} and θ_{rec}, showing the advancing and receding angles respectively. The tilt angle corresponds to the angle when the droplet starts to move.

as a measure of the contact angle hysteresis [43, 44].

1.1.3 Textured Surfaces and Wetting States

So far we have discussed the situation with idealised smooth solid surfaces, however in reality most surfaces are textured to some degree. To understand such surfaces it is useful to consider several types of wetting states. There are three categories of relevance, the Wenzel [42], Cassie [41], and Hemi-wicking states [45]. Of course, fluids wetting a surface may exist in a mixed state as a combination of the three. Fig. 1.3 highlights the three states plus an example of a mixed state.

Naturally the contact angle on such surfaces must be modified. For the Wenzel state, where the droplet penetrates the corrugations, the effective contact angle is given by [46],

$$\cos\theta_W = r\cos\theta_Y, \tag{1.2}$$

where θ_W is the Wenzel contact angle and θ_Y is the Young's contact angle. The roughness factor, r, is the ratio of actual area wetted by the droplet over the projected surface area of contact with the droplet. Since $r \geq 1$, the effect of roughness is to amplify the surface hydrophobicity for $\theta_Y > 90°$, and it hydrophilicity for $\theta_Y < 90°$.

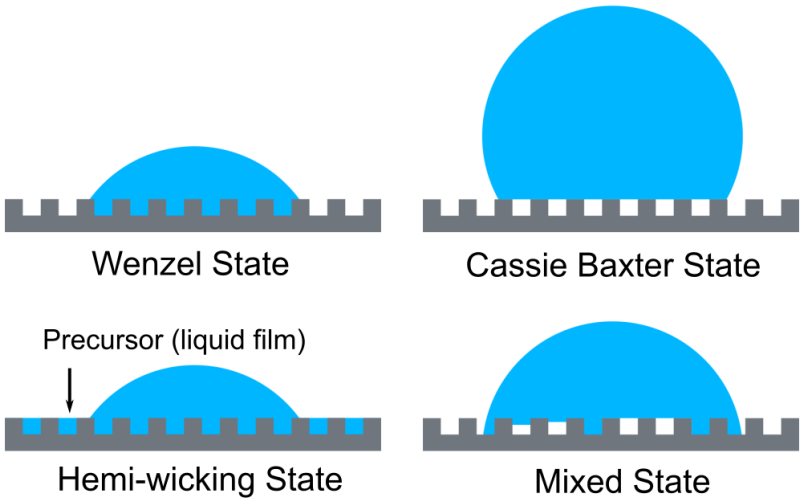

Figure 1.3: The above figure shows the different wetting states possible for a droplet on a textured surface. The Wenzel state is shown on the top left, where the droplet penetrates surface corrugations. An illustration of the Cassie-Baxter state is shown in the top right where the droplet does not penetrate the corrugations, instead resting on the top of them. In the bottom left we show the hemi-wicking state where a liquid film precursor fills the corrugation extending from the droplet. Finally in the bottom right we show a mixed state.

In the Cassie-Baxter state, the droplet is suspended on top of the corrugations. Effectively, the droplet sits on a composite substrate of solid and air in the Cassie-Baxter state. The Cassie-Baxter contact angle is given by, [46],

$$\cos\theta_{CB} = -1 + f(\cos\theta_Y + 1), \tag{1.3}$$

where θ_{CB} is the Cassie Baxter angle, and f is the projected area fraction of the solid in contact with the solid, and thus $f < 1$.

The concept of a composite substrate can also be extended to hemi-wicking states so long as they are stable [46]. In the geometry shown in Fig. 1.3, we can define the critical Young's contact angle for hemi-wicking to occur through the following relation,

$$\cos\theta_c = \frac{1-f}{r-f}. \tag{1.4}$$

In the geometry shown, and the fact that the top of the pillars remain dry, r and f are equivalent to those defined for the Wenzel and Cassie states. When

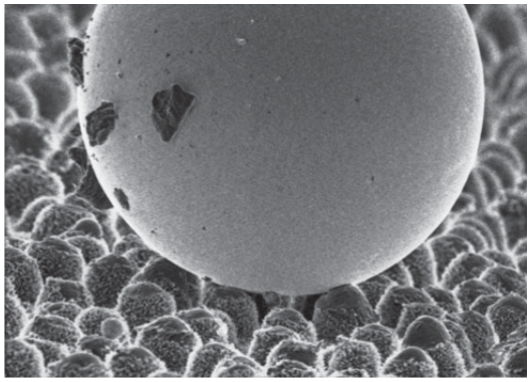

Figure 1.4: The above figure shows an example of a droplet removing a dust particle from a lotus surface [47, 53]. Reprinted with permission from Springer Nature: Planta, Purity of the sacred lotus, or escape from contamination in biological surfaces, W. Barthlott et al., copyright 1997.

$\theta_Y < \theta_c$ then Hemi-wicking states are possible. This allows us to determine the Hemi-wicking contact angle observed above the pillars to be

$$\cos\theta_H = f\cos\theta_Y + 1 - f. \tag{1.5}$$

The understanding of these various wetting states have crucial implications for the manufacture of several so called 'self-cleaning' surfaces. Perhaps the most common example being the superhydrophobic surfaces, inspired by the lotus effect [47, 48, 49]. Fig. 1.4 highlights how a dust particle is removed from a lotus surface by a droplet rolling across the textured surface [47]. In superhydrophobic surfaces, the presence of micro and nano structures induces the creation of air gaps between the droplet and the surface, and thus reduces the strength of capillary adhesion of the droplet onto the surface. To retain its self-cleaning properties the droplet must remain in the Cassie-Baxter state [41] as opposed to the Wenzel state [42]. One of the big challenges in developing such surfaces is the susceptibility of droplets to transition from the Cassie Baxter state to the Wenzel state due to external perturbations, and thus much research has been done on this wetting transition [50, 51, 52].

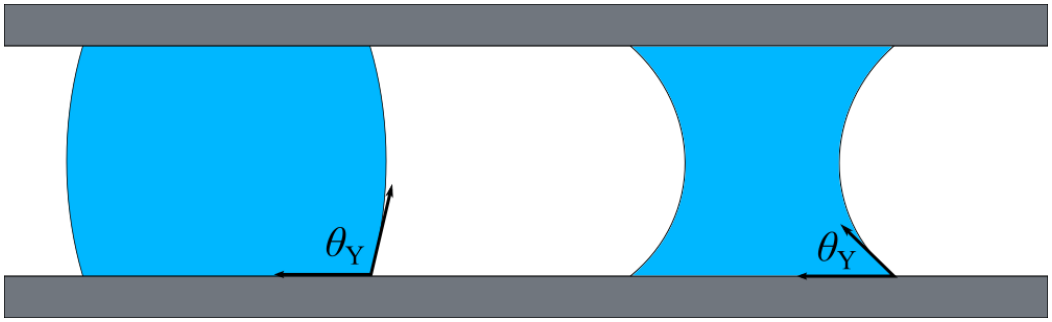

Figure 1.5: Here we show two examples of capillary bridges sandwiched between two surfaces, on the left is hydrophobic, and on the right is hydrophilic.

1.1.4 Capillary Bridges

A capillary bridge occurs when a droplet is sandwiched between two surfaces. In such a scenario the droplet induces a capillary force to act between the two surfaces. This force can be attractive or repulsive depending on the separation between the plates, the surface/interfacial energies and the volume of the droplet [37]. If we consider the simplest scenario of an axisymmetric droplet between two flat surfaces, then it is possible to calculate the capillary force between the surfaces. Fig. 1.5 shows two schematic diagrams showing a *hydrophobic* capillary bridge with $\theta_Y > 90°$ (left) and a *hydrophilic* capillary bridge with $\theta_Y < 90°$ (right).

The capillary force for such a binary fluid system is made up of two contributions, coming from the Laplace pressure and the surface tension of the droplet[37, 54]. If we consider one surface of contact between the capillary bridge and the surface, the capillary force is given by,

$$F_{cap} = -\Delta P_{lg} A_{ls} + \gamma_{lg} C \sin\theta_Y \tag{1.6}$$

where A_{ls} is area of contact between the liquid and the surface, and C is the perimeter of the area of contact. The Laplace pressure is the pressure difference between the liquid droplet and the surrounding gas which is related to the mean curvature of the liquid-gas interface,

$$\Delta P_{lg} = P_l - P_g = \gamma \left(\frac{1}{R_1} + \frac{1}{R_2} \right) = 2\gamma_{lg} H_{mean}, \tag{1.7}$$

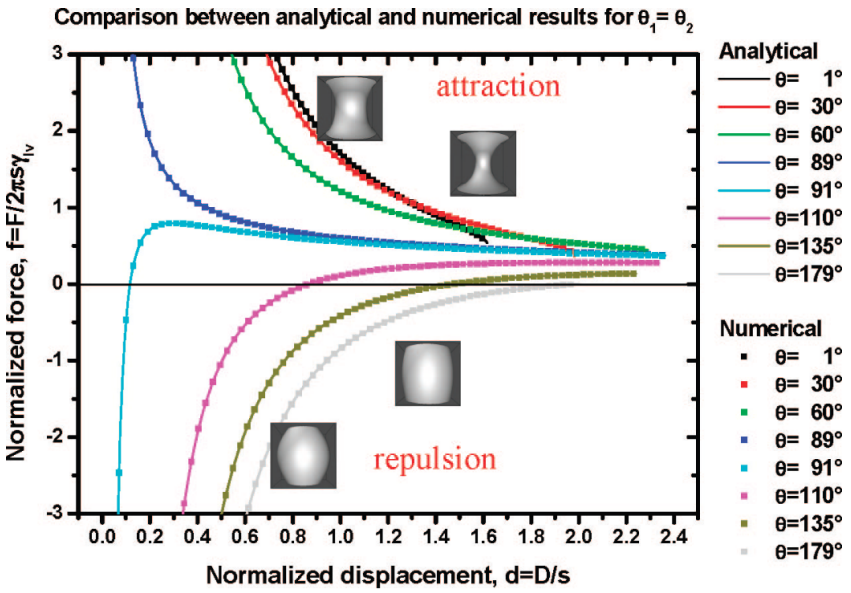

Figure 1.6: The above plot shows the capillary force as a function of plate separation for a wide range of contact angles[38]. Reprinted with permission from Langmuir, Enhancement of Capillary Forces by Multiple Liquid Bridges, E. J. De Souza et al. Copyright 2008. American Chemical Society.

where H_{mean} is the mean curvature of the interface, R_1 and R_2 are the two principal curvatures. The Laplace pressure can be generalised for arbitrary interfaces regardless of whether one of the fluids is a droplet or not, where the relationship between curvature and pressure difference is the same. The surface tension component will always be attractive, while the pressure difference component can be either positive or negative resulting in a repulsive or attractive contribution to the force.

We show how the typical capillary force depends on the Young's contact angle and separation distance between the two surfaces in Fig. 1.6 [54, 38]. Notice how for hydrophobic ($\theta > 90°$) capillary bridges, parts of the force curve can be negative, representing a repulsive force, whereas in comparison, for hydrophilic ($\theta < 90°$), the force always remains positive, regardless of separation distance. The calculated force curves have been verified to produce good predictions for experimental results, for chemically different substrates [54], and even in scenarios where contact angle hysteresis can be observed [55].

The study of capillary bridges are relevant across a wide range of applications exploiting different aspects of their properties. A set of examples are wet adhesion devices where the adhesive force induced by the capillary bridge is utilised [56, 57]. Importantly, it is not solely the capillary force which is of interest. In the example of liquid transfer [58, 59], the primary interest is on the shape of the capillary bridge surface and the amount of droplet transferred from one surface to another.

1.1.5 De-Wetting of Fluids and Contact Line Motion

In this thesis we are interested in droplet removal from a surface through de-wetting mechanisms. The fundamental aspect of such mechanisms would be the movement of the contact line [60].

At the level of macroscopic continuum mechanics, we run into the contact line singularity problem [61, 60, 62], which results when attempting to allow the contact line to move while trying to maintain the no-slip boundary condition. To alleviate this issue, it is necessary to include more microscopic physics at the contact line and couple with the Navier-Stokes equation. We will discuss two methods briefly, slip boundary condition and diffuse interface models [60]. In the results of this thesis we use diffuse interface models but we will give a brief description the common alternatives.

When introducing a slip boundary condition, the fluid velocity at the wall of the solid becomes [60],

$$u_{z=0} = l_s \frac{\partial u}{\partial z}, \tag{1.8}$$

where l_s is the characteristic slip length. There are many forms possible for the slip length. One form can be derived from a statistical theory of liquids [62, 60]

$$l_s \sim \frac{\eta Da k_B T}{[\gamma a^2 (1 + \cos\theta_e)]^2} a. \tag{1.9}$$

In the above equation, η is the viscosity of the droplet, D is the diffusion coefficient, a is a characteristic length scale representing the size of the fluid particle, and k_BT is the standard Boltzmann constant and temperature.

Another common approach is the Cox-Voinov theory, where the slip length, in the limit of small viscosity, is be related to the contact angle through a cubic relationship[60, 63],

$$\theta_{ap}^3 = \theta_e^3 + 9\mathrm{Ca}\ln\left(\frac{\alpha l_o}{l_s}\right). \tag{1.10}$$

Here the θ_{ap} is the macroscopic apparent contact angle, l_o is a macroscopic length scale which is larger than the slip-length, typically the capillary length or the size of the droplet, Ca is the capillary number, and α is a numerical prefactor of the order $O(1)$.

The other method would be to use a diffuse interface approach, as is done in this thesis. The diffuse interface approach will be discussed in detail in our Methodology chapter. In such a scenario as the contact line moves, there is imbalance in the chemical potential, leading to a diffusion mechanism for the effective motion, and hence, slip of the contact line.

1.1.6 Phase Separation

So far, we have discussed multicomponent systems where the components are already separated. In many scenarios, however, it is important to consider fluid mixtures which are initially mixed together.

Within mixtures, many structures can form and the stability is important for various applications. These range from tuning the formation of fractures in alloys in metallurgy [27, 28], for manipulating the structure of polymer blends which in turn affect their mechanical and electrical properties [64, 65, 66], and for controlling the morphology of complex emulsions and emulsion templating for applications in drug delivery [19, 20, 67] and in the food industry [21, 22, 23].

One of the key mechanisms for self-assembly of such structures is phase separation induced by spinodal decomposition [27, 10, 23]. Spinodal decomposition occurs when a mixture is no longer energetically stable to small fluctuations in the composition density and begins to phase separate into its constituent components. Importantly this is primarily dependent on the current state of the mixture, the composition of the different components, the temperature and pressure of the current system, and it is spontaneous. This contrasts with the other common separation mechanism, nucleation, because no energy barrier needs to be overcome, with the exception of perhaps any energy needed to quench the mixture. It also leads to global structures during the separation process. In comparison, nucleation is often dominated by heterogeneous nucleation at defects, points which are localised, and can seed growth of separate structures [27, 68, 10].

To describe spinodal decomposition, a common approach is to define a local order parameter $C(\mathbf{r}, t)$ which describes the local concentration of the two fluid components of the fluid mixture, and then define a free energy,

$$F = \int f_b(C) + \kappa(\nabla C)^2 \, \mathrm{d}V. \tag{1.11}$$

where f_b is the bulk free energy term, and $\kappa(\nabla C)^2$ are the gradient contributions. The interfacial tension between the two fluids is given by the following relation

$$\gamma = \int_0^1 \sqrt{4\kappa f_b(C)} \, \mathrm{d}V. \tag{1.12}$$

The evolution of the concentration can be described by the Cahn-Hilliard equation,

$$\frac{\partial C}{\partial t} = M\nabla^2\mu, \tag{1.13}$$

where μ is the chemical potential and M the mobility. The chemical potential is given by the functional derivative of the free energy,

$$\mu = \frac{\partial f_b}{\partial C} - 2\kappa\nabla^2 C. \tag{1.14}$$

Thus the evolution of the concentration is given by

$$\frac{\partial C}{\partial t} = M\left[\frac{\partial^2 f_b}{\partial C^2} + 2\kappa\nabla^4 C\right]. \tag{1.15}$$

Phase separation occurs when small perturbations of the concentration are unstable, i.e. when $\frac{\partial C}{\partial t} > 0$. The spinodal corresponds to the set of points at which macroscopic fluctuations become unstable and occurs when $\frac{\partial^2 f_b}{\partial C^2} = 0$. Macroscopic fluctuations are those with wavelengths tending towards infinity, or equivalently $k \to 0$, thus assuming $M > 0$, then $\frac{\partial C}{\partial t} > 0$ when $\frac{\partial^2 f_b}{\partial C^2} > 0$ as $k \to 0$. Hence, the spinodal occurs when $\frac{\partial^2 f_b}{\partial C^2} = 0$. Another related concept is the binodal, which occurs when the chemical potential of both components are equal. At the binodal, both components/phases are thermodynamically stable, and thus a mixed state is possible.

Being able to control the structures, which result, have applications in areas such as lithography, optical coatings, and flexible electronics [69, 70, 71]. Thus being able to predict the structures that can occur and their evolution in time would be highly beneficial. Typical binary fluid structures which can result are shown in Fig. 1.7. When the composition of the two fluids are close to being equal ($C \sim 0.5$), typically bi-continuous lamellae structure occur, see Fig. 1.7 (a), while when the compositions are far from equal ($C \neq\sim 0.5$), dispersed droplets typically result see Fig. 1.7 (b)[72].

After the initial phase separation has occurred there is further coarsening governing how such domains grow in size. Typically their size grows according to power law, $R \propto t^{\alpha}$ [73]. There are several common regimes, including, the diffusive regime and the hydrodynamic regime [74].

The diffusive regime occurs when the fluid advection velocity is zero, $\mathbf{u} = 0$ or small. During phase separation this typically occurs when the viscosity of the fluid is large such that the Reynolds number, Re, is small, or at the early stages of separation occurring. In the diffusive regime, the domain scales as $R \propto t^{\frac{1}{3}}$. In scenarios where the viscosity is not too high or later on in the coarsening process, hydrodynamics regime becomes more important. Here, the domain growth scales as $R \propto t$ in the viscous regime, and as $R \propto t^{\frac{2}{3}}$ in the inertial regime. In the hydrodynamic growth regime it is also observed that significant differences can

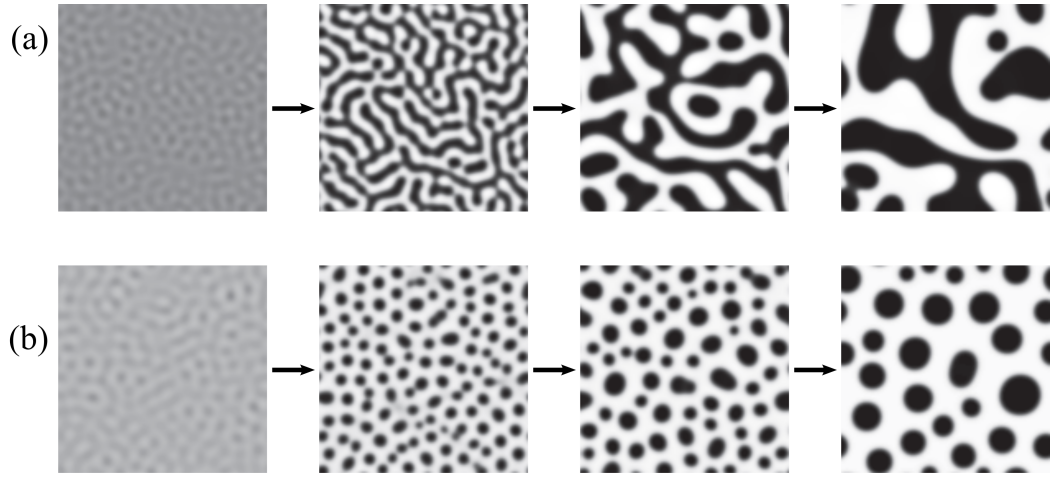

Figure 1.7: Here we show two typical separation pathways, the bi-continuous lamellae structures in row (a), and dispersed droplets in row (b) [72]. Used with permission of IOP Publishing, Ltd, from Viscoelastic phase separation, H. Tanaka, copyright 2000; permission conveyed through Copyright Clearance Center, Inc.

occur between the structures which result, depending on the fluid viscosity [74] and whether the system is under shear [73]. In the scenario of noise induced growth a random perturbation forcing term is added to the equation of motion.

1.2 Key concepts in Ternary Fluids

We now go into details about the concepts of ternary fluid systems relevant to our thesis.

1.2.1 Neumann Angles and Girifalco-Good Relation

When we introduce a third fluid to the system as mentioned earlier, we introduce two further types of fluid-fluid interfaces. As the three fluid-fluid interfaces meet they form a three fluid contact junction, leading to the concept of Neumann angles. Fig. 1.8 shows a liquid lens system with three fluids. The Neumann angles can be determined by considering the force balance at the triple contact junction,

$$\vec{\gamma}_{12} + \vec{\gamma}_{13} + \vec{\gamma}_{23} = 0. \tag{1.16}$$

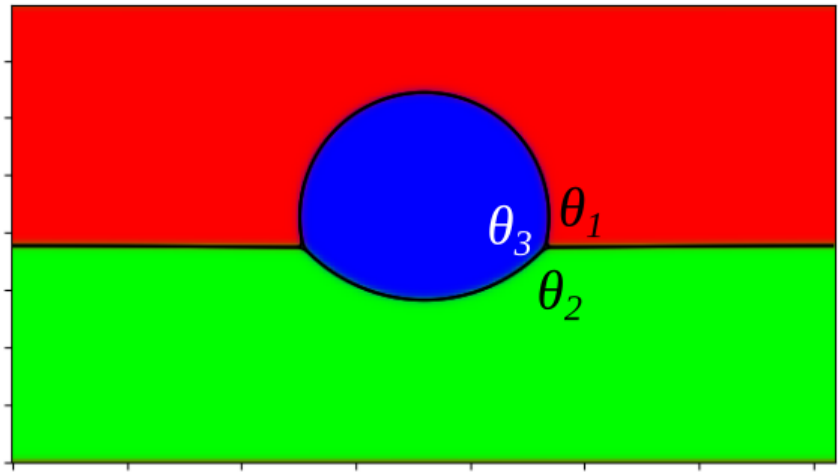

Figure 1.8: Here we show a liquid lens between three fluids: 1 (red), 2 (green) and 3 (blue). We also highlight the Neumann Angles, θ_1, θ_2, and θ_3.

By considering a cross-section of any triple contact line we can consider the scenario in 2D without loss of generality, similar to Fig. 1.8. If we consider $\vec{\gamma}_{12}$ as acting in the x-direction, then Eqn. 1.16 becomes

$$\gamma_{12}\begin{pmatrix}1\\0\end{pmatrix}+\gamma_{13}\begin{pmatrix}\cos\theta_1\\\sin\theta_1\end{pmatrix}+\gamma_{23}\begin{pmatrix}\cos\theta_2\\-\sin\theta_2\end{pmatrix}=0. \tag{1.17}$$

From the y-component it is clear that,

$$\gamma_{13}\sin\theta_1-\gamma_{23}\sin\theta_2=0 \tag{1.18}$$

and thus,

$$\frac{\gamma_{13}}{\sin\theta_2}=\frac{\gamma_{23}}{\sin\theta_1}. \tag{1.19}$$

We also know that

$$\begin{aligned}
\gamma_{12}+\gamma_{13}\cos\theta_1+\gamma_{23}\cos\theta_2&=0\\
\gamma_{12}&=-\gamma_{13}\left(\cos\theta_1+\frac{\sin\theta_1}{\sin\theta_2}\cos\theta_2\right)\\
&=-\gamma_{13}\frac{\cos\theta_1\sin\theta_2+\sin\theta_1\cos\theta_2}{\sin\theta_2}\\
&=-\gamma_{13}\frac{\sin(\theta_1+\theta_2)}{\sin\theta_2}\\
&=\gamma_{13}\frac{\sin(2\pi-(\theta_1+\theta_2))}{\sin\theta_2}\\
&=\gamma_{13}\frac{\sin\theta_3}{\sin\theta_2}
\end{aligned} \tag{1.20}$$

Hence, we now also know that

$$\frac{\gamma_{12}}{\sin\theta_3} = \frac{\gamma_{13}}{\sin\theta_2} = \frac{\gamma_{23}}{\sin\theta_1}. \tag{1.21}$$

When considering the contact angles on the solid surface, it is also important to note that the resulting contact angles between any two fluids and the solid are not completely independent. The three possible Young's contact angles are also related via the Girifalco-Good relation,

$$\gamma_{12}\cos\theta_{12} + \gamma_{23}\cos\theta_{23} + \gamma_{31}\cos\theta_{31} = 0. \tag{1.22}$$

Here the contact angle $\cos\theta_{ij}$ represents the contact angle measured from i to j, and thus $\cos\theta_{ij} = -\cos\theta_{ji}$. To verify the Girifalco–Good relation consider the Young's contact angle definition in terms of solid-surface tensions,

$$\cos\theta_{ij} = \frac{\gamma_{js} - \gamma_{is}}{\gamma_{ij}}. \tag{1.23}$$

Hence, the left-hand side of the Girifalco-Good relation becomes

$$\gamma_{2s} - \gamma_{1s} + \gamma_{3s} - \gamma_{2s} + \gamma_{1s} - \gamma_{3s} = 0. \tag{1.24}$$

Where the above highlights how the left-hand side of the Girifalco-Good relation sums to zero.

1.2.2 Liquid Infused Surfaces

In this thesis we study liquid-infused surfaces (LIS), or slippery liquid infused porous surfaces (SLIPS), inspired by the slippery surface of the Nepenthes plant [75, 76, 77, 78], which are often considered an alternative to superhydrophobic surfaces [79]. Such surfaces are composed of a textured substrate imbibed by a lubricant fluid, and when wetted by a droplet we obtain a three fluid system (the droplet, the lubricant and the surrounding gas).

There are several aspects to LIS which lend to much interest in applications. Its slippery nature lends naturally to applications in self-cleaning surfaces [77,

78, 80, 81], food packaging [82], anti-fouling surfaces [83, 84], and heat transfer via droplet condensation [85, 86]. The presence of the lubricant which cover the underlying substrate also inhibits bacterial growth on surfaces [87, 88], and leads to anti-icing properties so long as the temperature is well above the freezing point of the lubricant [81, 89, 90].

When compared to superhydrophobic surfaces, the main advantage of LIS is that it is more resistant to pressure failure and to penetration by the droplet due to the presence of the lubricant. However, at the same time, lubricant retention over the lifetime of LIS is a technical challenge whose solution is still an active area of research [91, 92].

Fig. 1.9 (a) and (b) show schematic diagrams of how such surfaces interact with a droplet. In general, there are a number of possible wetting states. These wetting states depend on whether the droplet is cloaked: in Fig. 1.9 (a) the droplet is fully encapsulated by the lubricant, while Fig. 1.9 (b) shows a lubricant ridge forming at a triple contact with the droplet and surrounding air; as well as how much the lubricant is wetting the solid corrugations. Fig. 1.9 (a) shows the case where the lubricant is fully wetting the solid, while Fig. 1.9 (b) presents the case with a partially wetting lubricant. In effect there are a combination of wetting states occurring.

1.2.3 Ternary Phase Separation

Phase separation in ternary fluid mixtures can result in various fluid structures [68, 93]. Previous works have identified several types of morphologies which differ from binary mixtures, and their dependence on the composition have been tabulated [68]. The analysis by Naumann et al. [68] largely focused on subtle differences between the observed morphologies but did not attempt to define rules to predict which structures will form. See Fig. 1.10 for a small sample of the morphologies possible, which were obtained experimentally. When three fluids are present many

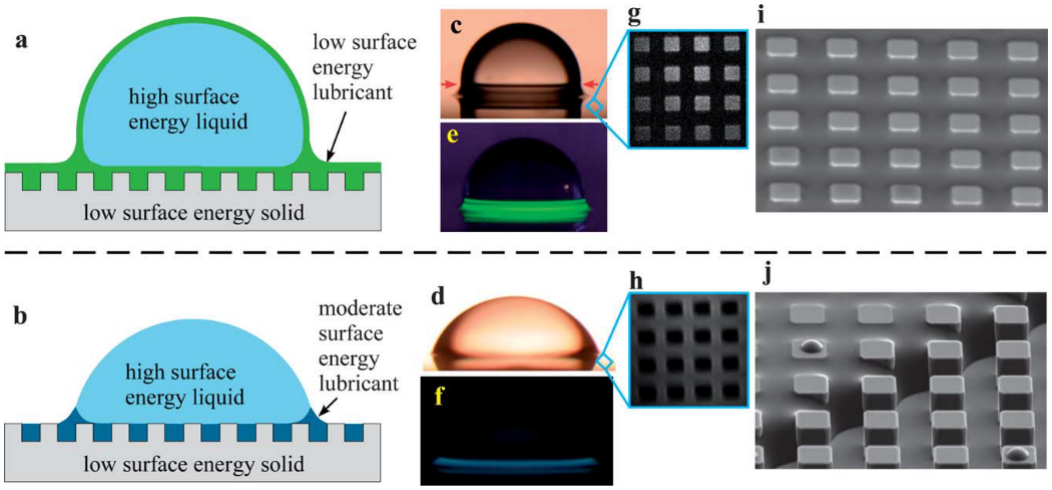

Figure 1.9: The above set of figures shows a liquid-infused surface, with the top row highlighting an encapsulated droplet and the bottom an non-encapsulated one. Panels (a) and (b) are schematical diagrams of both scenarios; (c) and (d) images of the real droplets resting on the surface; (e) and (f) showing highlighting the raised lubricant with dye; (g) - (j) show the underlying surface structure of such surfaces. [77].Used with permission of Royal Society of Chemistry, from Droplet mobility on lubricant-impregnated surfaces, J. D. Smith, et al., volume 9, copyright 2013; permission conveyed through Copyright Clearance Center, Inc

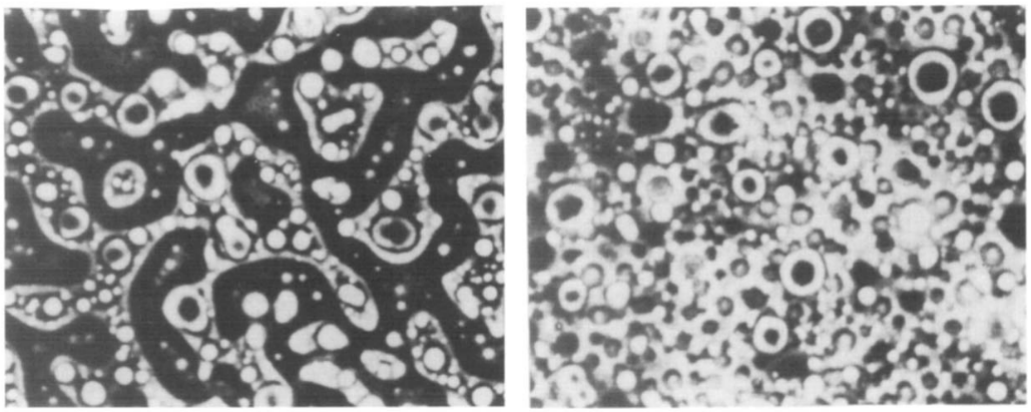

Figure 1.10: Various observed morphologies resulting from varying concentrations of three polymer blends [68]. Reprinted from Polymer Papers, E. B. Naumann, Morphology predictions for ternary polymer blends undergoing spinodal decomposition, 2243-2255, Copyright 1994, with permission from Elsevier.

more different topological structures are possible, when compared to the binary fluids case discussed in Sec. 1.1.6. In Fig. 1.10 we can observe substructures within the larger structures.

Another set of studies have utilised ternary phase separation to form various

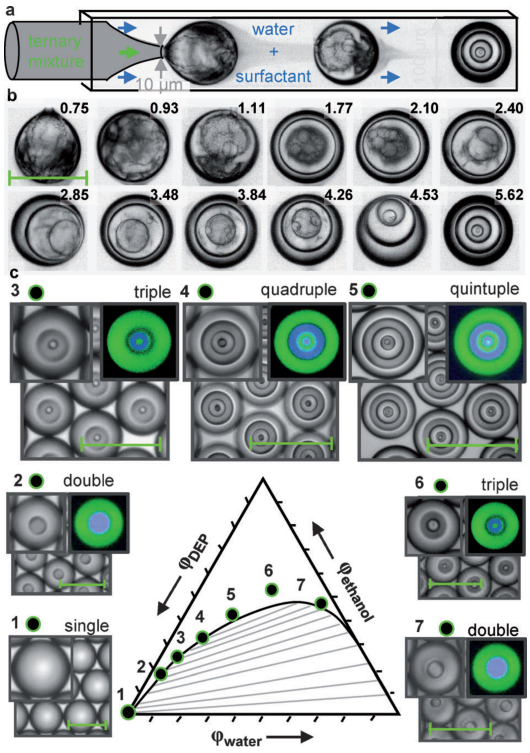

Figure 1.11: The above figure shows the details of how a multi-layered emulsion is formed from a ternary mixture. Panel (a) shows a diagram detailing the experimental use of a microfluidic glass capillary to form a multi-layered emulsion. Panel (b) shows how the ternary droplet undergoes phase separation to form a multi-layered emulsion droplet. Finally, panel (c) shows the phase diagram detailing how the number of layers is dependent on the composition of the mixture. [94]. Used with permission of John Wiley & Sons - Books, from Tailoring of High-Order Multiple Emulsions by the Liquid–Liquid Phase Separation of Ternary Mixtures, Haase, Martin F. et al, volume 126, copyright 2014; permission conveyed through Copyright Clearance Center, Inc.

emulsion structures [94, 95] for potential applications in drug delivery and emulsion templating. Here, the studies involve forming multi-layered emulsions using microfluidics. Three fluids are used, (oil, water and solvent) and it was found that the number of layers was dependent on the composition of the ternary fluid droplet. Fig. 1.11 shows experimental images of how the droplet forms multiple layers [94].

Other structures such as patchy and janus droplets have also drawn attention, for similar applications [96, 97]. In the early stages the structure formation is due to phase separation. Eventually, as the patches are enriched onto the surface of the

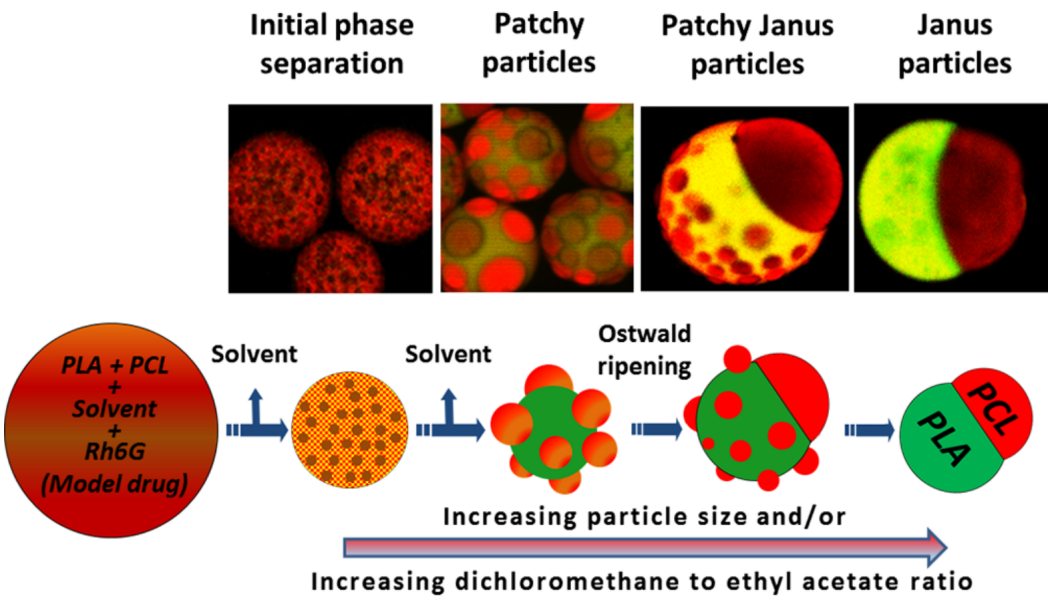

Figure 1.12: Here we show the evolution of a ternary mixture to form patchy droplets which eventually equilibrates to a Janus droplet [97]. Used under CC-BY license from American Chemical Society, Langmuir, Facile Production of Biodegradable Bipolymer Patchy and Patchy Janus Particles with Controlled Morphology by Microfluidic Routes, E. Ekanem et al. Copyright 2017.

droplets, they coalesce by undergoing Ostwald ripening. Fig. 1.12 highlights the stages of the droplet changing structure from a mixture to a patchy droplet and finally a Janus particle.

It is clear that the structures which are possible with ternary fluid systems are of interest for many applications. Currently much of the research focuses on what structures are possible [68, 98, 93, 96, 97, 94, 95]. However, to the best of our knowledge, there is a lack of a general understanding about how such structures form.

Much of the literature [68, 99, 93, 98, 100] focuses on using eigenvalues obtained from linear stability analysis to understand how the three fluids grow and form structures. This is in effect a ternary spinodal analysis [100]. However, there seems to be an underappreciation of the role of eigenvector components on how the fluid develop different structures. In our work we will highlight the importance of such tools in understanding ternary mixtures undergoing phase separation.

1.3 Binary and Ternary Fluid Systems

From a conceptual perspective, the key difference between a single component fluid system and a binary one is the existence of a fluid-fluid interface which is usually characterised by the interfacial tension between the two fluids. When moving from binary to ternary fluid systems, we have additional fluid-fluid interfaces. The Neumann angles provide a measure of how the three fluids interact with each other at the triple contact junction with no analogy to the binary case. In this thesis we will study and focus on three ternary fluid phenomena, Sticky Slips, Ternary De-Wetting, and Ternary Phase Separation. Before discussing these phenomena, we first highlight the challenges with modelling multi-fluid systems.

Our approach is to use free energy models, both for sharp interface and diffuse interface models. There is still active research on developing and implementing such models [101, 102, 103, 104, 105]. The introduction of a third fluid poses new challenges to the standard derivations of the equations of motion. This is especially true when determining the chemical potentials from the free energy models for immiscible fluids [106, 107, 108]. Notably a new concept arises, the reducibility and consistency of such equations of motion obtained. The terms reducibility and consistency refer to the fact that the equations of motion, of say a N-component system, must reduce to the equations of the motion of the $N-1$ component system when a component is absent in the system. We will discuss these issues in detail in Chapter 2: Methodology.

After Chapter 2: Methodology we will discuss our main results. Chapter 3: Sticky SLIPS will discuss the effects of a third fluid acting as the lubricant on the capillary forces and capillary bridge morphologies between two liquid infused surfaces, when compared to a single liquid component capillary bridge, between two smooth surfaces. We will highlight how it is possible to have several stable capillary bridge morphologies and how the capillary force is enhanced due to the presence of the third fluid. Importantly, the behaviour cannot be simply reduced

to that of a single liquid component capillary bridge.

Our next chapter will be Chapter 4: Ternary De-Wetting, where we will discuss a new mechanism for droplet removal by making use of the ternary fluid contact line. In comparison to more traditional binary fluid systems we use a thin liquid film to de-wet the droplet rather than flooding the surroundings with a cleanser fluid. This liquid film is then slowly increased in thickness, which raises the triple contact line and pulls the droplet with it. We will show that in the quasi-static limit the de-wettability of a droplet can be understood by treating the stretched droplet as a capillary bridge. Here, the Neumann angles play a key role in whether the droplet de-wets or not.

Finally we study the phase separation pathways of ternary fluid mixtures in Chapter 5: Ternary Phase Separation. We will categorise the various separation pathways and resulting fluid structures which can form. Unlike the binary case where the conditions for when phase separation would occur can be determined by determining the spinodal, we will show that in the ternary case the spinodals gives limited information. An often neglected part of linear stability analysis, the eigenvector components, play a key role in the structures which can result. We also study the phase separation pathway, where the minor component is enriched and undergoes an instability at the interface of the two major components to determine its dependence on the thickness of the enriched component layer formed.

Chapter 2

Methodology

2.1 Modelling Ternary Component Systems

To model ternary component fluid systems we must first consider which material parameters are relevant for the physical scenarios of interest. In this thesis, we are interested in phenomena where the fluids can be represented as a continuum. In this case, key parameters include the interfacial parameters, such as fluid-fluid interfacial tensions and fluid-solid interaction energies, as well as the bulk parameters, such as the fluid density and viscosity. When modelling multi-component fluid systems there are two broad categories of models, sharp interface [109, 110] and diffuse interface models [111, 112, 113].

In a sharp interface model, whenever there are two or more fluid components/phases separated from each other, we explicitly model the interface between the two as a sharp boundary. This boundary would be a point in 1D, a line in 2D, and a surface in 3D, and importantly there is no thickness to this boundary. Common numerical approaches that are often used with sharp interface models include the level set method [114, 115, 116], front tracking method [117, 118, 119], and volume of fluid method [120, 121, 122]. In this thesis we use a sharp interface model for quasi-static study for capillary bridges, where we are solving surfaces at equilibrium. However, it must be noted that sharp interface models can be used

for dynamic scenarios [123], where the interface can evolve sharply and quickly, but this can be difficult to implement numerically. We will explain this further later.

Sharp interface models map well to many physical scenarios where the interfacial thickness (usually of the order of several nm) between the fluids is much smaller than the length scale of the flow. Such length scales are related usually by the length scale of the boundaries of the system, such as the width of a channel where the liquid is undergoing flow. However, the sharp interface approximation breaks down when the physical scales of interest become more comparable to the interface thickness, such as in nanofluidics [111]. The main difficulty in sharp interface models is often in how the interface is tracked and how they are coupled to the Navier-Stokes equation [123]. Correspondingly, these models are often less favourable to problems where the interface topologies change rapidly, such as in droplet coalescence and breakup, or in the dynamics of fluid phase separation. Because the interface is sharp any change from one side of the interface to the other, will usually lead to a discontinuity of the relevant variable, such as the fluid density, and thus the equations of motion usually cannot remain continuous across the interface. The discontinuities across interfaces can be removed through the use of diffuse interface models.

We now discuss the general features of a diffuse interface model. In the literature such a model is often called a phase field model. In such a model the local concentration and/or density of each fluid component is represented by an order parameter. Across an interface between either two fluid components or phases the relevant order parameter will vary smoothly. This leads to a characteristic interfacial width which is non-zero. There are several methods to implement these models [124], including the finite difference method [125, 126, 127], the finite element method [128, 129, 130], and spectral methods [131, 132]. In this thesis we will focus on the use of the Lattice Boltzmann method (LBM) [133, 134, 135].

A major advantage of diffuse interface models is that the interface no longer needs to be tracked explicitly [111, 136]. To introduce a diffuse interface, typically,

a set of equations of motion, such as the Cahn-Hilliard or Allen-Cahn equations, are used to capture the evolution of relevant order parameters, and these equations apply everywhere throughout the simulation domain. This makes diffuse interface models convenient for studying highly dynamic interfacial flows where the interfaces evolve rapidly, such as during collision of droplets and phase separation. However, the existence of a non-zero interface width means that care must be made to ensure the relevant physics is not affected by the length scale implicitly set by the interfacial width. In real physical scenarios such an interface width is usually in the nanometre scale. Computationally, it is practically impossible to simulate the quantitatively correct interface width. For example, if we allocate 5 lattice points to capture an interface with of 1 nm, to simulate a droplet, with a radius of 1 mm, would require $O(10^{18})$ lattice points in three dimensions, which is neither feasible nor, in fact, necessary. In diffuse interface models, accurate simulations can be achieved as long as the length scales of the phenomena of interest are considerably larger than the interface width, ideally by one or more orders of magnitude. Due to potential chaotic evolution of an interface, this would also be necessary in cases where the motion is along an interface to ensure reliable results.

In this thesis, we will take advantage of both sharp and diffuse interface models in different scenarios where each approach is particularly advantageous. We use a sharp interface model to the study the quasi-static evolution of a capillary bridge between two liquid infused surfaces, where changes of the interface topologies are not the dominant features of interest. In our quasi-static method dynamical effects, such as those due to viscosity, were ignored. We give an overview of our algorithm for minimising the energy in a flow diagram shown in Fig. 2.1. We then apply a diffuse interface model to study the dynamical evolution of fluid interfaces during a novel de-wetting process and phase separation. We will discuss the explicit models we employ in this thesis in the following sections of this chapter.

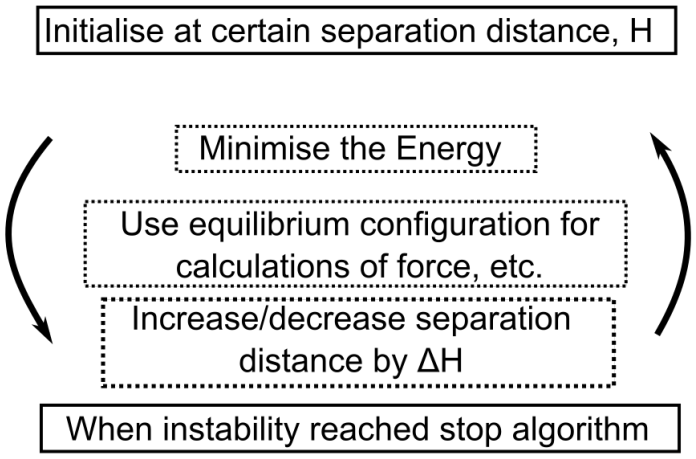

Figure 2.1: The flow diagram shows an outline of the energy minimisation algorithm used in Surface Evolver to obtain the capillary bridge equilibrium states. The steps in solid boxes are the initial and end states of the algorithm. For every separation, H, which allows for a stable capillary bridge we minimise the energy to obtain an equilibrium configuration. This allows us to compute the relevant quantities such as the capillary force. We then increase/decrease the separation by a chosen amount, ΔH, and repeat the steps until we reach an instability. The steps in dashed boxes are the repeated steps.

2.2 Sharp Interface Model

In Chapter 3: Sticky SLIPS we will study capillary bridges sandwiched between two liquid infused surfaces (LIS) [76]. Contrasting with the more commonly studied cases of capillary bridges where only one liquid component forms the droplet capillary bridge [37], capillary bridges between LIS are formed by two liquid components, one being the droplet liquid and the other is the lubricant fluid infused into the LIS. In both cases the capillary bridge is also surrounded by another fluid, the surrounding gas. We are interested in what differences such a two component liquid capillary bridge (ternary fluid system: droplet, liquid and gas) would have in comparison to one-component liquid capillary bridges (binary fluid system: droplet and gas). In our studies we vary the separation of the two LIS quasi-statically and, as such, we can ignore dynamical effects. As we discussed previously this lends to a suitable scenario to use a sharp interface model, because the interfaces evolve

slowly.

2.2.1 Free Energy Formulation

To develop the model we begin by considering the binary case with one liquid component first, as shown in Fig. 2.2 (a). This will then allow us to extend the model to the ternary case with two liquid components, as illustrated in Fig. 2.2 (b) - (d), and allow easier comparisons of the differences and similarities between the two cases Fig. 2.2 (b) - (d). The total free energy of the one-component liquid capillary bridge [137, 138] is given by

$$\begin{aligned} E_{smooth} &= \gamma_{dg}A_{dg} + \gamma_{ds}A_{ds} + \gamma_{gs}A_{gs} - \Delta P_{dg}V_d, \\ &= \gamma_{dg}A_{dg} - \gamma_{dg}\cos\theta_{dg}A_{ds} - \Delta P_{dg}V_d + \mathrm{C}_1, \end{aligned} \tag{2.1}$$

where the γ_{ij} and A_{ij} are the surface tension and interfacial area between components i and j, V_d is the drop volume, and ΔP_{dg} is the pressure difference between the drop and gas components. We assume the liquid drop is non-volatile, so that its volume is a conserved quantity. For a fixed drop volume V_d, the term ΔP_{dg} can be interpreted as a Lagrange multiplier. Rearranging the terms, and assuming the capillary bridge is confined by ideal and smooth surfaces, the liquid wettability is expressed by the material contact angle, $\cos\theta_{dg} = (\gamma_{gs} - \gamma_{ds})/\gamma_{dg}$. The remaining terms sum up to a constant, $\mathrm{C}_1 = \gamma_{gs}(A_{gs} + A_{ds})$, which do not alter the liquid bridge morphology, and can be neglected.

We can then extend the above model to a capillary bridge between two liquid infused surfaces (LIS). In such a scenario the three fluid components are the lubricant infused in the surface, *l*, the droplet sandwiched between the surfaces, *d*, and the surrounding gas, *g*. See Fig. 2.2 (b) for a model capillary bridge between two LIS. Here the lubricant ridges are formed around the droplet due to capillary action. As in previous works [139, 140, 141], we divide the total free energy contributions into two parts, the fluid-fluid and fluid-solid contributions, such that

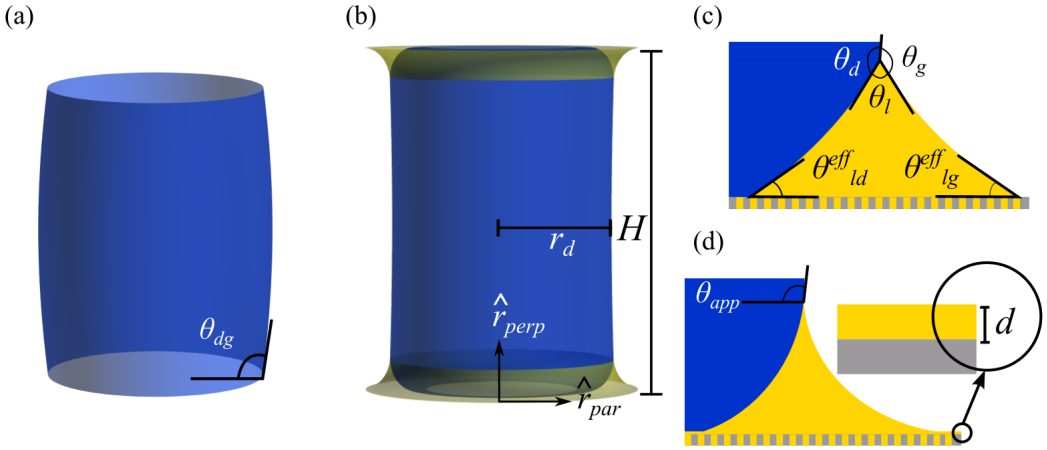

Figure 2.2: Capillary bridge geometry and parameters. Panel (a) shows a capillary bridge between two smooth surfaces. Panel (b) shows a capillary bridge between two LIS, where H is the separation distance, and $\hat{r}_{perp}$, $\hat{r}_{par}$ are the unit vectors perpendicular and parallel to the substrate. Panels (c) and (d) show the capillary bridge cases where the lubricant partially and completely wetting the solid corrugations, respectively. Additionally, panel (c) illustrates the definition of the Neumann angles, θ_l, θ_d, θ_g, and the effective wetting contact angles, θ^{eff}_{ld} and θ^{eff}_{lg}. Panel (d) also gives a geometrical interpretation of the apparent contact angle, θ_{app}, and the lubricant film thickness, d.

$E_{\text{LIS}} = E_{\text{FF}} + E_{\text{FS}}$. The fluid-fluid contributions are

$$E_{\text{FF}} = \gamma_{dg}A_{dg} + \gamma_{ld}A_{ld} + \gamma_{lg}A_{lg} - \Delta P_{dg}V_d - \Delta P_{lg}V_l. \tag{2.2}$$

Similar to the one-component liquid bridge case, the drop volume is assumed to be constant. For the lubricant (subscript l), we assume the rest of the substrate infused by the lubricant provides a virtually infinite reservoir. In experiments the lubricant exchange between the ridge and surrounding substrate can occur on a rather slow timescale due to the strong viscous dissipation in the thin lubricant layer [142]. However, we will assume this exchange is still much faster than the typical variation in the control parameters used in this work, such as the separation between the two LIS. Consequently, we employ the pressure ensemble for the lubricant, parameterised by the pressure jump ΔP_{lg} at the lubricant-gas interface. The term $-\Delta P_{lg}V_l$ in the free energy represents the energy cost for drawing additional lubricant from the reservoir.

When the lubricant only partially wets (PW) the solid surface, see Fig. 2.2(b),

we can write the fluid-solid contributions as

$$\begin{aligned} E_{\mathrm{FS(PW)}} &= \gamma_{ds}^{\mathrm{eff}} A_{ds}^{\mathrm{pr}} + \gamma_{ls}^{\mathrm{eff}} A_{ls}^{\mathrm{pr}} + \gamma_{gs}^{\mathrm{eff}} A_{gs}^{\mathrm{pr}} \\ &= \gamma_{ld} A_{ds}^{\mathrm{pr}} \cos\theta_{ld}^{\mathrm{eff}} - \gamma_{lg}(A_{ds}^{\mathrm{pr}} + A_{ls}^{\mathrm{pr}}) \cos\theta_{lg}^{\mathrm{eff}} + \mathrm{C}_2, \end{aligned} \tag{2.3}$$

where A_{is}^{pr} is the projected interfacial area between fluid i and the substrate. The index $i = d, g$ represents either the drop or gas phase. It is worth emphasizing that the substrate is effectively a composite of the underlying rough solid surface and the imbibed lubricant. For simplicity, we will not resolve the details of the composite surface. Instead, we simply assume this gives rise to an effective average surface tension $\gamma_{is}^{\mathrm{eff}} = f\gamma_{is} + (1-f)\gamma_{il}$, with f the fraction of the projected solid area exposed to the drop or gas phase. We also define the effective contact angle $\cos\theta_{ij}^{\mathrm{eff}} = (\gamma_{js}^{\mathrm{eff}} - \gamma_{is}^{\mathrm{eff}})/\gamma_{ij}$ between phases i and j on the composite solid-lubricant substrate. The constant term $\mathrm{C}_2 = \gamma_{gs}^{\mathrm{eff}}(A_{ds}^{\mathrm{pr}} + A_{ls}^{\mathrm{pr}} + A_{gs}^{\mathrm{pr}})$ can be neglected for the same reason that it will not affect the resulting morphology.

The limit of $\theta_{ld},\ \theta_{lg} \to 0^\circ$ describes the complete wetting (CW) case, Fig. 2.2(c), where the lubricant will form a thin layer above the surface. The thickness of the lubricant layer is determined by the intermolecular interactions between lubricant and solid [143]. These interactions are also often called the disjoining pressure term. To extend our calculations to this limit, we introduce

$$E_{\mathrm{FS(CW)}} = \int \frac{B}{12\pi d(\mathbf{r})^2}\, \mathrm{d}A, \tag{2.4}$$

where B is a constant and d is the thickness of the lubricant layer. A different choice for this contribution would not alter the results of this study, as long as the film thickness is small compared to the size of both the drop and the lubricant ridge. In practice, we also do not observe major differences in the results for full wetting and small but finite contact angles.

On LIS, the drop-gas interface does not come in contact with the solid, due to the ubiquitous presence of a lubricant ridge, see Fig. 2.2. At the top of this lubricant ridge, there is a triple contact line where the drop-gas (dg) interface

meets the lubricant-gas (lg) and lubricant-drop (ld) interfaces. The three Neumann angles, θ_l, θ_d and θ_g, are related to the interfacial tensions via

$$\frac{\gamma_{ld}}{\sin\theta_g} = \frac{\gamma_{dg}}{\sin\theta_l} = \frac{\gamma_{lg}}{\sin\theta_d}. \tag{2.5}$$

Consequently, on LIS the definition of a material contact angle needs to be adapted. Two alternatives are possible: either taking the slope of the drop-gas interface immediately above the triple line, or by estimating the slope of the (virtual) drop-gas interface if it were to continue within the lubricant ridge. Following Semprebon *et al.* [139], we employ the first definition, as illustrated in Fig. 2.2(c). This definition has an advantage that the triple line is directly visible, and therefore it is easy to be measured in experiments. The second definition instead would better approximate the overall drop shape in the case of large ridges. In the limit of vanishing lubricant ridges, the two definitions coincide and the apparent contact angle can be expressed as an average of the effective lubricant-drop and lubricant-gas contact angles, weighted by the ratios of surface tensions:

$$\begin{aligned}\cos\theta_{app} &= -\cos\theta_{ld}^{\text{eff}}\frac{\gamma_{ld}}{\gamma_{dg}} + \cos\theta_{lg}^{\text{eff}}\frac{\gamma_{lg}}{\gamma_{dg}} \\ &= -\cos\theta_{ld}^{\text{eff}}\frac{\sin\theta_g}{\sin\theta_l} + \cos\theta_{lg}^{\text{eff}}\frac{\sin\theta_d}{\sin\theta_l}.\end{aligned} \tag{2.6}$$

Unless specified otherwise, this equation defines the apparent angle used throughout the thesis. It allows us to compare the wettability of droplets on LIS with those on homogeneous surfaces, employing θ_{app} for the former and θ_{dg} for the latter. It should be noted here that θ_{ij}^{eff}, takes into account the case where the lubricant does not fully cover the solid protrusions, as detailed in Eqn. 2.3. However, in cases where a course grained approximation is insufficient, then it may be necessary to explicitly consider Young's contact angles between the solid protrusion and various fluid interfaces. This could occur if say the solid corrugations are highly irregular, then in effect θ_{ij}^{eff} can be thought of as position dependent, which would of course depend on the precise geometry of the corrugations.

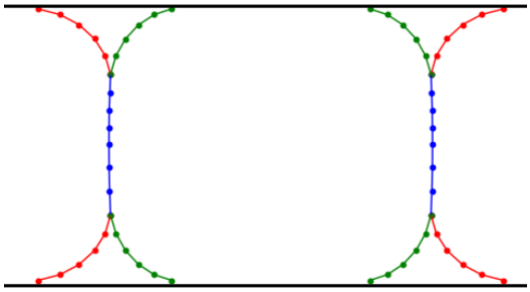

Figure 2.3: The figure shows a sketch of how the three interfaces in our axisymmetric model are modelled using Surface Evolver. The dots represent the vertices, while the lines are the edges connecting the edges. In red we have the lubricant-gas interface, green the lubricant-droplet interface, and in blue the droplet-gas interface. For completeness, we also show the reflected interfaces on the left, as we only need one set for the axisymmetric model.

2.2.2 Numerical Implementation - Surface Evolver

We compute the liquid bridge morphologies in mechanical equilibrium by numerically minimising the free energy. To do this, we employ the public domain software Surface Evolver [144, 145]. Owing to the symmetry of the problem, we employ an effective 2D model with rotational symmetry [139, 54, 55, 38].

The three fluid interfaces between drop, lubricant and gas are modelled by discrete segments joining at a point representing the drop-lubricant-gas triple line near the top and bottom of the capillary bridge. This is shown in Fig. 2.3, where we also show for clarity a reflected image of the edges and vertices on the left.

In this effective 2D model, each of the lubricant-drop and lubricant-gas interfaces also meets the substrate at a point corresponding to the substrate-lubricant-drop and substrate-lubricant-gas contact lines in the case of finite wettability. The relevant fluid-solid energy terms can then be calculated given the positions of the substrate-lubricant-drop and substrate-lubricant-gas contact lines.

In the case of full wetting, there are no substrate-lubricant-drop and substrate-lubricant-gas contact lines. Instead, the fluid-solid energy is accounted by numerically integrating the disjoining pressure term. In this case we ensure that the

lubricant layer has reached a constant thickness far away from the droplet in the case of full wetting. For this reason, we also apply a symmetric boundary condition with the external wall for the lubricant-gas interface. In the case of asymmetric LIS one needs only to consider different effective contact angles for the top and bottom plates.

2.3 Diffuse Interface Models

In Chapters 4 and 5 we will study ternary fluid de-wetting and ternary phase separation respectively. In our studies of ternary fluid de-wetting, we consider scenarios where we have a droplet detaching from a solid surface, due to displacement by an incoming fluid film. For phase separation we attempt to understand the *a priori* conditions which lead to the formation of different resulting morphologies. In both problems, the interfaces can evolve rapidly. It is easier and more appropriate to use a diffuse interface model, to avoid tracking the complicated evolution of the fluid interfaces.

2.3.1 Bulk Free Energy

As a starting point we need a bulk free energy that allows for three immiscible fluids. The ternary free energy model we base our numerical simulations is given below [106, 146],

$$E = \int \sum_{m=1}^{3} \frac{12}{\varepsilon} \frac{\Sigma_m}{2} \left(C_m^2 (1 - C_m)^2 + \frac{\varepsilon^2}{16} (\nabla C_m)^2 \right). \tag{2.7}$$

Here, the local concentration per unit volume for each fluid component m is given by C_m. The C_m's are the order parameters which we evolve and they range from 0 to 1. The constants, Σ_m, are related to the interfacial tensions between the fluid components, with $\gamma_{mn} = \frac{\Sigma_m + \Sigma_n}{2}$, where γ_{mn} is the interfacial tension between fluids m and n. For this model at equilibrium the interfacial profile, say between

fluid m and n, is given by

$$C_m(x) = \frac{1}{2}\left(1 + \tanh\left(\frac{2x}{\varepsilon}\right)\right) \tag{2.8}$$

$$C_n(x) = \frac{1}{2}\left(1 + \tanh\left(\frac{-2x}{\varepsilon}\right)\right), \tag{2.9}$$

where x is the displacement from the midpoint of the fluid interface between m and n. The midpoint of the interface is defined when $C_m = C_n = 0.5$. We can thus see that ε gives good measure for the interface width of the system.

We now must discuss how we obtain the equations of motion which govern how our simulations evolve in time. There are two sets of equations used. First, as we are studying fluid dynamics, we have the standard continuity and Navier-Stokes equations. If we denote time by t, the fluid density by ρ, and use Einstein summation convention on repeated indices, then the continuity equation is

$$\partial_t \rho + \partial_\alpha(\rho u_\alpha) = 0, \tag{2.10}$$

and the Navier Stokes equation is

$$\partial_t(\rho u_\alpha) + \partial_\beta(\rho u_\alpha u_\beta) = -\partial_\beta P_{\alpha\beta} + \partial_\beta \eta(\partial_\beta u_\alpha + \partial_\alpha u_\beta), \tag{2.11}$$

where α and β sum over the spatial coordinates. The pressure tensor $P_{\alpha\beta}$ contains the thermodynamic force that arises from the free energy in Eq. 2.7, and η is the dynamic viscosity.

Second we also have equations that govern the evolution of the order parameters. These are given by the Cahn-Hilliard equation. The specific terms of the Cahn-Hilliard equation depends on the model used, and they are written below in Sec. 2.3.1.1 and 2.3.1.2. We also employ the constraint $C_1 + C_2 + C_3 = 1$ to ensure the total concentrations sum to 1. There are several methods to ensure this constraint when solving the Cahn-Hilliard equation. We consider two approaches to solve this. One follows the method used by Semprebon et al. [146], where we coordinate-transform the concentrations and evolve the fluids in terms of the

auxiliary variables. The other approach is to follow Boyer et al. [106], where directly evolving the concentration values necessitate additional terms in the chemical potential to enforce the constraint. We will explain both approaches below.

2.3.1.1 Semprebon Approach

In Semprebon et al. [146], we make the following coordinate transformation of the concentration values,

$$C_1 = (\rho + \phi - \psi)/2 \qquad C_2 = (\rho - \phi - \psi)/2 \qquad C_3 = \psi, \tag{2.12}$$

with the inverse transformation being,

$$\rho = C_1 + C_2 + C_3, \qquad \phi = C_1 - C_2 \qquad \psi = C_3. \tag{2.13}$$

ϕ and ψ are auxiliary variables, and ρ is the fluid density which for our purposes is set to be the same and equal to 1 in simulation (dimensionless) units for all three components. We can see immediately the advantage of this model. Noticeably, ρ is the fluid density, the evolution of which is governed by the continuity and Navier-Stokes Equations. However, if one initialises the system with $\rho = 1$ then $C_1 + C_2 + C_3 = 1$ is immediately enforced.

This approach leads to the following set of Cahn-Hilliard equations,

$$\frac{\partial \phi}{\partial t} + \nabla \cdot (\phi \mathbf{u}) = \nabla \left(M_\phi \nabla \mu_\phi \right), \tag{2.14}$$

$$\frac{\partial \psi}{\partial t} + \nabla \cdot (\psi \mathbf{u}) = \nabla \left(M_\psi \nabla \mu_\psi \right). \tag{2.15}$$

The chemical potentials, are then obtained by taking the functional derivatives using the auxiliary variables. For detailed derivations please see Semprebon et al

[146]:

$$\begin{aligned}\mu_\phi &= \frac{\delta E}{\delta \phi} \\ &= \frac{12}{\varepsilon}\frac{\Sigma_1}{8}(\rho+\phi-\psi)(\rho+\phi-\psi-2)(\rho+\phi-\psi-1) \\ &\quad - \frac{12}{\varepsilon}\frac{\Sigma_2}{8}(\rho-\phi-\psi)(\rho-\phi-\psi-2)(\rho-\phi-\psi-1) \\ &\quad + \frac{\varepsilon^2}{16}\frac{1}{4}\frac{12}{\varepsilon}\left[(\Sigma_2-\Sigma_1)\left(\nabla^2\rho-\nabla^2\psi\right)-(\Sigma_1+\Sigma_2)\nabla^2\phi\right], \end{aligned} \tag{2.16}$$

$$\begin{aligned}\mu_\psi &= \frac{\delta E}{\delta \psi} \\ &= \frac{12}{\varepsilon}\frac{\Sigma_1}{8}(\rho+\phi-\psi)(\rho+\phi-\psi-2)(\rho+\phi-\psi-1) \\ &\quad - \frac{12}{\varepsilon}\frac{\Sigma_2}{8}\frac{12}{\varepsilon}(\rho-\phi-\psi)(\rho-\phi-\psi-2)(\rho-\phi-\psi-1) \\ &\quad + \frac{12}{\varepsilon}\Sigma_3\psi(\psi-1)(2\psi-1)+\frac{\varepsilon^2}{16}\frac{1}{4}\left[(\Sigma_1+\Sigma_2)\nabla^2\rho\right. \\ &\quad \left.-(\Sigma_2-\Sigma_1)\nabla^2\phi-(\Sigma_1+\Sigma_2+4\Sigma_3)\nabla^2\psi\right]. \end{aligned} \tag{2.17}$$

2.3.1.2 Boyer Approach

The other method follows Boyer et al. [106], where the Cahn-Hilliard equations are written in terms of the concentrations:

$$\frac{\partial C_m}{\partial t} + \nabla\cdot(C_m\mathbf{u}) = \nabla\left(\frac{M_o}{\Sigma_m}\nabla\mu_m\right) \tag{2.18}$$

$$\mu_m = -\frac{3}{4}\varepsilon\Sigma_m\nabla^2 C_m + \frac{12}{\varepsilon}(\Sigma_m H(C_m)+\beta). \tag{2.19}$$

Here,

$$H(C_m) = C_m(1-C_m)(1-2C_m), \tag{2.20}$$

$$\begin{aligned}\beta &= -\frac{6\Sigma_1\Sigma_2\Sigma_3}{\Sigma_1\Sigma_2+\Sigma_1\Sigma_3+\Sigma_2\Sigma_3}C_1C_2C_3 \\ &= -\delta C_1C_2C_3. \end{aligned} \tag{2.21}$$

In this approach the chemical potentials are modified with an extra term, β. This is in effect an interaction term which is only present when all three components are present, and serves to enforce the constraint $C_1 + C_2 + C_3 = 1$.

2.3.1.3 Comparing Semprebon and Boyer

Here we discuss the differences between the two approaches discussed in the preceding sub-sections. In the Boyer approach, all three components are treated symmetrically, and the reducibility of the model is analytically ensured [106]. When we mention reducibility we refer to the fact that if one of the components is set to be zero everywhere, the equations of motion reduce to the binary case. This can be seen explicitly by setting any of the C_m to be zero, in which case the associated chemical potential, μ_m, is set to zero uniformly.

However, if we were to do this with the Semprebon model, say $\psi = 0$, we instead obtain

$$\begin{aligned}
\mu_\psi &= \frac{\delta E}{\delta \psi} \\
&= \frac{12}{\varepsilon}\frac{\Sigma_1}{8}(\rho+\phi)(\rho+\phi-2)(\rho+\phi-1) \\
&\quad - \frac{12}{\varepsilon}\frac{\Sigma_2}{8}\frac{12}{\varepsilon}(\rho-\phi)(\rho-\phi-2)(\rho-\phi-1) \\
&\quad + \frac{\varepsilon^2}{16}\frac{1}{4}\frac{12}{\varepsilon}\Big[(\Sigma_1+\Sigma_2)\nabla^2\rho \\
&\quad -(\Sigma_2-\Sigma_1)\nabla^2\phi\Big] \\
&= \frac{12}{\varepsilon}\frac{\Sigma_1-\Sigma_2}{8}(1+\phi)(\phi-1)(\phi) \\
&\quad + \frac{\varepsilon^2}{16}\frac{1}{4}\frac{12}{\varepsilon}\Big[-(\Sigma_2-\Sigma_1)\nabla^2\phi\Big] \\
&= \frac{\Sigma_1-\Sigma_2}{4}\frac{12}{\varepsilon}\left[\frac{1}{2}(1+\phi)(\phi-1)\phi + \frac{\varepsilon^2}{16}\nabla^2\phi\right]. \qquad (2.22)
\end{aligned}$$

In general, the resulting chemical potential will be non-zero, except for $\Sigma_1 = \Sigma_2$. We now consider this term more carefully. Applying the inverse transformations and noting $\phi = 1 - C_1 = 2C_1 - 1$ when $C_3 = \psi = 0$ gives

$$\begin{aligned}
\mu_\psi &= \frac{\Sigma_1-\Sigma_2}{4}\frac{12}{\varepsilon}\left[2C_1(1-C_1)(1-2C_1) + 2\frac{\varepsilon^2}{16}\nabla^2 C_1\right] \\
&= \frac{\Sigma_1-\Sigma_2}{2}\left[\frac{12}{\varepsilon}C_1(1-C_1)(1-2C_1) + \frac{3}{4}\varepsilon\nabla^2 C_1\right]. \qquad (2.23)
\end{aligned}$$

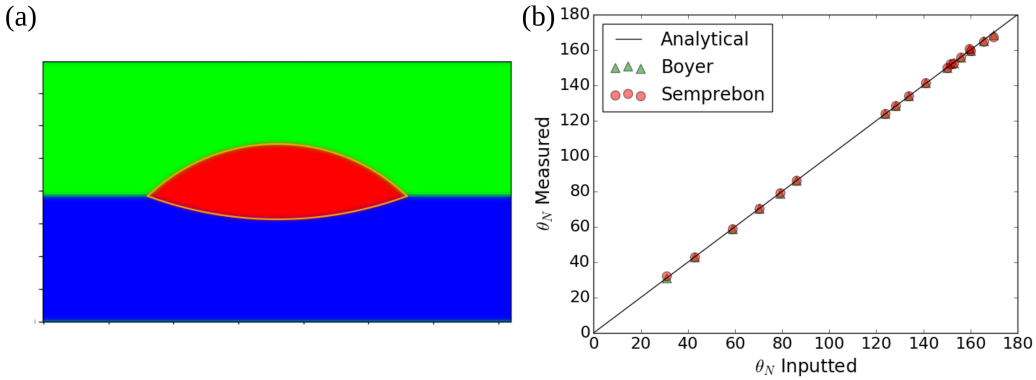

Figure 2.4: Panel (a) shows the liquid lens profile obtained from equilibrating a red droplet (fluid 1) between the green (fluid 2) and blue (fluid 3) fluids. We have chosen $\Sigma_1 = 0.01333$, $\Sigma_2 = 0.05333$, and $\Sigma_3 = 0.12$. Panel (b), we have plotted the measured Neumann angles for both the Semprebon and Boyer approaches, and compared them with the analytical Neumann angles, plotted as a solid line.

In fact, at equilibrium, where C_1 has a hyperbolic tangent profile, this term is a constant and zero. Hence, both the Semprebon and Boyer approaches are equivalent if we wish to study the steady or equilibrium states of the system we wish to study. For example, both approaches produce accurate Neumann angles when we benchmarked using a liquid lens morphology, see Fig. 2.4. In Fig. 2.4 (a) we show an example of the liquid lens morphology obtained for three fluids coloured in red, green and blue. The analytical profile of the equilibrium liquid lens shape is also highlighted in orange. Fig. 2.4 (b) shows the plot of the measured Neumann angles for both the Boyer and Semprebon approaches.

However, comparing the two approaches, we can observe some variations in the dynamic path towards equilibrium. For instance, show that the presence of C_3 is smaller using the Boyer approach when a droplet of C_1 surrounded by C_2 is initialised with a sharp interface Fig. 2.5. In Fig. 2.5, in the first row, Fig. 2.5 (a) - (c), we show the droplet (red) reaching equilibrium from a sharp interface initialisation. When observing the overall evolution of the dominant liquid components, we find no noticeable difference between the Semprebon and Boyer approaches. However, if we look at the evolution of C_3, we can see differences in the presence of C_3 as the simulation is evolved in time. In Fig. 2.5 (d) - (f) we show the evolution of C_3

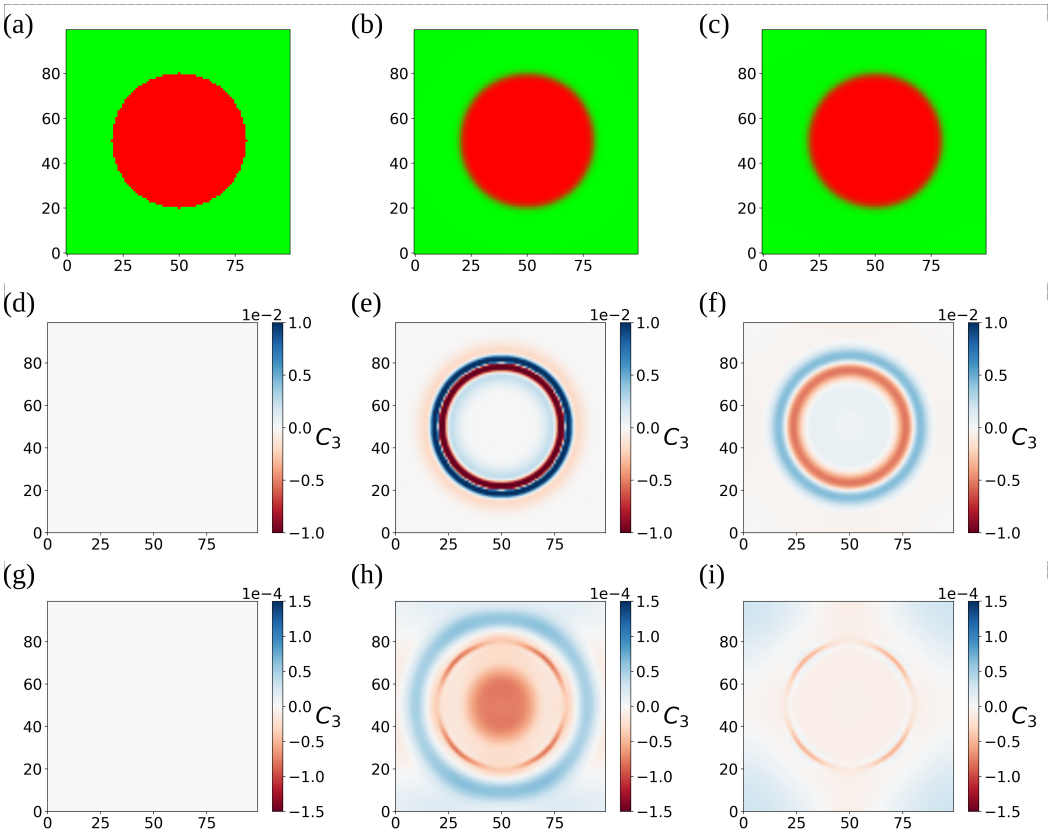

Figure 2.5: Panels (a) to (c) show the droplet from initialisation to equilibrium. In the second row (d) to (f) we display the value of C_3 as it evolves in time when using the Semprebon approach. Similarly, in the third row (g) to (i), we display the value of C_3 evolving in time using the Boyer approach. The first column shows the initialisation at timestep 0, the second column shows timestep at 1000, and the third column shows timestep at 10000. Here we have set $\Sigma_1 = 0.0003333$, $\Sigma_2 = 0.001$, and $\Sigma_3 = 0.0016667$.

using the Semprebon approach. Fig. 2.5 (g) - (i) show the results using the Boyer approach. We observe that presence of C_3 can reach a magnitude of the order 10^{-2} in the Semprebon approach, while in Boyer approach the presence of C_3 reaches a magnitude of the order 10^{-4}. We can thus conclude that the Boyer approach is more accurate. However, in the overall picture this does not necessarily have a large quantitative impact on the results as the Semprebon approach still gives accurate results to within $1\% - 2\%$.

2.3.2 Wetting Boundary Conditions

Thus far we have only mentioned the bulk fluid mechanics and thermodynamics. However, for the problems of interest in this thesis, we also need to consider the interaction between the fluids and solid boundaries. Throughout our work in our thesis we employ 4 categories of such boundary conditions. These are: the no slip boundary condition, inlet boundary conditions, outlet boundary conditions, and the wetting boundary conditions giving the contact angles. In this section we shall discuss the wetting boundary conditions but leave the numerical implementations of every other boundary condition in Lattice Boltzmann in Section 2.3.4.1. For the wetting boundary conditions, we use two methods: one based on the work of Dong [108], and one we term the Surface Energy method. Both of these are boundary conditions for the concentration values C_m.

2.3.2.1 Dong's Method

If we follow the method by Dong, the wetting boundary condition prescribes the relation

$$\mathbf{n} \cdot \nabla C_m|_S = \sum_{n=1}^{N} \xi_{mn} C_m C_n, \tag{2.24}$$

$$\xi_{mn} = -\frac{4}{\varepsilon} \cos\theta_{mn}, \tag{2.25}$$

where $\mathbf{n}$ is normal to the solid surface. The notation here is that the angle is measured from within fluid m when surrounded by fluid n. The antisymmetric condition $\xi_{mn} = -\xi_{nm}$ also holds.

2.3.2.2 Surface Energy Method

We also derive a separate method originating from a free energy form. Here, the free energy functional in Eq. 2.7 is extended to include surface energy contributions,

which only applies at the solid boundaries.

$$\begin{aligned} E &= \int_V \sum_{m=1}^{3} \frac{12}{\varepsilon}\frac{\Sigma_m}{2}\left[C_m^2(1-C_m)^2 + \frac{\varepsilon^2}{16}(\nabla C_m)^2\right]\ \mathrm{d}V \\ &+ \int_S \sum_{m=1}^{3} \lambda_m \left(\frac{1}{2}C_m^2 - \frac{1}{3}C_m^3\right)\ \mathrm{d}S \\ &= E_B + E_S, \end{aligned} \tag{2.26}$$

where E_B refers to bulk free energy and E_S the surface free energy term. In this method we introduce three variables to determine the solid surface interactions, λ_m, $m = 1, 2, 3$. It now remains to find how the different λ_m are determined as functions of the contact angles. Following standard methods of calculus of variations,

$$\frac{3}{4}\varepsilon\Sigma_m \mathbf{n}\cdot\nabla C_m\Big|_S = \lambda_m C_m(1-C_m) \tag{2.27}$$

To determine the values of λ_m, consider the surface energies of each component,

$$\begin{aligned} I_m &= \lambda_m\left(\frac{1}{2}C_m^2 - \frac{1}{3}C_m^3\right)\Big|_s \\ &= \frac{\lambda_m}{6}. \end{aligned} \tag{2.28}$$

Therefore

$$\gamma_{sm} = \frac{\lambda_m}{6}. \tag{2.29}$$

From the definition of the Young's Equation we then find

$$\cos\theta_{mn} = \frac{\gamma_{sn} - \gamma_{sm}}{\gamma_{mn}} \tag{2.30}$$

$$= \frac{\lambda_n - \lambda_m}{3(\Sigma_m + \Sigma_n)} \tag{2.31}$$

Solving the equations algebraically, and noting the Girifalco-Good relation we only have two independent equations. As such one λ_m is inevitably a free parameter, Choosing λ_3 as the free parameter, we define

$$\lambda_1 = 3(\Sigma_3 + \Sigma_1)\cos\theta_{31} + \lambda_3 \tag{2.32}$$

$$\lambda_2 = 3(\Sigma_2 + \Sigma_3)\cos\theta_{32} + \lambda_3 \tag{2.33}$$

For concreteness, we typically choose $\lambda_3 = 0$.

In the transformed coordinate system, $\rho = C_1 + C_2 + C_3$, $\phi = C_1 - C_2$, $\psi = C_3$, and the gradient condition becomes

$$\mathbf{n} \cdot \nabla \rho|_s = \frac{4}{3\varepsilon} \left(\frac{\lambda_1 C_1 (1 - C_1)}{\Sigma_1} + \frac{\lambda_2 C_2 (1 - C_2)}{\Sigma_2} + \frac{\lambda_3 C_3 (1 - C_3)}{\Sigma_3} \right), \tag{2.34}$$

$$\mathbf{n} \cdot \nabla \phi|_s = \frac{4}{3\varepsilon} \left(\frac{\lambda_1 C_1 (1 - C_1)}{\Sigma_1} - \frac{\lambda_2 C_2 (1 - C_2)}{\Sigma_2} \right), \tag{2.35}$$

$$\mathbf{n} \cdot \nabla \psi|_s = \frac{4}{3\varepsilon} \left(\frac{\lambda_3 C_3 (1 - C_3)}{\Sigma_3} \right). \tag{2.36}$$

In both the surface energy method and Dong's method the boundary conditions are implemented by setting concentration value of boundary nodes to ensure the normal gradient conditions are met. To do this we consider the inverting finite difference method (central difference approach),

$$\left. \frac{\partial C_m}{\partial x} \right|_b = \frac{C_{m1} - C_{m2}}{\Delta x}, \tag{2.37}$$

to obtain

$$C_{m2} = C_{m1} - \Delta x \left. \frac{\partial C_m}{\partial x} \right|_b. \tag{2.38}$$

C_{m1} and C_{m2} are defined as shown in Fig. 2.6, and Δx is the distance from C_{m1} and C_{m2}. Here $\frac{\partial C_m}{\partial x}$ is determined by the methods we have described. For surface energy method,

$$\left. \frac{\partial C_m}{\partial x} \right|_b = \frac{4}{3\varepsilon} \frac{\lambda_m C_m (1 - C_m)}{\Sigma_1}, \tag{2.39}$$

while for Dong's method,

$$\left. \frac{\partial C_m}{\partial x} \right|_b = \sum_{n=1}^{N} \xi_{mn} C_m C_n. \tag{2.40}$$

2.3.2.3 Comparing Wetting Boundary Conditions

In this section we discuss in detail the differences between the two methods. As an example, consider the conditions for C_3 when we consider it explicitly as $C_3 =$

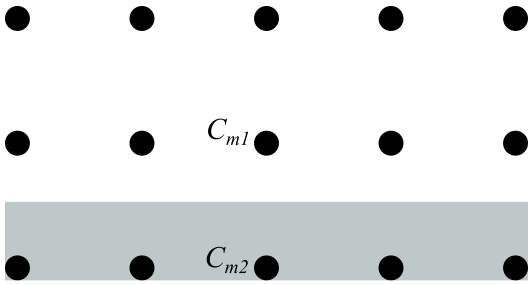

Figure 2.6: Here we show a lattice of nodes, with the grey area representing a solid surface. Two adjacent nodes C_{m1} and C_{m2} are highlighted. Note the physical boundary of the solid is between the nodes simulated.

$1 - C_1 - C_2$. This of course would also imply $\nabla C_3 = -\nabla C_1 - \nabla C_2$.

$$\mathbf{n} \cdot \nabla C_3 = \xi_{31} C_1 (1 - C_1 - C_2) + \xi_{32} C_2 (1 - C_1 - C_2) \tag{2.41}$$

$$\mathbf{n} \cdot \nabla C_1 = \xi_{12} C_1 C_2 + \xi_{13} C_1 (1 - C_1 - C_2) \tag{2.42}$$

$$\mathbf{n} \cdot \nabla C_2 = \xi_{21} C_1 C_2 + \xi_{23} C_2 (1 - C_1 - C_2) \tag{2.43}$$

Relating the boundary conditions, we can explicitly show that the constraint above is satisfied:

$$\begin{aligned} -\mathbf{n} \cdot \nabla C_1 - \mathbf{n} \cdot \nabla C_2 &= -\xi_{12} C_1 C_2 - \xi_{13} C_1 (1 - C_1 - C_2) \\ &\quad - \xi_{21} C_1 C_2 - \xi_{23} C_2 (1 - C_1 - C_2) \\ &= \xi_{31} C_1 (1 - C_1 - C_2) + \xi_{32} C_2 (1 - C_1 - C_2) \\ &= \mathbf{n} \cdot \nabla C_3, \end{aligned} \tag{2.44}$$

where we have also used the antisymmetric relation $\xi_{mn} = -\xi_{nm}$.

However, when we attempt to do this for the surface energy method we obtain a slight error.

$$\begin{aligned} \frac{3}{4} \varepsilon \mathbf{n} \cdot \nabla C_3 &= \frac{\lambda_3}{\Sigma_3} (1 - C_1 - C_2)(C_1 + C_2) \\ &= \frac{\lambda_3}{\Sigma_3} \left(C_1 + C_2 - C_1^2 - C_2^2 - 2 C_1 C_2 \right) \\ &= \frac{\lambda_3}{\Sigma_3} \left(C_1 (1 - C_1) + C_2 (1 - C_2) - 2 C_1 C_2 \right) \\ &= \frac{\lambda_3}{\Sigma_3} \left[\frac{3}{4} \varepsilon \frac{1}{\lambda_1} \mathbf{n} \cdot \nabla C_1 + \frac{3}{4} \varepsilon \frac{1}{\lambda_2} \mathbf{n} \cdot \nabla C_2 - 2 C_1 C_2 \right] \end{aligned} \tag{2.45}$$

Notice that even if we choose a tailored value for ϕ_3 we will not be able to perfectly satisfy the constraint, due to the presence of cross terms.

It is clear, that if our objective is to obtain accurate contact angles it would be best to use the form by Dong. However, due to the existence of cross terms, to the best of our knowledge, there are no simple mathematical forms for the surface energy density which would reproduce the conditions by Dong. If the explicit surface energy contributions need to be calculated, then the surface energy method is the only viable option.

2.3.3 Comparing Contact Angle Models

We will highlight the differences between the two contact angle methods, by studying a droplet equilibrating on a corrugated surface, as shown in Fig. 2.7. Fig. 2.7 (a) shows the initial configuration which always the same: a droplet (in red) surrounded by the green fluid on a corrugated surface. Then Fig. 2.7 (b) shows the droplet equilibrium of evolving using the Semprebon bulk approach with contact angles derived from the Surface Energy method; Fig 2.7 (c) shows the equilibrium state using Semprebon bulk approach with boundary conditions derived from Dong's method; and finally Fig. 2.7 (d) shows the case of Boyer bulk approach with boundary conditions derived from Dong's method. We can see from Fig. 2.7 (b) that reducibility is no longer well preserved, as the blue fluid creeps in from the corners of the corrugation. We find this issue to be significantly diminished on flat surfaces, and is only apparent in more complicated surface geometries. Fig. 2.7 (c) and (d) show little difference between them which suggests the main issue with reducibility is due to the way we determine surface boundary conditions, rather than the reducibility of the bulk model.

We also measure the droplet contact angles vs the theoretical contact angles on a flat surface, and compare them against theoretical predictions for (i) the Semprebon bulk approach with Dong boundary conditions and (ii) the Boyer bulk

approach with Dong boundary conditions. The results are shown in Fig. 2.8. In both cases the contact angles agree well above $\theta_c = 20°$ and below $\theta_c = 150°$. In fact, the Boyer approach with Dong boundary conditions seems to be still very accurate even up to a contact angle of $\theta_c = 170°$. In summary, it is clear that the bulk fluid model has minimal effect on the accuracy of the measured contact angle, as such both methods can be used reliably. Due to the superior reducibility properties of the Boyer approach, one might come to the conclusion that the Boyer with Dong boundary conditions is the superior approach. However, we find that the Semprebon bulk approach is more stable across a larger range of viscosity ratios, as such when large viscosity ratios are modelled it is superior to use the Semprebon approach.

We conclude that when the accuracy of contact angles and Neumann angles are the only metrics to consider, it is the superior choice to use Boyer bulk approach with Dong boundary conditions. However, since the Semprebon bulk model is more numerically stable for varying viscosities Semprebon model with Dong boundary conditions is also more numerically stable when we take into account viscosity variation. Hence, in cases where we also want to study the effects of viscosity and gravity it was more optimal to use the Semprebon bulk approach with Dong boundary conditions. Finally, it is worth noting that, if we decide to use an energy minimisation method, we cannot use Dong boundary conditions as there is no simple form to calculate the surface energy density. The step is crucial for the energy minimisation method we use. See the thesis by Panter, [147] for the details about the implementation of the energy minimisation procedure.

2.3.4 Lattice Boltzmann Implementation

We solve the, continuity, Navier-Stokes and Cahn-Hilliard equations using the lattice Boltzmann approach. We shall show the Boyer model implementation here, the Semprebon model is effectively the same but with different variables, see Semprebon et al [146].

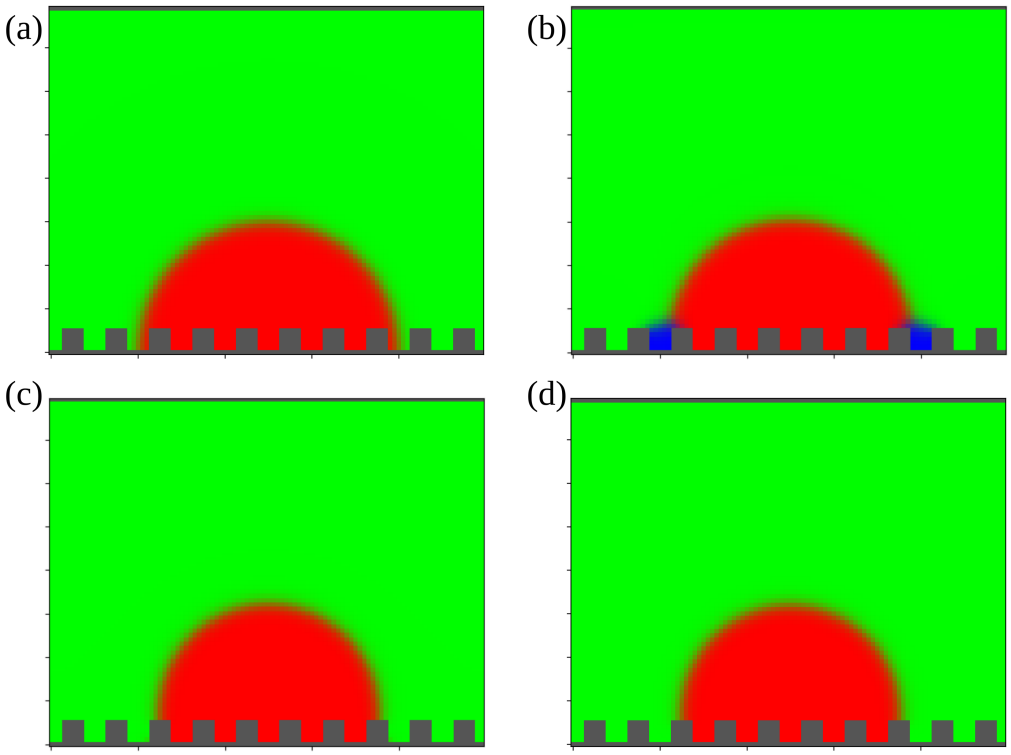

Figure 2.7: Panel (a) shows the initialisation of a droplet on a corrugated surface; (b) shows the equilibrated result, using the surface energy contact angle, with Semprebon bulk approach; (c) shows the result of Semprebon bulk approach with Dong boundary conditions; (d) shows the result of Boyer model with Dong boundary conditions. In all cases we have set contact angles of $\theta_{12} = 90°$ and $\theta_{31} = 30°$. For (b) and (c) $\Sigma_m = 0.0033333$ for $m = 1, 2, 3$, while for (d) we have $\Sigma_1 = 0.0033333$, $\Sigma_2 = 0.013333$, and $\Sigma_3 = 0.03$. By comparing cases (b) and (d) show that surface energy method is causing the spurious growth of the third component (blue), while the lack of spurious growth of the third component in (c) despite non-equal surface tensions shows that the bulk irreducibility of the Semprebon model is not signficant in causing spurious growth at the boundaries.

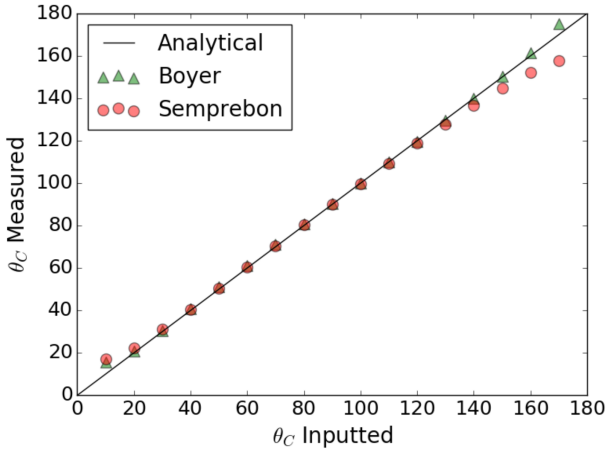

Figure 2.8: Results for using and Dong's method contact angles, when combined with the differing bulk models.

To begin with we will give a background on the lattice Boltzmann method. In the lattice Boltzmann method, we focus on evolving the distribution functions f_i whose moments are the physical quantities of relevance, such as the density and momentum:

$$\rho = \sum_i f_i \qquad\qquad \rho\mathbf{u} = \sum_i \mathbf{c}_i f_i. \tag{2.46}$$

Each lattice Boltzmann scheme has a chosen stencil for the velocity discretization of the distribution functions. The direction related to each distribution function is given by a lattice vector $\mathbf{c}_i$, which will depend on the stencil used. The ones we use are D2Q9 and D3Q19. See Fig. 2.9 for a pictorial representation of each lattice vector in relation to the standard Cartesian directions, in both for D2Q9 and D3Q19 lattices.

In addition to the lattice vectors each distribution function is associated with a weighting factor, w_i. Combining all these together we can present a table detailing the weightings and the lattice vectors for both lattice stencils. See Tab. 2.1 for the D2Q9 stencil, and Tab. 2.2 for the D3Q19 stencil.

We use the Bhatnagar-Gross-Krook (BGK) collision operator to evolve the

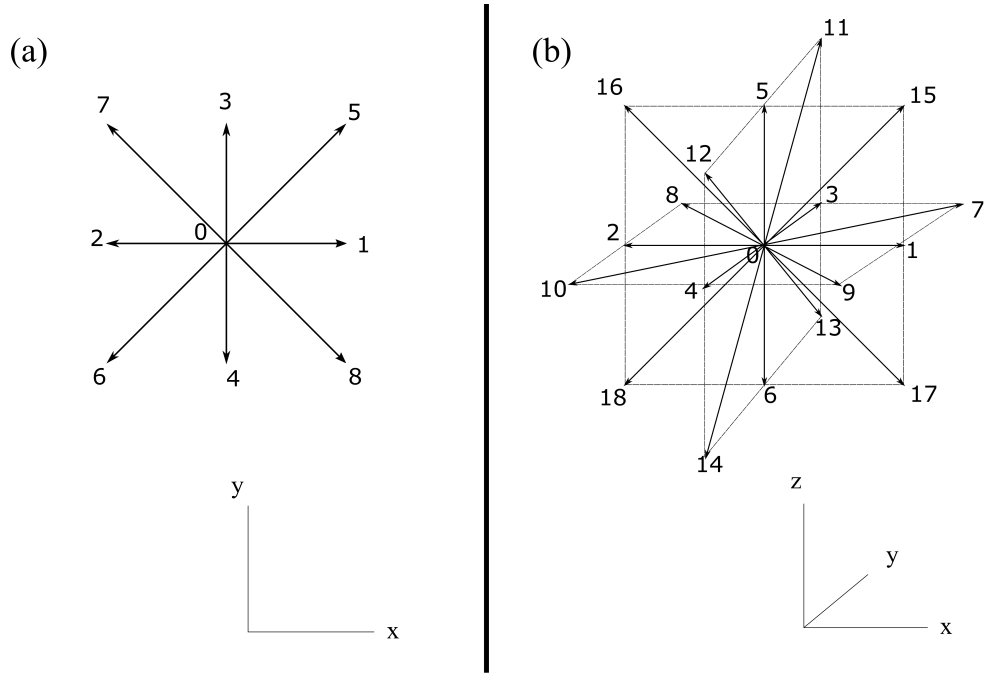

Figure 2.9: Here we highlight the lattice vectors for both (a) D2Q9 and (b) D3Q9 lattices. Underneath both we also highlight the Cartesian coordinate frame used.

i	Cartesian vector	w_i
c_0	$(0, 0)$	$4/9$
c_1	$(1, 0)$	$1/9$
c_2	$(-1, 0)$	$1/9$
c_3	$(0, 1)$	$1/9$
c_4	$(0, -1)$	$1/9$
c_5	$(1, 1)$	$1/36$
c_6	$(-1, -1)$	$1/36$
c_7	$(-1, 1)$	$1/36$
c_8	$(1, -1)$	$1/36$

Table 2.1: This table summarises the lattice vectors for the D2Q9 stencil. The first column gives the lattice vector corresponding to the distribution function i, with the second column describing the lattice vector given in Cartesian coordinates, and the third column describing the corresponding lattice weighting.

i	spatial vector	w_i
c_0	$(0,0,0)$	$1/3$
c_1	$(1,0,0)$	$1/18$
c_2	$(-1,0,0)$	$1/18$
c_3	$(0,1,0)$	$1/18$
c_4	$(0,-1,0)$	$1/18$
c_5	$(0,0,1)$	$1/18$
c_6	$(0,0,-1)$	$1/18$
c_7	$(1,1,0)$	$1/36$
c_8	$(-1,1,0)$	$1/36$
c_9	$(1,-1,0)$	$1/36$
c_{10}	$(-1,-1,0)$	$1/36$
c_{11}	$(0,1,1)$	$1/36$
c_{12}	$(0,-1,1)$	$1/36$
c_{13}	$(0,1,-1)$	$1/36$
c_{14}	$(0,-1,-1)$	$1/36$
c_{15}	$(1,0,1)$	$1/36$
c_{16}	$(-1,0,1)$	$1/36$
c_{17}	$(1,0,-1)$	$1/36$
c_{18}	$(-1,0,-1)$	$1/36$

Table 2.2: This table summarises the lattice vectors for the D3Q19 stencil. The first column gives the lattice vector corresponding to the distribution function i, with the second column describing the lattice vector given in Cartesian coordinates, and the third column describing the corresponding lattice weighting

distribution functions

$$f_i(\mathbf{x} + \mathbf{c}_i\Delta t) = f_i(\mathbf{x}, t) - \frac{f_i(\mathbf{x}, t) - f_i^{eq}(\mathbf{x}, t)}{\tau}\Delta t + F_i. \tag{2.47}$$

There are two main parts to the above equation, the collision and streaming steps. To implement this numerically, one can consider the two steps separately. At each lattice node, denoted by $\mathbf{x}$, we can calculate the collision step, which is the right-hand side of Eq. 2.47. Then we stream the distribution functions by moving them to the nodes they point to according to their associated lattice vector, c_i. We give a pictorial representation of the streaming step in Fig. 2.10 for D2Q9. Finally we also have a forcing term, F_i, which here captures contributions from external body forces.

When looking at the LBM equation in Eq. 2.47, we still need to determine the equilibrium distribution functions, f_i^{eq}. There are several choices for this. Here, we

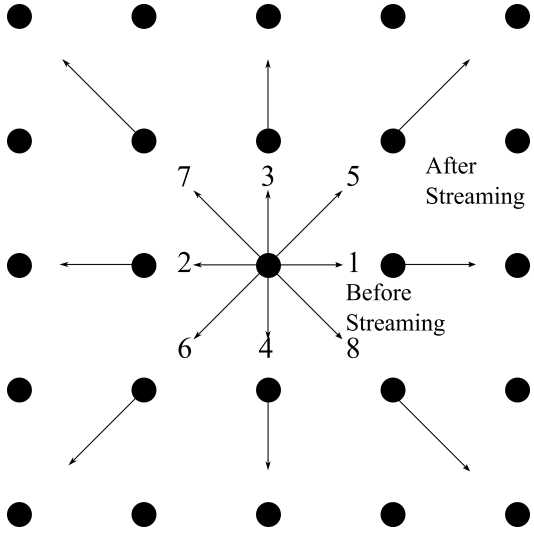

Figure 2.10: The above figure highlights the lattice stencil centred on one lattice node. Here, the lattice vectors are also highlighted f_{1-8} pointing to the nodes they will stream to.

use the pressure tensor approach, where the thermodynamic forces resulting from the fluid free energy is absorbed into the pressure tensor. This pressure tensor, $P_{\alpha\beta}$, is the same as the pressure tensor which goes into the Navier-Stokes equation. The pressure tensor is related to the chemical potential by the following,

$$\partial_\beta P_{\alpha\beta} = \partial_\alpha p + \sum_{m=1}^{3} \left[C_m \partial_\alpha \mu_m \right], \tag{2.48}$$

where $p = \rho c_s^2$ is the ideal gas pressure, as is standard in the lattice Boltzmann method. This leads to the pressure tensor being given by

$$\begin{aligned} P_{\alpha\beta} = &\left[p_b + \beta - \sum_{m=1}^{3} \frac{3}{4} \varepsilon \Sigma_m \left(\frac{1}{2} (\partial_\gamma C_m)^2 + C_m \partial_\gamma \partial_\gamma C_m \right) \right] \delta_{\alpha\beta} \\ &+ \sum_{m=1}^{3} \frac{3}{4} \varepsilon \Sigma_m (\partial_\alpha C_m)(\partial_\beta C_m), \end{aligned} \tag{2.49}$$

where

$$p_b = \rho c_s^2 + \sum_{m=1}^{3} \left(\frac{1}{2} \frac{12}{\varepsilon} \Sigma_m C_m^2 (1 - C_m)(1 - 3C_m) \right). \tag{2.50}$$

In the pressure tensor approach, the thermodynamic force enters the lattice Boltzmann

equation via the equilibrium distribution functions for the density,

$$f_i^{eq} = w_i\rho\left(\frac{c_{i\alpha}u_\alpha}{c_s^2} + \frac{u_\alpha u_\beta\left(c_{i\alpha}c_{i\beta} - c_s^2\delta_{\alpha\beta}\right)}{2c_s^4}\right) + \frac{w_i}{c_s^2}\left(p_b + \beta - \frac{3}{4}\varepsilon\sum_{m=1}^{3}\Sigma_m C_m \Delta C_m\right) + \frac{3}{4}\varepsilon\sum_{m=1}^{3}\Sigma_m\sum_{\alpha,\beta} w_i^{\alpha\beta}(\partial_\alpha C_m)(\partial_\beta C_m). \tag{2.51}$$

For all the above equations the spatial gradient terms are determined using finite difference.

In our work, we also choose to solve the Cahn-Hilliard equations using the lattice Boltzmann method, one for each fluid component. The evolution of the distribution functions, g_{mi}, for each concentration, C_m, is given by

$$g_{mi}(\mathbf{x} + \mathbf{c}_i\Delta t) = g_{mi}(\mathbf{x}, t) - \frac{g_{mi}(\mathbf{x}, t) - g_{mi}^{eq}(\mathbf{x}, t)}{\tau}\Delta t.$$

The equilibrium distribution function g_{mi}^{eq} is then given by

$$g_{mi}^{eq} = w_i\left(\frac{\Gamma_j\mu_m}{c_s^2} + \frac{C_m c_{i\alpha}u_\alpha}{c_s^2} + \frac{C_m u_\alpha u_\beta\left(c_{i\alpha}c_{i\beta} - c_s^2\delta_{\alpha\beta}\right)}{2c_s^4}\right), \tag{2.52}$$

where to obtain correctly scaled mobilities (M_m in the Cahn-Hilliard equation),

$$M_m = \frac{M_0}{\Sigma_m} = \Gamma_m\left(\tau_m - \frac{\Delta t}{2}\right), \qquad \Gamma_m = \frac{M_0}{\Sigma_m}\left(\frac{2}{2\tau_m - \Delta t}\right). \tag{2.53}$$

We now discuss how external non-thermodynamic forces are incorporated into the lattice Boltzmann equation. There are several methods to do this but we shall choose the exact difference method. In this case, the forcing contribution, for each distribution function f_i, can be written as

$$F_i = f_i^{eq}(\mathbf{u} + \Delta\mathbf{u}) - f_i^{eq}(\mathbf{u}). \tag{2.54}$$

The external body force, $\mathbf{F}$ such as gravity is implemented through $\Delta\mathbf{u} = \mathbf{F}\Delta t/\rho$.

2.3.4.1 Lattice Boltzmann Boundary Conditions

We have so far detailed how the lattice Boltzmann method works in the bulk fluids. We must also consider boundary conditions. The simplest boundary conditions we use are the periodic boundary and symmetry boundary conditions. With periodic boundary conditions, we simply treat the end nodes as if they are adjacent to the other side of the simulation domain. For symmetry boundary conditions we define axes of symmetry and then treating the nodes at the symmetry boundary to be adjacent to themselves. Additionally, we often require three other boundary conditions: bounce-back for ensuring no-slip boundary conditions at the solid walls, inlet boundary condition, and outlet boundary condition.

The no-slip boundary condition is a boundary condition for the velocity of the fluid, which is set to zero at the solid boundaries, (more generally, the same velocity as the solid)

$$\mathbf{u}|_S = 0, \tag{2.55}$$

where S denotes the solid surface.

In lattice Boltzmann we use the bounce-back boundary condition to implement this. It should be clear that within the bulk after the streaming step there are no issues, but when streaming at the nodes adjacent to the boundaries we are missing several distribution functions as they cannot be streamed from solid boundaries. For example, in Fig. 2.11, for the lattice nodes adjacent to the solid surface, after streaming we will be missing the distribution functions f_3, f_5 and f_7. To determine these distribution functions we will use the bounce-back condition [148, 149] gives

$$f_3(\mathbf{x}) = f_4^*(\mathbf{x}) \tag{2.56}$$

$$f_5(\mathbf{x}) = f_6^*(\mathbf{x}) \tag{2.57}$$

$$f_7(\mathbf{x}) = f_8^*(\mathbf{x}). \tag{2.58}$$

We use the asterisk to denote the distribution functions that are computed after the collision step, but before streaming. For other solid boundary orientations,

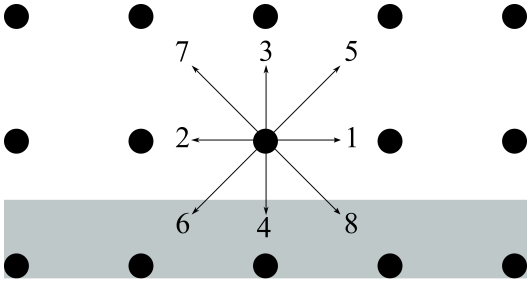

Figure 2.11: In this figure we show in grey the solid boundaries. The black circles represent the lattice nodes. The real edge of the solid boundary lies between the two layers of nodes.

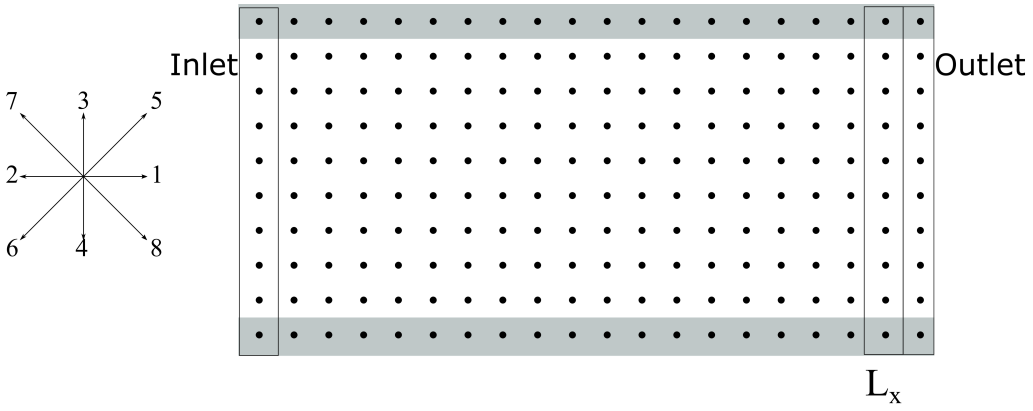

Figure 2.12: We show a channel flanked by solid boundaries shown in grey at the top and bottom, with the inlet on the left and outlet on the right. We also show the D2Q9 lattice vectors for the LBM method which will be present at every node.

the bounce-back boundary condition can be used in a similar manner. It also also extends naturally to the case with D3Q19 lattice. For further details about the bounce-back boundary, see [148, 149].

In cases where we use an inlet boundary condition, we set the inlet velocity profile, which remains fixed throughout time. For simplicity, we use a constant velocity profile,

$$\mathbf{u}|_I = v_{in}, \tag{2.59}$$

where the subscript I denotes the inlet, and v_{in} is the inlet velocity. In principle we could use a varying velocity profile, but for our purposes this would not have a significant impact on the flow physics. We are primarily interested in introducing new fluid to the simulation domain. In addition to setting the velocity, we also pre-

scribe density and concentration values at the inlet which remain fixed throughout time.

Similar to the bounce-back boundary condition, at the macroscopic level, the inlet boundary condition is straightforward, equivalent to setting the velocity and concentration values at the inlet nodes. But as with the bounce-back condition, we are missing distribution functions at the propagation step in the lattice Boltzmann algorithm. As an example, consider a lattice point in the middle of the channel at the inlet, see Fig. 2.12. After the streaming step, such a node will be missing the f_1,f_5 and f_8 distribution functions. We now must determine how to calculate these. If we set the inlet velocities to be only acting in the x-direction, u_x, from the moments of the distribution functions we have

$$\begin{aligned} f_0 + f_1 + f_2 + f_3 + f_4 + f_5 + f_6 + f_7 + f_8 &= \rho, \\ f_1 + f_5 + f_8 &= \rho - (f_2 + f_3 + f_4 + f_6 + f_7) = f^*. \end{aligned} \tag{2.60}$$

We now make a choice to weigh the distribution function according to their lattice weights [150]. Thus we have,

$$f_i = \frac{w_i f^*}{w_1 + w_5 + w_8}, \qquad i = 1, 5, 8. \tag{2.61}$$

This can similarly be applied to g_{mi}, corresponding to distribution functions for the concentration order parameters.

For the outlet boundary condition, we use the convective boundary condition to ensure the correct outgoing flux is determined for each relevant variable, χ,

$$\partial_t \chi + U \partial_\alpha \chi = 0, \tag{2.62}$$

where U is the characteristic velocity chosen. There are several choices possible, including, the average velocity, the local velocity, and the maximum velocity, [151]. In our case we choose to use the average velocity.

As with the inlet node layer we can observe we have missing distribution functions. However, unlike for inlet boundary condition we use two outlet layers. The

L_x layer, see Fig. 2.12 is treated as the final full lattice Boltzmann layer. In this layer for the missing distribution functions after streaming, we determine them using

$$f_i(L_x, y, t + \Delta t) = \frac{f_i(L_x, y, t) + U(L_x - 1, y, t) f_i(L_x - 1, y, t)}{1 + U(L_x - 1, y, t)}. \tag{2.63}$$

This is essentially the discretized version of Eq. 2.62. Similar equations are also used for the g_{mi} distribution functions.

The outermost layer at $L_x + 1$ is a ghost layer. No collision and streaming is calculated here. Its purpose is to provide values for the fluid concentrations to allow for the calculation of gradients for the outlet layer. Using the convective boundary condition, this is given by

$$\rho(L_x + 1, y, t + \Delta t) = \frac{\rho(L_x + 1, y, t) + U(L_x, y, t) \rho(L_x, y, t)}{1 + U(L_x, y, t)}. \tag{2.64}$$

for the density, and the similarly for the concentration values.

Chapter 3

Sticky SLIPS

3.1 Introduction

The subject of capillary bridges has received much attention in the literature due to their ubiquity in nature and engineering applications. For example, capillary bridges between parallel flat plates [37, 152, 153] have been considered for applications in liquid transfer [58, 59], wet adhesion device [56, 57], and for the formation of curved polymeric particles [154], while those between curved solid bodies [155, 156, 157] occur in wet granular materials [158, 159] and in atomic force microscopy experiments [160, 161, 162]. Capillary bridges also play important roles in the physiology of numerous insects and animals, such as in the adhesive pads of Asian Weaver ants [163, 164] and how shorebirds trap and consume prey inside their beaks [165]. Furthermore, the stability of liquid bridge shapes and their force-separation relations have been investigated for smooth and patterned surfaces [55, 166, 167, 168], as well as in the presence of one and multiple droplets [168, 169, 38].

In contrast to previous works, where the capillary bridges comprise of a single liquid component, here we study the case where they have two liquid components, especially in the context of the so-called liquid infused surfaces (LIS) or slippery liquid infused porous surfaces (SLIPS). These are a novel class of functional surfaces

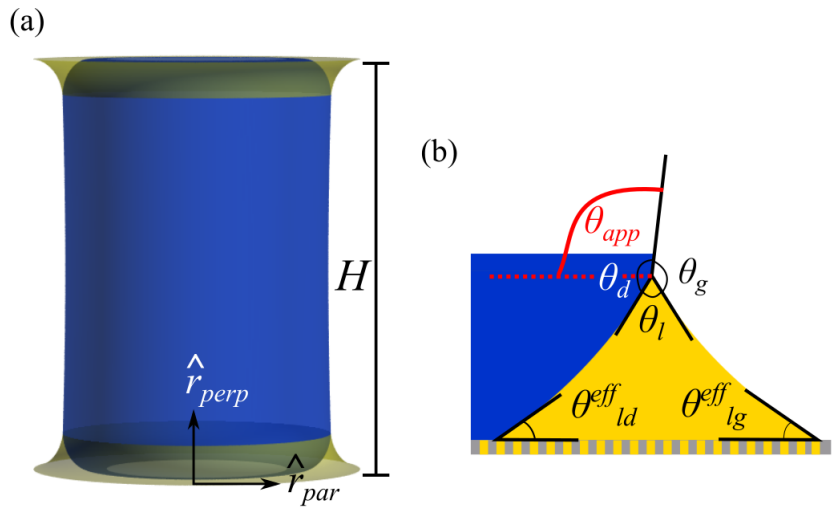

Figure 3.1: We once again highlight the key features of the LIS model. Here, a capillary bridge is formed between two LIS surfaces separated by a distance H, as shown in (a). In (b) we show the various relevant angles, including: the Neumann angles, θ_l, θ_d, and θ_g; the effective contact angles θ^{eff}_{ld}, θ^{eff}_{lg}; and the apparent contact angle highlighted in red, θ_{app}.

constructed by infusing textured or porous materials with wetting lubricants [76, 77, 78]. LIS can be considered as being an alternative to superhydrophobic surfaces [170, 35, 78], with the key difference of a lubricant layer being present. This difference has one key disadvantage which is the depletion of the lubricant over time [92], and can be considered the key problem to be overcome for LIS to become a reliable and tested technology.

Many applications of LIS exploit the fact that, on LIS, liquids move easily parallel to the substrate [76, 77, 78, 171, 172, 173, 174]. This "slippery" nature results in numerous advantageous properties, such as self-cleaning, enhanced heat transfer, anti-fouling, and anti-icing. Here, we focus instead on the adhesive properties of droplets when displaced perpendicularly to the substrate. Since the adhesive force now has contributions which originate not just from the liquid droplet but also from the lubricant, we will argue that LIS are "sticky" in the perpendicular direction.

To study capillary adhesion on LIS, we will consider a liquid droplet sandwiched

between two parallel LIS, as illustrated in Fig. 3.1 (a). For simplicity, we assume that gravity is negligible and consider symmetric surface properties such that the Neumann (θ_l, θ_d and θ_g) and wetting contact angles (θ_{ld}^{eff} and θ_{lg}^{eff}), illustrated in Fig. 3.1 (b) , will be the same for the top and bottom plates. In our studies, we focus on equilibrium rather than dynamic effects, obtained by quasi-statically varying the separation between the substrates. As we will show later the shape of the capillary bridge plays a key role in the capillary bridge morphologies and capillary forces and as such we expect that the addition of gravity could have a significant effect in cases where the droplet size is greater than the capillary length of the droplet. The addition of gravity can be easily implemented numerically but that was not the focus in this thesis.

The fact that capillary bridges on LIS involve two liquid components, instead of just one, leads to several interesting phenomena. Firstly, two-component liquid bridges can exhibit a wider range of interfacial morphologies and topologies. Morphological transitions can be triggered by compressing and stretching the capillary bridges. Secondly, to characterise the "stickiness" of LIS, we calculate the capillary force. To demonstrate he increase in "stickiness" is not due to a simple additional contribution, we also study the effective spring constant of the capillary bridges. We find both the size and shape of the lubricant ridge to play an important role. In the limit of vanishing ridge size, we observe that the adhesion force converges to that of a perfectly smooth surface. Since perfectly smooth surfaces are challenging to realise, LIS can be considered as an excellent alternative to mimic their properties in the limit of small ridge. Additionally, LIS can also be tuned to have stronger adhesion than an equivalent smooth surface.

3.2 Study of capillary bridges between liquid infused surfaces

In our studies we performed systematic numerical energy minimization, using Surface Evolver, varying the plate separation H, the apparent contact angle θ_{app} [139], the lubricant Neumann angle θ_l, and the lubricant pressure ΔP_{lg}. Also in the studies shown here we focus on the so-called pressure ensemble, when determining the volume of the lubricant ridge. In effect we control the size of the lubricant ridge by setting the pressure difference between the lubricant ridge and surrounding gas,P_{lg}, as a constant, while we minimise the free energy, with respect to the other variables. In principle we could had set the volume of the lubricant ridge, V_l, to be a constant. Both would produce valid results but we believe the pressure ensemble reflects a more intuitive understanding. This is because, if one would experimentally measure the behaviour of a droplet sandwiched between liquid-infused surfaces, it would be much more intuitive to set the volume of the droplet, but almost impossible to fix the volume of lubricant ridge which would inevitably form.

3.2.1 Morphology Classes

We begin by classifying the various capillary bridge morphologies we observed. One can broadly group the bridge morphologies on LIS into three categories. Referring to panels in Fig. 3.2 these are: (a-b) unstable bridges due to envelopment instability, (c-f) stable bridges, and (g-h) unstable bridges due to capillary break up or detachment. We must note here that envelopment is different from the lubricant cloaking or encapsulating the droplet. In these cases the spreading parameter, $S = \gamma_{dg} - \gamma_{lg} - \gamma_{ld} > 0$, and as such it is not stable for the three fluids to meet at a triple contact line forming Neumann angles. Instead, the lubricant forms a thin layer around the droplet. Envelopment on the other hand is when the droplet is

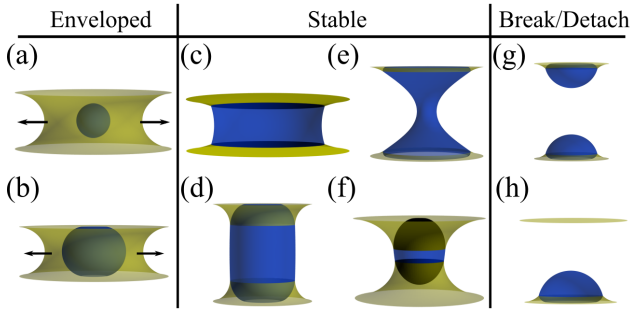

Figure 3.2: Three broad categories of the energy minimization results. The top and bottom rows illustrate the typical morphologies for hydrophilic ($\theta_{app} < 90°$) and hydrophobic ($\theta_{app} > 90°$) capillary bridges, respectively, with the exception of (a) and (b) which can occur for both cases. First, at small separation, the capillary bridge is unstable and the droplet is enveloped by the lubricant. Here, the droplet can be (a) detached from or (b) attached to the substrates. The droplet is attached to the substrate when the blue droplet makes contact the solid surface of the LIS, detached when the droplet no longer makes contact with the surface. Second, stable capillary bridges are formed. For hydrophilic bridges, the droplet can be (c) detached from both substrates or (e) attached to both substrates; while for hydrophobic bridges, the droplet can be (d) attached to both substrates or (f) attached to only one substrate. Third, at large separation, the capillary bridges can become unstable by (g) breaking the droplet or (h) transferring to one of the substrates.

forced to "submerge" into the lubricant. We have also shown two broad classification of capillary bridges Fig. 3.2, hydrophilic and hydrophobic capillary bridges in the top and bottom rows, respectively, with the exception Fig. 3.2 (a) and (b). This is precisely defined to be when the apparent angles are $\theta_{app} < 90°$ and $\theta_{app} > 90°$, respectively. In Fig. 3.2 (a) and (b) we show unstable morphologies. Both morphologies can occur for hydrophobic capillary bridges, and can also occur for hydrophilic capillary bridges. Strictly speaking, the minimization routine fully converges only for morphologies labelled as stable. The unstable morphologies are depicted to illustrate the capillary bridges as the instabilities take place. Due to the large number of control parameters, we have computed morphology diagrams in the form of 2D slices of the parameter space, as depicted in Fig. 3.3. For each slice, all the remaining parameters are fixed.

To start, let us vary the apparent angle θ_{app} and plate separation H/s in Fig. 3.3(a). We have normalised the length scale of the system by $s = (3V/4\pi)^{\frac{1}{3}}$, which

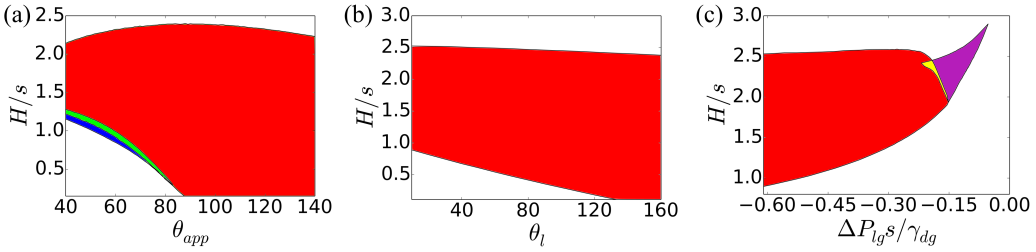

Figure 3.3: Morphology phase diagrams for a capillary bridge between two LIS. In panel (a), we vary the apparent contact angle θ_{app} and normalised separation H/s, and fix the lubricant Neumann angle $\theta_l = 160°$ and normalised lubricant pressure $\Delta P_{lg}s/\gamma_{dg} = -0.62$. In panel (b), we vary H/s and θ_l, keeping $\theta_{app} = 100°$ and $\Delta P_{lg}s/\gamma_{dg} = -0.62$. In panel (c), H/s and $\Delta P_{lg}s/\gamma_{dg}$ are varied, with $\theta_{app} = 100°$ and $\theta_l = 10°$. In all panels, the wetting contact angles for the lubricant are set at $\theta_{ld}^{\text{eff}} = \theta_{lg}^{\text{eff}} = 5°$. The red region denotes stable morphologies when the droplet remains attached to both LIS substrates, blue when the droplet is detached from both substrates, and purple when the droplet is detached from one of the substrates. The green and yellow regions in panels (a) and (c) represent regions where multiple morphologies are possible. These occur due to the presence of two energy minima, and would physically represent scenarios where the droplet may be pinned or not pinned onto the solid substrate.

is the radius of a sphere equal in volume to the droplet [54, 55, 38]. Here we have fixed the wetting contact angles for the lubricant, $\theta_{ld}^{\text{eff}} = \theta_{lg}^{\text{eff}} = 5°$, the lubricant Neumann angle, $\theta_l = 160°$, and the normalised lubricant pressure, $\Delta P_{lg}s/\gamma_{dg} = -0.62$. Such lubricant pressure results in lubricant ridge that is small compared to the droplet size for the majority of the results shown in Fig. 3.3(a), as commonly observed in experiments [77, 175, 176]. However, the lubricant ridge can become comparable in size with the droplet at small separations.

The largest, red colored region in Fig. 3.3(a) identifies the most common case of a stable liquid bridge in contact with both LIS substrates, as illustrated in Fig. 3.2(d-e). Moving to the bottom-left of the phase diagram by decreasing both the apparent angle and the plate separation, there also exists a morphology in which the droplet is detached from both substrates for hydrophilic capillary bridges ($\theta_{app} < 90°$), and where lubricant menisci connect the droplet and the substrates. Here, as we reduce the plate separation, we find the Neumann triangle at the top of the lubricant ridge rotates such that the drop-gas interface becomes

more aligned to the direction normal to the substrate. This in turn leads to a detachment of the lubricant-drop interface from the substrate. Such morphology is shown in Fig. 3.2(c) and corresponds to the blue region on the phase diagram in Fig. 3.3(a). The green region highlights the parameter space in which both morphologies are possible. Both states can coexist because the ld contact line can be pinned or unpinned to the LIS corrugations. This can be due to differing initial conditions such as a droplet resting on the LIS corrugations, and thus pinned, before a capillary bridge is formed. Or it could be possible that with enough agitation the droplet may become unpinned while the separation distance, H, is varied. Once unpinned the droplet needs to be forced to make contact with the LIS corrugations to become pinned again which due to hysteresis effects may not be at the same separation distance.

Further decreasing the plate separation leads to an instability related to the coalescence of the two lubricant menisci. The lubricant floods the space in between the LIS substrates and envelopes the droplet. In our studies, since we use the pressure ensemble for the lubricant, this continues indefinitely. However, in practice, especially in the limit of starved lubricant regime, it will do so until the lubricant from the drop surrounding is depleted. This envelopment instability is unique to LIS where the capillary bridge has two liquid components. Inspecting the data reported in Fig. 3.3(a), we further observe that the envelopment instability occurs at larger separation as we decrease the apparent angle. Typically, the envelopment occurs with the droplet detached from the surfaces for hydrophilic bridges ($\theta_{app} < 90°$), as illustrated in Fig. 3.2(a); and with the droplet attached to the surfaces for hydrophobic bridges ($\theta_{app} > 90°$), illustrated in Fig. 3.2(b).

The capillary bridges also become unstable at large plate separation. Similar to conventional one-component capillary bridges on non-infused surfaces, this can occur in two ways. The drop can break in two as in Fig. 3.2(g), typically observed for hydrophilic capillary bridges. Alternatively, the droplet may detach from one of the substrates, as illustrated in Fig. 3.2(h), commonly found for hydrophobic

bridges. Since we ignore gravity in the studies shown, the droplet can move to the top or bottom substrate with equal probability triggered by numerical noise during minimization. The detailed dynamics of these instabilities are beyond the scope of the work we show here.

Next, we study the role of the lubricant Neumann angle θ_l, in particular to characterize the envelopment instability at small H/s. Fig. 3.3(b) shows a phase diagram as a function of H/s and θ_l. We now fix $\theta_{app} = 100°$, while the other parameters are set as before in Fig. 3.3 (a). It is worth noting that the other two Neumann angles are no longer independent variables when an apparent angle and one of the Neumann angles are defined. Here we employ the lubricant Neumann angle as control parameter, as it provides a good measure of the shape of the lubricant ridge.

We clearly observe that the system is more prone to envelopment instability for smaller θ_l. Considering the force balance at the droplet-lubricant-gas contact line, this is because smaller θ_l implies the droplet-gas surface tension becomes more dominant in magnitude over the droplet-lubricant and lubricant-gas surface tensions. As such, the system can lower its free energy by reducing any droplet-gas interface. In contrast, the detachment instability at large H/s is relatively insensitive to θ_l.

In Fig. 3.3(a) we observe that the stability region for bridge morphologies where the drop is detached from both substrates, as depicted in Fig. 3.2(c), is limited to $\theta_{app} < 90°$. We now investigate whether this morphology can occur also for $\theta_{app} > 90°$ for a different combination of parameters. We find the critical parameter is the lubricant pressure ΔP_{lg}. Thus, we present a morphology phase diagram as a function of separation H/s and $\Delta P_{lg} s/\gamma_{dg}$ in Fig. 3.3(c). Here we fix $\theta_{ld}^{\text{eff}} = \theta_{lg}^{\text{eff}} = 5°$, $\theta_{app} = 100°$, and $\theta_l = 10°$. Interestingly, the morphology where the droplet is detached from both substrates is not found to be stable for hydrophobic bridges. Rather, we find a morphology where the droplet is only directly in contact with one of the substrates, as illustrated in Fig. 3.2(f), when

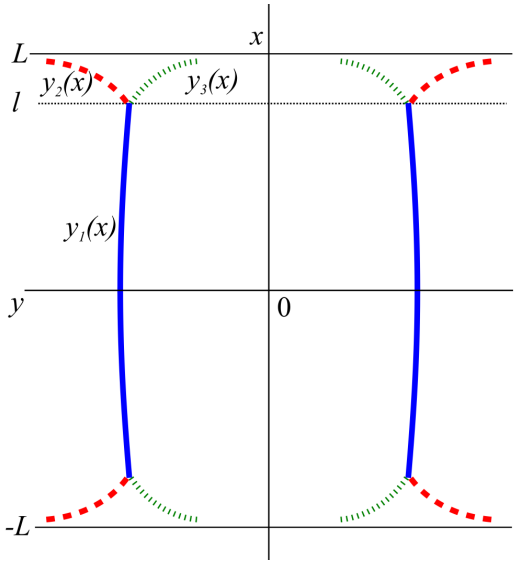

Figure 3.4: Schematic of the capillary bridge profile. Here, $y_1(x)$ (solid line) is the drop-gas interface, $y_2(x)$ (dashed line) is the lubricant-gas interface, and $y_3(x)$ (dotted line) is the lubricant-drop interface.

we increase $\Delta P_{lg}s/\gamma_{dg}$ (becoming less negative). Physically, increasing $\Delta P_{lg}s/\gamma_{dg}$ corresponds to reducing the energy costs of drawing lubricant from the reservoir, leading to lubricant meniscus size which is comparable to the droplet size. In the phase diagram of Fig. 3.3(c), this morphology is indicated by the purple region, bounded from below by the envelopment instability and from above by the droplet detachment instability. The two instability boundaries terminate in a cusp located at $\Delta P_{lg}s/\gamma_{dg} = -0.053$ and $H/s = 2.896$. It is also worth commenting that the morphology in Fig. 3.2(f) is observed for a wide range of θ_l. Here we have fixed $\theta_l = 10°$ because lower θ_l allows a broader range of plate separation in which the morphology is stable. The yellow region corresponds to parameter regime where the morphologies of Fig. 3.2(d) and (f) are both possible.

3.2.2 Capillary Forces

3.2.2.1 Calculating the Forces and the Spring Constant

A natural measure of the "stickiness" of capillary bridges between LIS surfaces is given by the capillary force exerted by the bridges on the two substrates. This force can be directly calculated from the profile of a liquid bridge in mechanical equilibrium, as illustrated in Fig. 3.4.

The capillary force exerted by the liquid bridge can be directly calculated from the equilibrium profile. To derive the force, consider variation of the free energy of the system induced by varying the plate separation, $H \to H + \delta H$, following a similar approach carried out for one-component liquid bridges [138, 37, 137]. Since we are considering symmetric surfaces, it is mathematically more convenient to set the origin of our coordinate system to be at the middle of the liquid bridge. If we define the $y_i(x)$ to represent each interface's radial distance from the axial centre of the bridge, then the surfaces are located at $\pm H/2$, as defined in Fig 3.4. As such, exploiting symmetry, we only need to consider the profile curves from $x = 0$ to $x = L = H/2$. Under this variation, the position of the drop-lubricant-gas triple contact line varies from $l \to l + \delta l$, and correspondingly the profile curves also vary as $y_i(x) \to \bar{y}_i(x) = y_i(x) + g_i(x)$.

The free energy upon extending the plate separation by $\delta H = 2\delta L$ is given by

$$\begin{aligned}
&\frac{E_{\mathrm{LIS}}(L+\delta L)}{2\pi} \\
&= \int_0^{l+\delta l} \gamma_{dg}\bar{y}_1(x)(1+(\bar{y}_1')^2(x))^{1/2} - \frac{\Delta P_{dg}}{2}\bar{y}_1^2(x)\ \mathrm{d}x \\
&+ \int_{l+\delta l}^{L+\delta L} \gamma_{lg}\bar{y}_2(x)(1+(\bar{y}_2')^2(x))^{1/2} - \frac{\Delta P_{lg}}{2}\bar{y}_2^2(x)\ \mathrm{d}x \\
&+ \int_{l+\delta l}^{L+\delta L} \gamma_{ld}\bar{y}_3(x)(1+(\bar{y}_3')^2(x))^{1/2} - \frac{\Delta P_{dl}}{2}\bar{y}_3^2(x)\ \mathrm{d}x \\
&+ \gamma_{ld}\cos\theta_{ld}^{\mathrm{eff}}\bar{y}_3^2(L+\delta L) - \gamma_{lg}\cos\theta_{lg}^{\mathrm{eff}}\bar{y}_2^2(L+\delta L). \qquad (3.1)
\end{aligned}$$

The first variation of the free energy leads to the well-known Euler-Lagrange or shape equation for each of the fluid interface, $y_i(x)$, as derived in [138, 37, 137].

In addition, it leads to boundary conditions at $x = l$ and $x = L$. For the former, considering the variation in δl gives us

$$\left[\frac{\gamma_{dg}}{(1+(y_1')^2)^{1/2}} - \frac{\gamma_{lg}}{(1+(y_2')^2)^{1/2}} - \frac{\gamma_{ld}}{(1+(y_3')^2)^{1/2}}\right] y(l) - \left[\frac{\Delta P_{dg}}{2} - \frac{\Delta P_{lg}}{2} - \frac{\Delta P_{dl}}{2}\right] y(l)^2 = 0. \tag{3.2}$$

where we have used $y(l) = y_i(l)$. The second term in the above equation is identically zero, since the pressure terms cancel one another. Furthermore, the square bracket in the first term corresponds to the force balance of the surface tensions projected in the x-direction. Similarly, the variation in $\delta y(l)$ results in

$$\left[\frac{\gamma_{dg} y_1'}{(1+(y_1')^2)^{1/2}} - \frac{\gamma_{lg} y_2'}{(1+(y_2')^2)^{1/2}} - \frac{\gamma_{ld} y_3'}{(1+(y_3')^2)^{1/2}}\right] = 0, \tag{3.3}$$

which is the force balance of the surface tensions projected in the y-direction. Note that for these derivations we have used the geometrical relation $g_i(l+\delta l) = \delta y_i(l) - y_i'(l)\delta l$.

We can do a similar analysis for the boundary condition at $x = L$. Considering the variation in $\delta y_2(L)$ and $\delta y_3(L)$, we recover the expected contact angle equations for the lubricant-gas and lubricant droplet interfaces,

$$\left[\gamma_{lg}\frac{y_2 y_2'}{(1+{y_2'}^2)^{\frac{1}{2}}}\right]_{x=L} - \gamma_{lg}\cos\theta_{lg}^{\text{eff}} y_2(L) = 0, \tag{3.4}$$

$$\left[\gamma_{ld}\frac{y_3 y_3'}{(1+{y_3'}^2)^{\frac{1}{2}}}\right]_{x=L} + \gamma_{ld}\cos\theta_{ld}^{\text{eff}} y_3(L) = 0. \tag{3.5}$$

Finally, to determine the actual force we must choose a point along x to evaluate. There are two natural locations to evaluate the capillary force, at the substrate or in the middle of the bridge. At the substrate, the capillary force is given by

$$\begin{aligned} F &= \frac{\delta(2E)}{\delta(2L)}\bigg|_{x=L} \\ &= 2\pi\left[\gamma_{lg}\frac{y_2}{(1+{y_2'}^2)^{\frac{1}{2}}} + \gamma_{ld}\frac{y_3}{(1+{y_3'}^2)^{\frac{1}{2}}}\right]_{x=L} \\ &\quad - \pi\left[\Delta P_{dg} y_3^2 + \Delta P_{lg}(y_2^2 - y_3^2)\right]_{x=L} \end{aligned} \tag{3.6}$$

The first term can be interpreted as the surface tension forces of both the lubricant-gas and lubricant-droplet interfaces acting perpendicular to the substrate, while the second term corresponds to force contributions due to the droplet and lubricant pressures relative to the surrounding gas pressure. This is the more generally useful way to determine the force.

Alternatively, the capillary force can be conveniently computed at the symmetry plane located at $x = 0$ in the schematic diagram in Fig. 3.4, in which $y_1' = 0$. In this case, the force expression simplifies to

$$\begin{aligned} F &= 2\pi \left[\gamma_{dg} \frac{y_1}{(1 + {y_1'}^2)^{\frac{1}{2}}} \right]_{x=0} - \pi \, \Delta P_{dg} y_1^2 \Big|_{x=0}, \\ &= 2\pi \gamma_{dg} r_d - \pi \Delta P_{dg} r_d^2. \end{aligned} \tag{3.7}$$

Here r_d is the radial distance of the droplet-gas interface. This term is simpler and easier to calculate fo the symmetric case, but would no longer confer any advantages if one was to pursue the studies for asymmetric capillary bridges. In Fig. 3.5 we show these comparisons. We use the derivative of the energy calculated using a simple finite difference method for one force calculation, F_E. This is then compared with force calculated directly from the capillary bridge profile at various points along the capillary bridge: F_B, at the bottom; F_T at the top; F_M at the middle. As can be seen that for the methods of force calculation are equivalent, and holds true for hydrophilic-like and hydrophobic-like capillary bridges.

A complementary measure of the "stickiness" is given by the spring constant of the bridge, K_{eq}, when the capillary force vanishes. To calculate K_{eq}, we can employ a simple linear relation between the calculated force and the displacement from the capillary bridge equilibrium distance. Following Hooke's Law,

$$F = -K_{eq}(H - H_{eq}),$$

where H_{eq} is the capillary bridge separation when $F = 0$. By fitting how F varies with H near the equilibrium distance, K_{eq} can be obtained. An increasing spring constant would mean that any "snapping" forces experienced during ca-

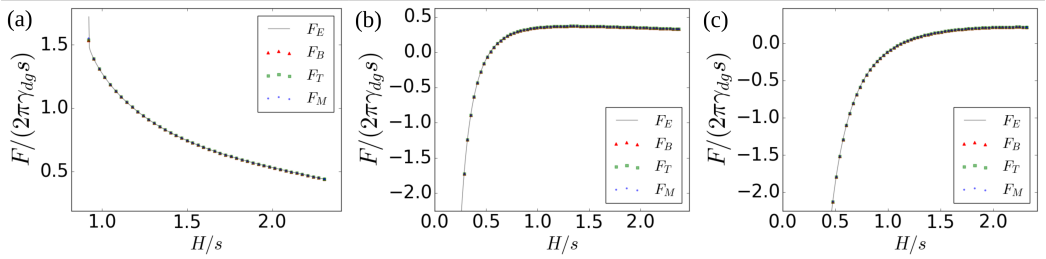

Figure 3.5: We plot the force calculated in four ways: F_E gives the force calculated by the derivative of the energy; F_B is the force calculated for the bottom surface contact; F_T the force calculated for the top surface contact; F_M the force calculated from the middle of the bridge. All panels show the results for $\theta_l = 160°$, $\Delta P_{lg} s/\gamma_{dg} = -0.62$, with surface contact angles $\theta_{lg} = \theta_{ld} = 5°$. They differ in the apparent angles used. Panel (a) shows the case of $\theta_{app} = 60°$; (b) shows the case of $\theta_{app} = 100°$; (c) shows the case of $\theta_{app} = 120°$. We have explored three cases to highlight the agreement for the various methods of force calculations for hydrophilic ($\theta_{app} < 90°$), and hydrophobic ($\theta_{app} > 90°$) capillary bridges. It can also be observed in (b) that the force reaches a maximum before detaching. This means that the droplet is detaching in a relatively controlled manner instead of "snapping off" once it reaches its maximum force. Experimentally one could thus measure the maximum force more accurately.

pillary bridge formation or stretching would be increased, which could have implications when measuring the surface tension of the droplet and stability of the capillary bridges.

3.2.2.2 Effects on the Capillary Forces and Spring Constants due to Material Variations

Having discussed the spectrum of different liquid bridge morphologies between two LIS substrates, we now address the key question of how the forces exerted by stable capillary bridges are affected by the presence of the lubricant. We will start by considering cases in which the lubricant ridge is small and flat, which we can achieve by setting large lubricant Neumann angle and low lubricant pressure. Here we use $\theta_l = 160°$, and $\Delta P_{lg} s/\gamma_{dg} = -0.62$. Fig. 3.6(a) and (b) show the (normalised) force contour plots as a function of the (apparent) contact angle and plate separation for a capillary bridge on smooth surfaces and LIS, respectively. For the latter, we focus on cases where the droplet is directly in contact with both LIS

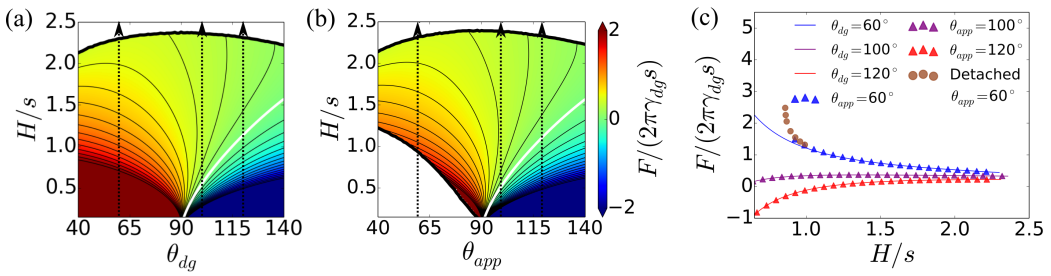

Figure 3.6: (a) and (b) Force contour plots as a function of contact angle (θ_{dg} or θ_{app}) and substrate separation for smooth solid surfaces and LIS, respectively. For the latter, we have set $\theta_l = 160°$, $\theta_{ld}^{\text{eff}} = \theta_{lg}^{\text{eff}} = 5°$ and $\Delta P_{lg}s/\gamma_{dg} = -0.62$. The white lines trace the separation for which the force is zero. (c) Capillary force as a function of the substrate separation for contact angles $\theta_{app} = 60°$, 100° and 120°. The LIS cases are represented by triangles and circles for when the droplet is attached and detached from the substrates, while those for smooth surfaces are represented by solid lines.

substrates. The parameter space explored here is the same as in the morphology diagram in Fig. 3.3(a).

In this limit in which the lubricant ridge is small and flat, the capillary forces obtained are quantitatively very similar for LIS and for smooth solid surfaces. For hydrophilic capillary bridges ($\theta_{app} < 90°$), the force is always attractive and monotonically decreases as one increases H/s; while for hydrophobic capillary bridges ($\theta_{app} > 90°$), the force is repulsive at short separation and attractive at large separation. Following Eqs. 3.6 and 3.7, this is because while the surface tension contributions are always attractive, the pressure contributions can be either attractive or repulsive. The contour of zero force, corresponding to the equilibrium separation distance, H_{eq}, is marked by the white lines in Fig. 3.6 (a) and (b). Consequently, it can be observed that there is no equilibrium separation for hydrophilic capillary bridges, implying that the LIS plates will prefer to stick together. Of course in reality due to the finite size of the droplet and the fact the separation distance can never truly reach zero, the force will never reach infinity. From these results, we can also conclude that the apparent contact angle is a suitable control parameter to compare capillary bridges on conventional smooth, non-infused surfaces and LIS in the limit of small lubricant ridges.

The main difference between one-component liquid bridges on non-infused surfaces and two-component liquid bridges on LIS, as shown in Fig. 3.6, is found at small H/s for $\theta_{app} < 90°$, as we approach the parameter space in which the detached droplet and enveloped morphologies in Figs. 3.2(a) and (c) are preferred. To better illustrate this point, Fig. 3.6(c) plots the capillary force F as a function of separation H for three contact angles, 60°, 100° and 120°. The LIS cases are shown with triangular and circular markers for when the droplet is attached and detached from the substrates, while those for one-component capillary bridge on smooth solid surfaces are shown with solid lines. As illustrated in Fig. 3.6(c), we see the force deviates strongly at small H/s for $\theta_{app} = 60°$. This is due to significant amount of lubricant being drawn from the reservoir, increasing the attractive force of the capillary bridge.

This deviation illustrates the importance of the lubricant ridge in the resulting capillary force. Since the shape and size of the ridge depends on the Neumann and lubricant contact angles, as well as the lubricant pressure, we further investigate how these parameters affect the strength of the capillary adhesion of the droplet on LIS. To study these effects we have chosen to employ an apparent angle of $\theta_{app} = 100°$ as an exemplary case. Such contact angle value is quite typical in experiments [77, 175], though of course the apparent contact angle can be varied depending on the materials involved.

The effect of altering the wetting contact angles for the lubricant θ_{lg}^{eff}, θ_{ld}^{eff} and the Neumann angle θ_l at fixed apparent angle is shown in Fig. 3.7. Fig. 3.7(a)-(c) show contour plots of the (normalised) force as function of θ_l and H/s for different lubricant contact angles. In all three plots we have chosen $\Delta P_{lg} s/\gamma_{dg} = -0.62$. For comparison, we also show the force contour plot for one-component capillary bridge with $\theta_{dg} = 100°$ in Fig. 3.7(d).

The case with completely wetting lubricant is shown in Fig. 3.7(a). In such a scenario, the contact angles are no longer relevant. Theoretically this leads to an extra degree of freedom, the thickness of the lubricant layer. To control this we

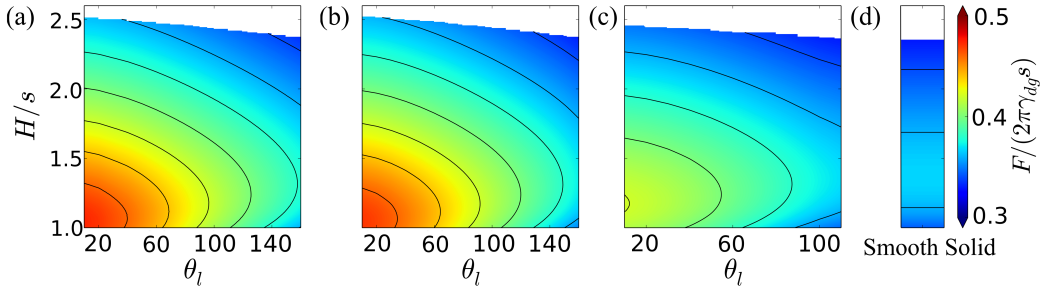

Figure 3.7: (a-c) Force contour plots as a function of the lubricant Neumann angle θ_l and normalised separation H/s. In panels (a-c), we have respectively set θ_{ld}^{eff}, $\theta_{lg}^{\text{eff}} = 0°$, 5°, and 30°. In all cases, we have $\theta_{app} = 100°$ and $\Delta P_{lg}s/\gamma_{dg} = -0.62$. For the complete wetting case, we have also chosen a Hamaker constant of $B/\gamma_{dg}s^2 = 2.6 \times 10^{-8}$. (d) Force contour plot as a function of H/s for a one-component capillary bridge with $\theta_{dg} = 100°$.

need to include the physics of disjoining pressure, and we have chosen a Hamaker constant of $B/\gamma_{dg}s^2 = 2.6 \times 10^{-8}$ to ensure the thickness of the lubricant layer is several orders of magnitude, $O(10^3)$, smaller than the droplet size $V_d^{1/3}$, as is typical in experiments [143, 142]. We have also studied cases with larger disjoining pressure (data not shown), and the only difference is that the lubricant layer thickness offsets the value of H/s when comparing the capillary forces. From the plot in Fig. 3.7(a), the maximum capillary force and separation distance increases with decreasing θ_l.

The same tendency in the variation of θ_l is observed in Fig. 3.7(b) and (c), where we now employ partially wetting lubricants with $\theta_{lg}^{\text{eff}} = \theta_{ld}^{\text{eff}} = 5°$ and 30°. We note that, for panel (c), there is no available solution for $\theta_l > 120°$ because the three angles forming the lubricant ridge must sum to less than 180°. Comparing the results in Fig. 3.7(a)-(d), it is also clear that the capillary adhesion is stronger on LIS than for one-component capillary bridge on smooth surfaces, and that this "stickiness" is amplified for more wetting lubricants. We find the capillary force on LIS can be up to 40% higher than that on smooth solid surfaces. Taking the results in Fig. 3.7 together, the shape of the lubricant ridge is an important factor to manipulate the strength of the capillary force.

Next, we address the issue of the size of the lubricant ridge, which can be tuned by varying the lubricant pressure. Fig. 3.8 (a) illustrates the case for a droplet

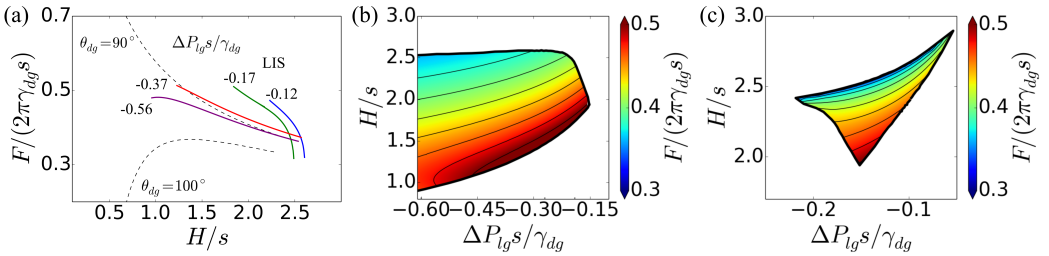

Figure 3.8: (a) Normalised capillary force as a function of normalised separation for several values of normalised lubricant pressure and an apparent angle of $\theta_{app} = 100°$. For comparison, the force curves for one-component capillary bridge is also shown for $\theta_{dg} = 90°, 100°$. (b-c) Force contour plots as a function of the normalised separation and normalised lubricant pressure when the droplet is connected to (b) both LIS substrates and (c) only one of the LIS substrates. Here we have used $\theta_l = 10°$, and $\theta_{ld}^{\text{eff}}, \theta_{lg}^{\text{eff}} = 5°$.

with $\theta_{app} = 100°$, $\theta_l = 10°$, $\theta_{ld}^{\text{eff}} = \theta_{lg}^{\text{eff}} = 5°$, while $\Delta P_{lg}s/\gamma_{dg}$ is varied. Here, the force curves only exist over a certain range of H/s, bounded by the envelopment instability from below and the detachment instability from above, as discussed in the previous section.

It is known that the apparent angle as defined in Eq. 2.6 is valid for the limit of vanishing ridge. As we make $\Delta P_{lg}s/\gamma_{dg}$ less negative, the lubricant ridge increases in size in comparison to the droplet size, and this can lead to a reduction in the measured geometric apparent angle [139, 140]. For hydrophobic cases, this angle will always be bounded from below by 90°. Therefore, to test whether the increase in the capillary force is simply due to changes in the effective apparent angle, we also plot force curves for one-component capillary bridges in Fig. 3.8(a) for contact angles $\theta_{dg} = 90°, 100°$, to allow for easy comparison. We find that we can even exceed the force from the 90° case for certain separation distances. This implies that the apparent angle alone is insufficient to fully describe the increase in capillary force.

Fig. 3.8(b) and (c) summarise the force contour plots as a function of $\Delta P_{lg}s/\gamma_{dg}$ and H for the stable morphologies where the droplet is directly attached to both LIS substrates and only one of the substrates respectively. In both scenarios, the capillary force increases with increasing $\Delta P_{lg}s/\gamma_{dg}$ at constant H/s, and decreases

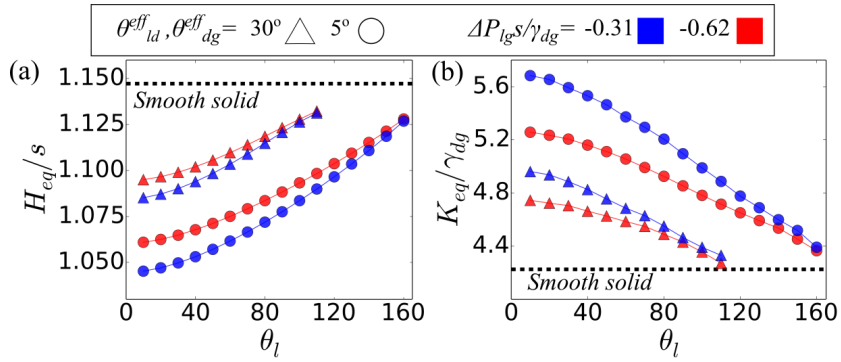

Figure 3.9: In both plots, the circles and triangles correspond to $\theta^{\text{eff}}_{ld}, \theta^{\text{eff}}_{lg} = 5°$ and 30°, respectively; while the straight and dashed lines represent $\Delta P_{lg}s/\gamma_{dg} = -0.31$ and -0.62. The apparent contact angle is set at $\theta_{app} = 120°$. (a) Equilibrium separation H_{eq} as a function of the lubricant Neumann angle. (b) Effective spring constant, K_{eq} as a function of the lubricant Neumann angle. The results for one-component capillary bridge on smooth surfaces are shown by the dotted lines.

with H/s at constant $\Delta P_{lg}s/\gamma_{dg}$. However, comparing the two contour plots, the capillary force is affected differently. This is most clearly illustrated by the force curves in Fig. 3.8(a). The cases of $\Delta P_{lg}s/\gamma_{dg} = -0.17$ and -0.12 have a different shape, with a greater dip in force near their maximum separation where droplet detachment occurs. This is because these cases correspond to morphology in Fig. 3.2(f), where the droplet is only directly connected to one of the LIS substrates. Here, the capillary force is dominated by the drawn lubricant. In contrast, the cases of $\Delta P_{lg}s/\gamma_{dg} = -0.56$ and -0.37 correspond to the morphology in Fig. 3.2(d), where the droplet dominates the capillary force response.

3.2.3 Equilibrium Separation and Spring Constant

To further corroborate our findings on the adhesion of a liquid droplet on LIS, in this subsection we will consider how the equilibrium separation, H_{eq}, and spring constant, K_{eq}, of the capillary bridge compare to those for one-component capillary bridge on non-infused, smooth solid surfaces.

We first note that, for one-component capillary bridge on non-infused surfaces, there is always an equilibrium separation in which the capillary force $F = 0$ for

$\theta_{dg} > 90°$. In contrast, this is not the case on LIS. In particular, the envelopment instability often kicks in before the capillary bridge can reach its equilibrium separation distance for small but negative value of $\Delta P_{lg} s/\gamma_{dg}$. For $\theta_{app} = 100°$, this instability significantly limits the range of parameters where the capillary bridge can reach $F = 0$. As such, in this subsection, we have chosen to focus on results with $\theta_{app} = 120°$. The qualitative behaviour is the same for different apparent angles.

Fig. 3.9 summarises our findings. In panel (a), we first study how the equilibrium separation is affected by the Neumann angle, θ_l, the wetting contact angles for the lubricant, θ_{lg}^{eff}, θ_{ld}^{eff}, and the lubricant pressure, $\Delta P_{lg} s/\gamma_{dg}$. For comparison, the one-component liquid bridge case is also shown as the black dotted line. Overall, we find the equilibrium separation is slightly smaller for LIS than for a one-component bridge. From the four curves for H_{eq}, we also observe that we approach the one-component liquid bridge case as we increase θ_l and make $\Delta P_{lg} s/\gamma_{dg}$ more negative. This is consistent with our observation in the previous subsection that the lubricant ridge morphology impacts the capillary force, so that as the ridge vanishes, LIS are equivalent to smooth surfaces in this limit.

We also study the effective spring constant, K_{eq}, around the equilibrium separation in Fig. 3.9(b). K_{eq} is always greater than that for the one-component liquid bridge implying that, not only capillary forces are larger on LIS, but also the resulting capillary bridges are stiffer due to the lubricant drawn from the LIS substrates. This would mean that capillary bridges can also be more stable around the equilibrium separation, as the "snapping" force which returns the capillary bridge to equilibrium is stronger.

3.3 Conclusion

In summary we have studied two-component capillary bridges formed when a liquid droplet is sandwiched between two LIS. The lubricant ridge morphology was

shown to be important in determining the capillary force, the maximum substrate separation, and the effective spring constant, which are all enhanced by lowering the lubricant-gas pressure difference ΔP_{og}, the lubricant Neumann angle θ_l, and the lubricant contact angles $\theta_{ld}^{\text{eff}}, \theta_{lg}^{\text{eff}}$ relative to the drop and gas phases. The parameter ΔP_{lg} affected the overall size of the lubricant ridge, θ_l changed the shape of the ridge, and $\theta_{ld}^{\text{eff}}, \theta_{lg}^{\text{eff}}$ tuned the adhesion between the lubricant and the solid surface. Varying these parameters we found that, for a given drop apparent contact angle, a capillary force could be achieved on LIS which was up to 40% higher than that for the one-component case. Conversely, in the limit of a vanishing lubricant ridge, the properties of the two-component capillary bridge tended to those of a one-component bridge between smooth, solid substrates.

In contrast to the one-component capillary bridge, a two-component capillary bridge also had a richer set of possible morphologies. Due to the presence of the lubricant, the capillary bridge could be stable with the liquid droplet directly in contact with two, one or none of the LIS substrates. At small separation, we have further identified a new envelopment instability, where the lubricant fills the space in between the two substrates.

While the facts that LIS have low contact angle hysteresis and are thus "slippery" parallel to the surface have been extensively discussed in the literature, here we point out that, at the same time, they are potentially "sticky" perpendicular to the surface. This suggests LIS are a unique class of liquid repellent surfaces. For instance, on superhydrophobic surfaces, liquid droplets are suspended on top of the surface textures in the Cassie-Baxter state, and as a result, they move easily both parallel and perpendicular to the surface [177, 178, 39]. In the Wenzel state, liquid drops penetrate the surface corrugations leading to both large contact angle hysteresis and strong adhesion [177, 178, 39], and so they are "sticky" in both directions.

Chapter 4

Ternary De-Wetting

4.1 Introduction

The importance of cleaning has long been recognised, likely since the beginning of sentient human history. Correspondingly, a significant amount of research has been done into developing a wide variety of cleaning processes and products [40, 179, 180]. This ranges from studying the fluid mechanics of confined and free surface flows typically involved in cleaning processes [181, 182], incorporating various ways of introducing additional mechanical perturbations [183, 184, 185, 186], improving the chemistry and chemical actions of the cleaning agents [180, 187, 188], and better understanding of how the undesirable soils can finally be removed from the substrate and captured elsewhere [189, 190].

Recent years, however, have seen a new challenge in the field of cleaning. Driven by environmental concerns and aspirations for more sustainable development, there is now an urge to develop cleaning mechanisms that employ significantly less resources, including the use of water and surfactants [191, 192, 193, 194, 195]. There is currently over 40% gap in global water supply and demand [196], and cleaning tasks consume a sizable proportion of household water ($\sim$ 16.5% for clothes washer usage alone according to a 2016 Report by the Water Research Foundation) [197]. There is also strong recognition to reduce surfactant consumption, both because

many surfactants are not environmentally friendly [198, 191] and because it requires significant energy and CO2 emissions to produce them [199].

Motivated by this challenge to clean under constrained resources, here we study the fluid dynamics of droplet lift-off driven by an invading film of another immiscible liquid, as illustrated in Fig. 4.1. This mechanism exploits the lifting force arising from the Neumann triangle at the contact line between the droplet, the invading film, and the surrounding air. Hence, this mechanism necessarily involves three fluid phases, unlike other, more well-studied de-wetting phenomena that typically involve two fluid phases [200, 201, 202]. Furthermore, in contrast to traditional cleaning processes that harness an abundant amount of water-based formulation, here we demonstrate that this ternary de-wetting mechanism can enable droplet lift-off and removal from the surface only when the film thickness is comparable to the droplet size.

We organise this chapter as follows. In Section 4.2, we discuss the simulation geometry and computational methods used in our work. In Section 4.3, we introduce previous results, by Jack Panter, and what we term the ternary lift-off mechanism in the quasi-static limit, and critically discuss the importance of the interfacial tensions between the various fluids involved. All sections labelled as "Previous Results" were primarily due to the work of Jack Panter. Then, in Section 4.4, we study the possible roles of dynamics in enhancing and/or limiting droplet removal, including the effects of the invading film velocity, as well as the densities and viscosities of the droplet and liquid film. Finally, we summarise the most salient points of our work in Section 4.5.

4.2 Model and Method

We use two numerical methods for the results presented in this chapter. The results are divided into two parts, the quasi-static results obtained by using an energy minimisation method, and the dynamic simulations by lattice Boltzmann

simulation. In both cases we use a diffuse interface model as described in Chapter 2: Methodology. Special credit must be given to Jack Panter who produced all the quasi-static results, and for full details on his energy minimisation method please see his thesis [147].

4.2.1 Simulation Geometry

The typical simulation geometry studied in this chapter is shown in Fig. 4.1. A soil droplet (shown in yellow), d, is placed on a solid surface with a contact angle of θ_{dg} in the presence of the surrounding gas, g (see Fig. 4.1a). For the rest of this chapter, unless otherwise stated, we use $\theta_{dg} = 60°$. We find the value of θ_{dg} is not critical and only affects the start of our dynamical simulations. The more critical variable is the droplet contact angle θ_{dl} in the presence of the formulation film (l, shown in blue), as illustrated in Fig. 4.1b, which we will vary broadly.

The three fluids have interfacial tensions between one another that we denote by γ_{dl}, γ_{dg} and γ_{lg}. The three fluid interfaces meet at the triple contact line, and using force balance argument, they form certain angles known as the Neumann angles, θ_l, θ_d, and θ_g. These angles satisfy the following relations [139],

$$\frac{\gamma_{dl}}{\sin\theta_g} = \frac{\gamma_{dg}}{\sin\theta_l} = \frac{\gamma_{lg}}{\sin\theta_d}. \tag{4.1}$$

4.2.2 Previous Results - Quasi-Static Simulations

We give a brief overview of how the energy minimisation is applied for this chapter. For the quasi-static simulations, we wish to achieve minimum energy configurations of a sessile soil droplet of fixed volume, partially immersed in a layer of the formulation film.

The free energy is defined by three contributions,

$$E = E_b + E_s + E_c, \tag{4.2}$$

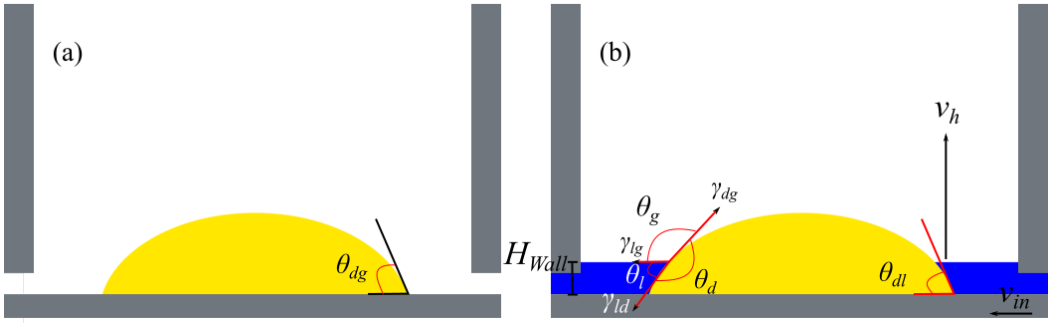

Figure 4.1: Schematic diagram of our simulation geometry. In yellow we have the soil droplet, in blue the formulation film, while the solid substrates are shown in grey. In panel (a) we show the soil droplet resting on the substrate with no formulation present. This is characterised by the droplet-gas contact angle, θ_{dg}. Panel (b) shows the case when we introduce the formulation film to the system, with the droplet forming a contact angle θ_{dl} in the presence of the formulation. At the triple contact line we highlight the various interfacial tensions, γ_{dl}, γ_{dg} and γ_{lg}, and Neumann angles, θ_l, θ_d, and θ_g. Finally we show the inlet velocity, v_{in}, through a liquid-filled aperture of height H_{wall} which leads to the formulation height velocity, v_h, moving upwards.

where E_b is the bulk free energy and E_s is the surface free energy. Both are defined in Chapter 2: Methodology, where we have used the Surface Energy method to define E_s. E_c is the constraining potential, which serves to ensure the volume of the droplet is fixed. This is given by

$$E_c = k_c \left(V_d - V_d^o\right), \tag{4.3}$$

where k_c is the constraint strength, V_d^o is the desired droplet volume, and V_d is the droplet volume at a given step in the free energy minimisation. Throughout, we fix $k_c = 1.0 \times 10^{-6}$ and $V_d^o = 6.0 \times 10^5$, both expressed in lattice units. The value for k_c was determined by trial and error to ensure numerical stability, while V_d^o is chosen as an input volume for the droplet which has been kept constant throughout.

To achieve equilibrium fluid configurations, the total free energy $E_b + E_s + E_c$ is minimised. To do this efficiently, we treat the system as axisymmetric about the centre of the droplet, and discretise the domain into a 2D square array of 200 $\times$ 150 nodes. The lattice spacing is $\varepsilon/4$. The minimisation is carried out using the L-BFGS algorithm [203, 204] due to its computational and memory efficiency.

To simulate the quasi-static introduction of the formulation film, the system is initialised in a configuration like that shown in Fig 4.1b, featuring a droplet in the centre of the system, with a formulation film of depth H_{wall}. At the inlet to the system, the film height is fixed at H_{wall}. The energy of this configuration is then minimised. In each subsequent iteration, we use the previously minimised configuration as input, increase H_{wall} at the boundary by 1 lattice unit, and re-minimise the energy.

In addition to the minimum energy configurations, we also find the energy barrier to detaching a droplet from the surface to form a liquid lens at fixed film height H_{wall}. To do this, the system must exhibit multistability - both a partially-submerged sessile drop and a detached lens are stable at the same H_{wall}. We then use the simplified string method [205], in which an interpolated chain of 40 images is initialised between the two metastable states, then evolved to converge on the minimum energy pathway. The highest energy point along this minimum energy pathway defines the transition state. The energy difference between the sessile droplet state and the transition state defines the minimum energy barrier to lifting the sessile droplet off the surface in this ternary system, labelled ΔE_T. As a comparison, we have also calculated the energy barrier to lift a droplet off the substrate when the droplet is completely submerged in liquid (no gas is present in the system). The energy barrier in this binary system is labelled as ΔE_B. This is calculated as the difference in energy between a sessile drop of contact angle θ_{dl}, and a fully detached drop, so that

$$\Delta E_B = 4\pi R_d^{o2} \gamma_{dl} \left(1 - \frac{R_d^o}{R_d}\right). \tag{4.4}$$

R_d^o is the radius of a spherical drop of volume V_d^o, and R_d is the radius of curvature of the sessile drop, defined as

$$R_d = R_d^o \left[\frac{4}{(1-\cos\theta_{dl})^2 (2+\cos\theta_{dl})}\right]^{\frac{1}{3}}. \tag{4.5}$$

4.2.3 Dynamic Simulations

For the dynamic simulations we use the same bulk free energy term. Here we use Dong's method for determining the contact angles. In this chapter, we use the lattice Boltzmann method to solve the fluid equations of motion. Typically, our simulation domain consists of a 3D domain of 50 x 50 x 240 nodes. We also use symmetric boundary conditions for two symmetry planes to reduce the amount of lattice nodes needed for the simulation, in effect reducing the number of lattice nodes by a factor of 4, as opposed to a full domain of 100 x 100 x 240. Inlet boundary conditions are also used to allow constant in-flow of the formulation liquid with velocity v_{in} (See Fig. 4.1 (b); this leads to a characteristic formulation height velocity, v_h), and a convective boundary condition at the outlet to allow fluids to leave the simulation, as described by Wang et al. [206].

We initialise a droplet equivalent in volume to a spherical droplet with radius of 20 lattice units when taking into account the symmetry. For all the dynamical results presented here in this chapter we have initialised the droplet as hemispherical cap with contact angle of 60°, with the centre at zero on the symmetry axis. The inlet height was chosen to be 5 lattice units, while the initial film height was chosen to be 10 lattice units.

4.3 Previous Results - Quasi-Static Limit

4.3.1 Previous Results - Ternary Lift-Off Mechanism

We begin by considering the quasi-static limit, where the formulation is introduced infinitely slowly, before including the effects of dynamics in the next section. In this limit, we simply use energy minimization methods as discussed in Section 4.2.2, and dynamic material parameters, such as viscosity, do not play any role. In this section, we will also focus on the case where the soil droplet is small enough (below the capillary length) such that the effects of gravity can be ignored. Later on for

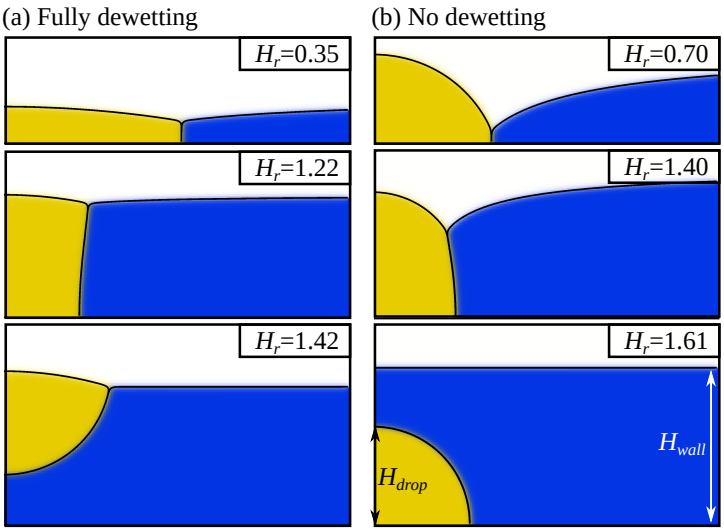

Figure 4.2: The two outcomes possible on quasi-statically increasing the liquid height H_r about a sessile droplet, where $H_r = H_{wall}/H_{drop}$. (a) Snapshots of the fully de-wettting transition for $\theta_{dl} = 90^o$, $\gamma_{dg}/\gamma_{lg} = 1.0$, $\gamma_{dl}/\gamma_{lg} = 0.1$. (b) Snapshots of the transition where no de-wetting occurs, for $\theta_{dl} = 90^o$, $\gamma_{dg}/\gamma_{lg} = 2.0$, $\gamma_{dl}/\gamma_{lg} = 2.5$. In all panels, the axis of rotation is on the left.

a subset of the dynamic results we will introduce gravity, but for the quasi-static limit none of the results have gravity implemented.

Upon increasing the liquid height at the boundary, H_{wall}, one of two transitions can occur, illustrated in Fig. 4.2. The first, shown in Fig. 4.2(a), sees the droplet stretched and raised by the three-fluid contact line, to completely de-wet from the underlying substrate. This results in a lens forming at the liquid-gas interface. The second, shown in Fig. 4.2b, sees the droplet also being stretched and raised by the three-fluid contact line, however instead of the droplet detaching from the surface, the liquid detaches from the droplet to result in a fully submerged sessile drop. We label the height of this submerged sessile drop H_{drop}.

In Fig. 4.3, we show phase diagrams demarcating the fully and no de-wetting states as functions of the droplet, formulation and gas interfacial tensions for five representative droplet-formulation contact angles. The regions marked with black-filled squares highlight fully de-wetting systems, whereas white-filled indicate where no de-wetting occurs. Note that blank regions indicate systems where one fluid is

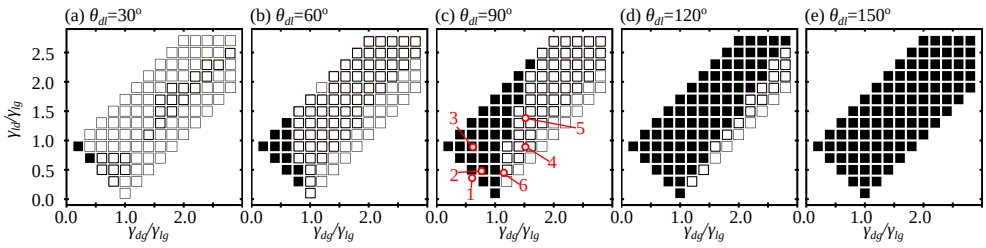

Figure 4.3: Phase diagrams of droplet de-wettability for varying interfacial tension ratios, γ_{ld}/γ_{lg} and γ_{dg}/γ_{lg}, at five different contact angles, θ_{dl}. We also indicate in panel (c) the 6 sets of interfacial tension ratios we choose to study further in Section 4.4. The squares in black show the regions where ternary lift-off occurs, while the white squares the regions where they do not. Outside the squares we have a region where the three-fluid interface is no longer stable.

completely spreading on the interface between the other two, meaning no three-fluid contact line is possible. As we are primarily concerned with the impact of the three-fluid contact line on de-wetting, we do not consider these states further.

Considering first only the regions marked with black squares (fully de-wetting systems), strikingly we see full de-wetting is able to be achieved for contact angles substantially less than 180°, the angle required for full dewetting in binary systems. We also observe several general trends. First, it is clear that as the droplet-formulation contact angle, θ_{dl}, increases the droplet is more likely to de-wet at various surface tensions ratios. This is to be expected, as it corresponds to the situation where the incoming formulation liquid increasingly has more favourable interfacial energy with the surface when compared to the droplet.

From Fig. 4.3, we also observe that the interfacial tensions strongly influence the de-wettability of the system. As can be seen in Fig. 4.3(a-c), decreasing γ_{dg}/γ_{lg} can lead to the transition from no de-wetting to full de-wetting. Meanwhile, most clearly seen in Fig. 4.3(c), at a fixed γ_{dg}/γ_{lg}, increasing γ_{ld}/γ_{lg} also leads to a transition from no de-wetting to full de-wetting. Both of these observations suggest that full de-wetting in ternary systems is promoted by large γ_{lg} and large γ_{ld}. In a sense, this contrasts with the simplified view of using more surfactant to reduce the formulation interfacial tension, γ_{lg}, to induce de-wetting for the binary case. Here, we highlight that although reducing the overall interfacial tensions is beneficial, it

is not strictly necessary to have formulation interfacial tension smaller than that of the droplet.

These trends can be understood from two complementary perspectives, based on either energetic or geometric arguments. Energetically, we consider the interfacial properties that energetically stabilise the liquid lens upon de-wetting, as opposed to the sessile droplet upon submersion. Full de-wetting may therefore be represented as a competition against submersion. Relative to the submerged droplet, the lens has: (1) a larger droplet-gas interfacial area, (2) a smaller liquid-gas interfacial area, (3) a smaller droplet-surface contact area. Respectively, the interfacial properties that stabilise the lens relative to the submerged state are then: (1) a smaller droplet-gas interfacial tension γ_{dg}, which principally stabilises the lens; (2) a larger liquid-gas interfacial tension γ_{lg}, which principally destabilises the submerged droplet; (3) a large droplet-liquid interfacial tension θ_{dl}, which also principally destabilises the submerged droplet.

4.3.1.1 Theoretical Understanding

Geometrically, we can understand fully versus no de-wetting using an analogy with capillary bridges. For a capillary bridge, both its shape and its stability limit are strongly determined by its contact angles [37, 207, 54]. In our analogy here, illustrated in Fig. 4.4a, the bottom contact angle is given by the droplet-formulation contact angle θ_{dl}. The effective top contact angle at the interface with the surrounding gas, which we denote by θ_t, is less obvious. However, if we assume the gas-droplet and gas-formulation interfaces to be relatively flat, we can approximate the top apparent contact angle by

$$\cos\theta_t \approx \frac{\gamma_{lg} - \gamma_{dg}}{\gamma_{ld}}. \tag{4.6}$$

We can now rationalise that by decreasing γ_{dg}, increasing γ_{lg}, or incrreasing γ_{ld}, the effective contact angle θ_t is lowered, and so the droplet tends to spread more at the gas interface. Indeed, as is well-understood in the capillary bridge literature

Formulation	γ_{dg}/γ_{lg}	γ_{ld}/γ_{lg}
1	0.6	0.5
2	0.7	0.6
3	0.6	1.0
4	1.5	1.0
5	1.5	1.5
6	1.1	0.6

Table 4.1: This table details the surface tension ratios chosen for formulae 1-6.

[208, 209, 210], for the droplet to be transferred from the bottom (here, the solid) to the top (here, effectively the gas interface) substrate, the bottom contact radius r_b must reach zero faster than the top contact radius r_t (See Fig. 4.4a). This is expected to take place if $\theta_t < \theta_{dl}$. In addition, depending on the effective contact angles at the top and bottom substrates, we can have convex and concave capillary bridge shapes, as shown in Fig. 4.4(b-c): the former when $\theta_t + \theta_{dl} > 180°$, and the latter when $\theta_t + \theta_{dl} < 180°$.

In Fig. 4.3(c), we have also indicated three cases (1, 2 and 3) of surface tension ratios with $\theta_t < 90°$, and three cases (4, 5 and 6) with $\theta_t > 90°$. We will further study these six surface tension ratios in Section 4.4. The precise ratios are given in Tab. 4.1. These six formula were chosen for a mixture of surface tension ratios, some are directly related to experimental measurements while others were chosen to give a good sampling of the ratios possible, with a good combination of $\gamma_{dg}/\gamma_{lg} \leq 1$ and $\gamma_{dg}/\gamma_{lg} \geq 1$, with $\gamma_{ld}/\gamma_{lg} \leq 1$ and $\gamma_{dg}/\gamma_{lg} \geq 1$.

4.3.2 Previous Results - Film Height for Inducing De-Wetting

The next question we address is the minimum amount of formulation that is required to enable the ternary lift-off mechanism, shown in Fig. 4.5. To do this, we focus on the fully de-wetted regions in the phase diagrams of Fig. 4.3 and plot the ratio of two characteristic heights in this problem, H_{wall}/H_{drop}, at the minimum H_{wall} required for full de-wetting. H_{drop} is the height of the sessile droplet when fully submerged by liquid. Examining, for example, Fig. 4.5d, we observe that

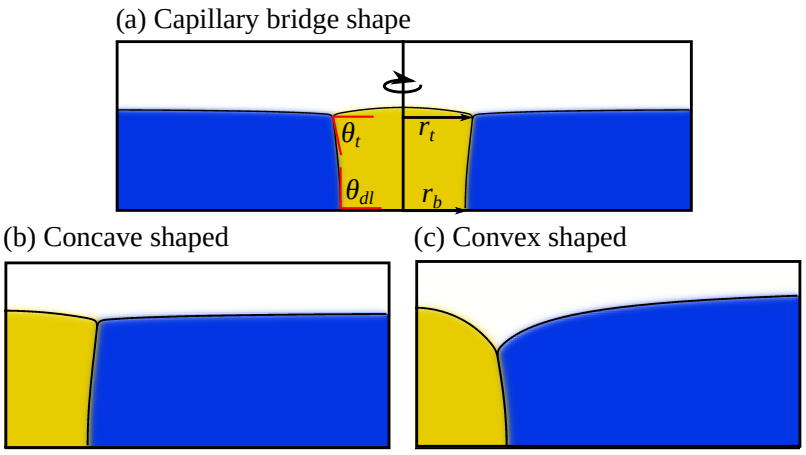

Figure 4.4: (a) An analogy with the capillary bridge geometry. We show the definitions of the contact radii, r_t and r_b, and contact angles, θ_t and θ_{dl}, at the top and bottom substrates. The axis of rotation is indicated in the centre of the system. (b) Example concave shape. (c) Example convex shape.

H_{wall} is minimised at small γ_{dg}/γ_{lg}, and large γ_{ld}/γ_{lg}. Under these conditions, a typical lens morphology will protrude substantially more into the gas region than into the liquid region beneath. Thus, a stable lens is able to be formed at small values of H_{wall}. Meanwhile, upon increasing the solid substrate wettability (decreasing θ_{dl}), H_{wall}/H_{drop} required for full de-wetting increases. This is because at small θ_{dl}, the droplet coats a relatively large solid surface area, and H_{drop} is relatively small. Thus, the liquid film must be made relatively thick in order to stretch the drop vertically enough to reduce the large drop-solid contact area to zero.

However, in all cases, H_{wall} is always comparable to H_{drop}. Thus, we can conclude that the amount of formulation required is much less than that required for a more traditional approach to cleaning where the liquid formulation would flood the system.

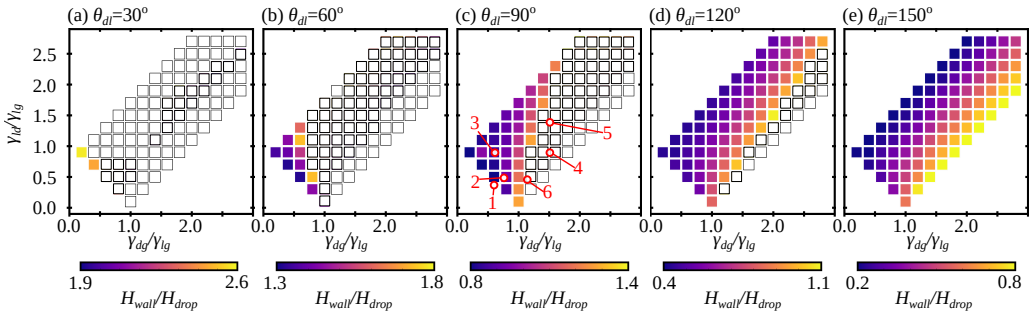

Figure 4.5: The ratio of H_{wall}/H_{drop} when fully de-wetting takes place as a function of the interfacial tension ratios, γ_{ld}/γ_{lg} and γ_{dg}/γ_{lg}, for five different contact angles, θ_{dl}. H_{wall}/H_{drop} provides an estimate for the amount of formulation required for the ternary lift-off mechanism.

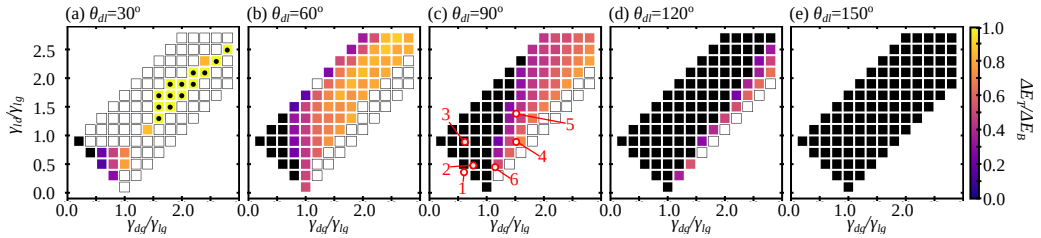

Figure 4.6: The energy barrier ratio, $\Delta E_T/\Delta E_B$, as a function of the interfacial tension ratios, γ_{ld}/γ_{lg} and γ_{dg}/γ_{lg}, for five different contact angles, θ_{dl}. In black are the regions which ternary lift-off fully de-wets the droplet, while the white regions are equivalent to regions where ternary lift-off will never be possible as the droplet is submerges without forming a triple contact line. For $\theta_{dl} = 30°$ we also show rare cases where $\Delta E_T/\Delta E_B > 1$, identified via black circles.

4.3.3 Previous Results - Reduction in Energy Barriers

We now return to the no de-wetting regions in the phase diagrams of Fig. 4.3. Even though the ternary lift-off mechanism is not sufficient to fully de-wet the system, it does not necessarily mean we cannot make use of the mechanism, at least partially. To explore this aspect, using the string method as described in Section 4.2.2, we compare the theoretical energy barrier for droplet lift-off when (i) the droplet is fully submerged by the formulation, ΔE_B; and (ii) the droplet is partially in contact with a formulation film, ΔE_T. For the calculation of ΔE_T, we vary the film height and choose the lowest possible energy barrier. We plot the ratio of $\Delta E_T/\Delta E_B$ on the phase diagrams for varying contact angles in Fig. 4.6. The black regions are

the regions which can fully de-wet by the ternary lift-off mechanism. The regions in white are regions where ternary lift-off is not possible because the equilibrium results suggests the droplet will remain submerged. More precisely, this is a result of a combination of two effects. In our quasi-static results we must still increase our fluid formulation amount in finite steps by increasing H_{wall} this can possibly lead to overshooting any increase causing the results to remain submerged. However, we believe these results are still accurate and relevant as there will always be a region of the phase space where any stretching is minimal, in which case it would be experimentally and numerically difficult to detect. These regions would thus show as lacking any detectable stretching numerically. In general, we observe, with exception of the case of $\theta_{dl} = 30°$, that $\Delta E_T/\Delta E_B < 1$. This suggests that we can still make use of the ternary lift-off mechanism to reduce the energy required to be inputted to de-wet the droplet, for example by introducing additional mechanical agitations, flows, or buoyancy effects.

4.4 Finite Velocities

Building on the quasi-static limit observations, we now wish to consider the effect of finite velocities on the droplet lift-off phenomenon. Since the simulation time involved is significantly more for the dynamic simulations, we are unable to explore the whole phase space. Instead, we choose to study in detail 6 surface tension ratios, as indicated in Fig. 4.3. We shall denote these as formulations (1)-(6).

Throughout, we will discuss how the interfacial and dynamic properties influence the three overarching dynamic dewetting mechanisms, illustrated in Fig. 4.7. In Fig. 4.7(a-d), snapshots of the dewetting transition show how the droplet is fully dewetted from the surface, to form a liquid lens. This mechanism is comparable to the quasi-static full de-wetting mechanism shown in Fig. 4.2a. In dynamic simulations, we also observe a partial dewetting mechanism, shown in Fig. 4.7(e-h), in which only a portion of the droplet is removed from the surface to form a

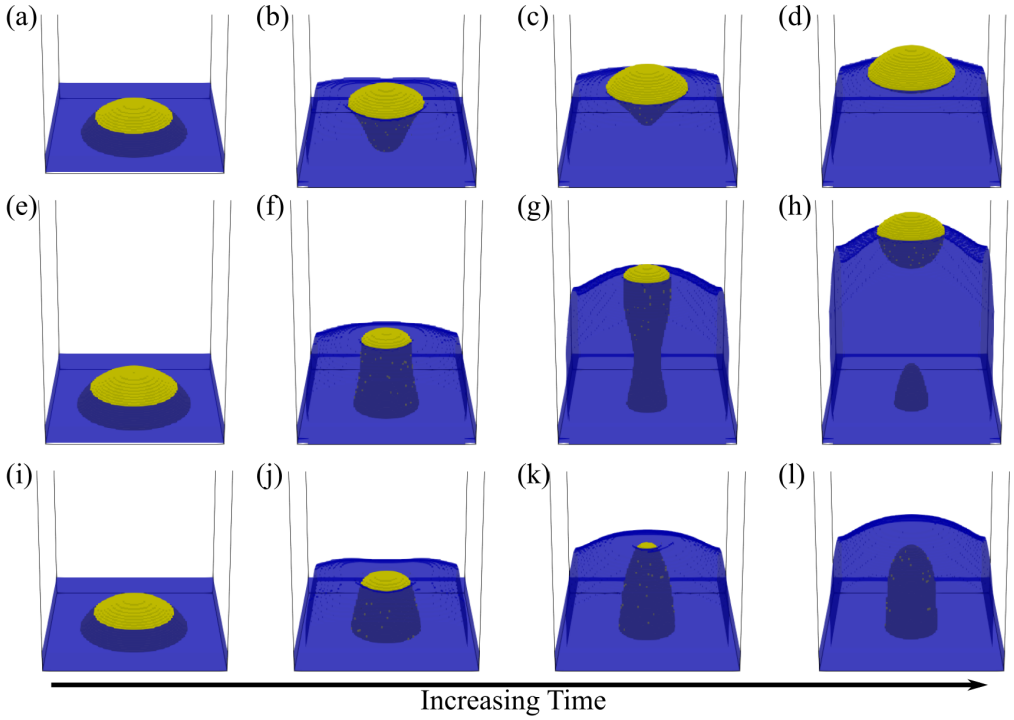

Figure 4.7: Typical dynamical evolution for the (a)-(d) fully de-wetting, (e) - (h) partially de-wetting, and (i) - (l) no de-wetting cases. In each case it can be seen we initialise a droplet resting on the surface in the same way, shown in the left column and as we move right we show snapshots increasing in time during the evolution of the system.

lens. The rest remains submerged as a sessile drop. Finally, Fig. 4.7(i-l) show the dynamic no de-wetting mechanism, whereby the liquid completely envelopes the drop, with no liquid detached from the surface. This mechanism is comparable to the quasi-static no de-wetting mechanism shown in Fig. 4.2 (b).

4.4.0.1 Varying Liquid Viscosities and Contact Angles

In this sub-section, we shall look at the effects of varying the droplet-formulation contact angle, θ_{dl}, as well as the viscosities of droplet, η_d, and formulation, η_l. The viscosity of the surrounding gas is negligible ($\eta_g \ll \eta_d, \eta_l$) and does not significantly affect our simulation results. For concreteness, here we choose a moderate input velocity such that the Capillary number is $\mathrm{Ca} = \eta_l v_h / \gamma_{lg} = 0.032$. We will explore varying the input velocities in Section 4.4.0.3. We will also compare cases where

gravity is absent and present. For the latter, we will focus on the scenario where the droplet and formulation have the same density. The Bond number is given by $\mathrm{Bo} = \rho g L^2/\gamma_{dg} = 28.8$.

Fig. 4.8 shows the outcomes of the simulation results for all 6 formulations, both in the absence and presence of gravity, as we vary the droplet-lubricant viscosity ratio and contact angle. We classify the results into three categories of de-wettability: no de-wetting, partial de-wetting and fully de-wetting cases. Additionally, we also highlight the boundary between no de-wetting and fully de-wetting states for formulations (4) to (6) in the quasi-static limit (see the dashed lines). For formulations (1) to (3), the boundary values are smaller than $\theta_{dl} = 90°$ and thus are not shown.

From Fig. 4.8, we can capture a number of general trends. First, comparing the cases with and without gravity, the downward action of gravity is to oppose the lift force arising from the force balance at the three-phase contact line, leading to poorer de-wettability as expected. Indeed, simulation results exploring buoyancy effects due to different droplet and formulation densities are provided later in Section 4.4.0.4. When the formulation has a larger density than the droplet, it provides an upward buoyancy force that assists the de-wetting of the droplet. In contrast, when the droplet has a larger density than the formulation, the droplet lift-off becomes even more less effective.

Second, comparing the results to the quasi-static limit, introducing a finite inlet velocity typically reduces the effectiveness of the ternary lift-off mechanism, as some fully de-wetting states in the quasi-static limit become partially or even no de-wetting states. This is because, with increasing velocity, there is a limited time for the capillary force to deform and lift the droplet. However, as we will see later, this is not always the case due to another competing mechanism.

Following the same argument as in the previous paragraph, we further expect that the increasing the droplet viscosity relative to the formulation viscosity will

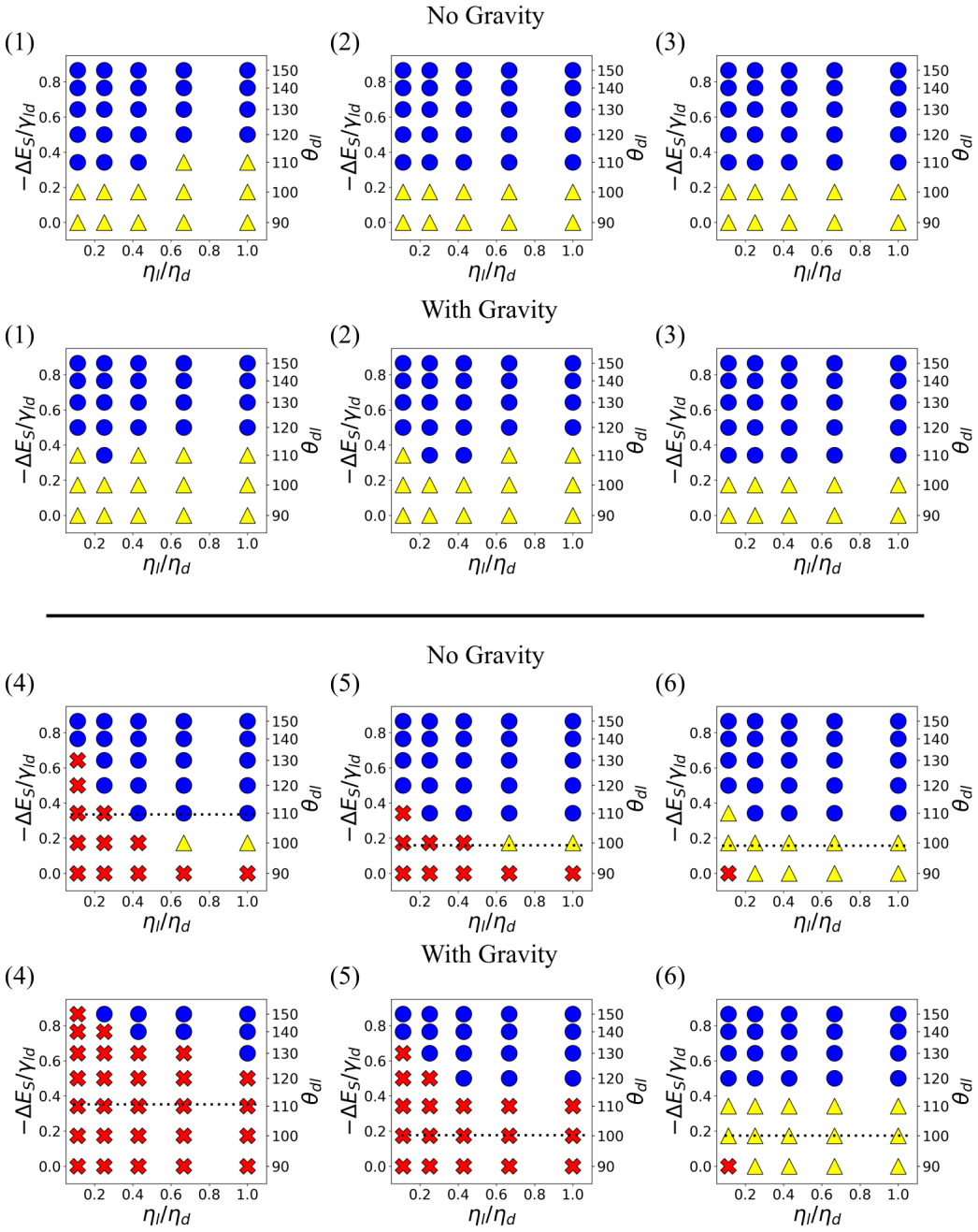

Figure 4.8: De-wetting states as a function of viscosity ratios and contact angles for formulations (1)-(6). All of the above systems utilize a characteristic capillary number of Ca = 0.032. For formulations (4)-(6), the dashed line shows the the boundary between full and no de-wetting in the quasi-static limit without gravity. The fully de-wetting states are marked by blue circles, partial de-wetting states by yellow triangles, and no de-wetting states by red crosses.

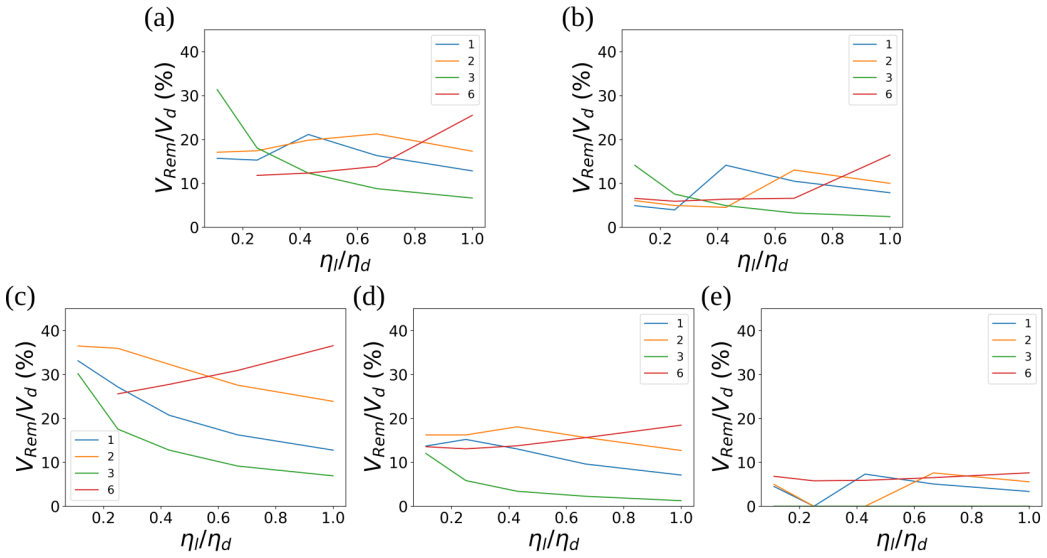

Figure 4.9: Droplet fraction remaining on the substrate as a function of droplet-formulation viscosity ratio for formulations 1, 2, 3, and 6 for the partially de-wetting states. Panels (a) and (b) show the zero gravity cases at contact angles $\theta_{dl} = 90°$ and 100°, respectively. Panels (c), (d), and (e) show the equal density cases at contact angles $\theta_{dl} = 90°$, 100° and 110°.

make it more difficult to deform the droplet, leading to poorer de-wettability for the system. We can clearly this behaviour for formulations (4)-(6) in Fig. 4.8, where fully de-wetting states turn into partial or no de-wetting states for smaller η_l/η_d. Interestingly, such dependency is less obvious for formulations (1)-(3), and we can even find the opposite trend, see e.g. Fig. 4.8 for formulation 1 along the line corresponding to $\theta_{dl} = 110°$.

The complex dependency of the ternary lift-off mechanism on the droplet-formulation viscosity ratio can be further seen when we plot the droplet fraction remained on the substrate for the partially de-wetting states, V_{Rem}. Fig. 4.9 (a-b) show the cases with zero gravity and $\theta_{dl} = 90°$, 100°, while Fig. 4.9 (c-e) show the equal density cases between the droplet and formulation with $\theta_{dl} = 90°$, 100°, 110°. Formulation (3) is the simplest to understand, as increasing the viscosity ratio decreases V_{Rem}, which follows our argument on the deformation of the droplet. However, for formulations (1) and (2), the droplet fraction broadly behaves non-monotonically with variations in η_l/η_d. The non-monotonic behaviour is because a

varying number of satellite droplets can form as the droplet is stretched. This leads to varying amounts of droplet remaining after each satellite droplet is detached, we have chosen to measure the results after the point at which no further satellite droplets form and detach. We found that with the addition of gravity fewer satellite droplets formed and detached, the overall trend when comparing Fig. 4.9 (a) with (c) and (b) with (d) shows that the percentage of droplet remaining increases when gravity is introduced. This is expected of course as gravity acts downward which means any effective uplifting force must be increased to compensate if the the droplet is to be removed. Perhaps the most surprising results are those of formulation (6) which has the opposite trend to formula (3). This suggests there is another mechanism at play at finite velocities that is competing with the ternary lift-off mechanism, one which is driven by the kinetic energy inputted into the system.

4.4.0.2 Momentum Aided Lift-Off

To better understand the non-monotonic behaviour observed in the previous section, we now investigate the de-wetting pathways that can be observed in our simulations. We find that, beyond the typical scenarios shown in Fig. 4.7, the momentum imparted by the invading formulation film can give rise to highly complex droplet lift-off dynamics.

We show exemplar cases of such momentum aided lift-off in Fig. 4.10. First, in panels (a) to (c), we see a fully de-wetting state where the complete droplet removal occurs in two stages. Initially, the droplet forms a neck which breaks the droplet in two as it is lifted. Then, the droplet fraction on the substrate rebounds of the substrate and fully lifts off due to the momentum imparted to the droplet. Second, panels (d) to (f) show a partially de-wetting state where the droplet becomes stretched and forms a long neck sustained by the droplet upward velocity, after which it breaks twice, once from the main droplet at the gas interface and a second time from the bottom substrate, leading to the formation of a satellite

droplet. Finally, in panels (g) to (i), we observe that the droplet is stretched by the incoming formulation but it is then detached from the gas interface. It is the momentum given to the droplet which breaks the droplet in two and results in a partially de-wetting state.

In fact, the mechanism in Fig. 4.10(d-f) with the formation of multiple detached droplets is commonly found for formulations (1) and (2) near the boundary between fully and partially de-wetting states and we identify this as a key reason why we can observe an upward trend on the amount of droplet remaining as function of increasing viscosity ratio η_l/η_d in Fig. 4.9.

4.4.0.3 Varying Input Velocity

To better understand the interplay between the ternary droplet lift-off and the momentum aided lift-off mechanisms, in this sub-section we vary the input velocity of the formulation film. For each formulation, we carry out two sets of velocities and the results are shown in Fig. 4.11. In the top section we use slower velocity, corresponding to Ca = 0.0032, or 10 times slower than our previous results. The bottom section shows the results for Ca=0.064 or 2 times faster than our previous results.

As we reduce the input velocity, we are approaching the quasi-static limit where ternary lift-off mechanism is dominating. For formulations (1)-(3), where the droplet typically has a concave shape, we see that all cases studied are now fully de-wetting. This means, for these cases, the kinetic energy has a negative impact to the de-wettability of the system. For formulations (4)-(6), where the droplet has a convex shape, we find that there is no partially de-wetting states at all, and many partially de-wetting states in Fig. 4.8 are now no de-wetting states. This is most obviously observed for formulation 6. This confirms that, indeed, the kinetic energy inputted to the system provides another mechanism for de-wetting, at least to enable partial droplet removal.

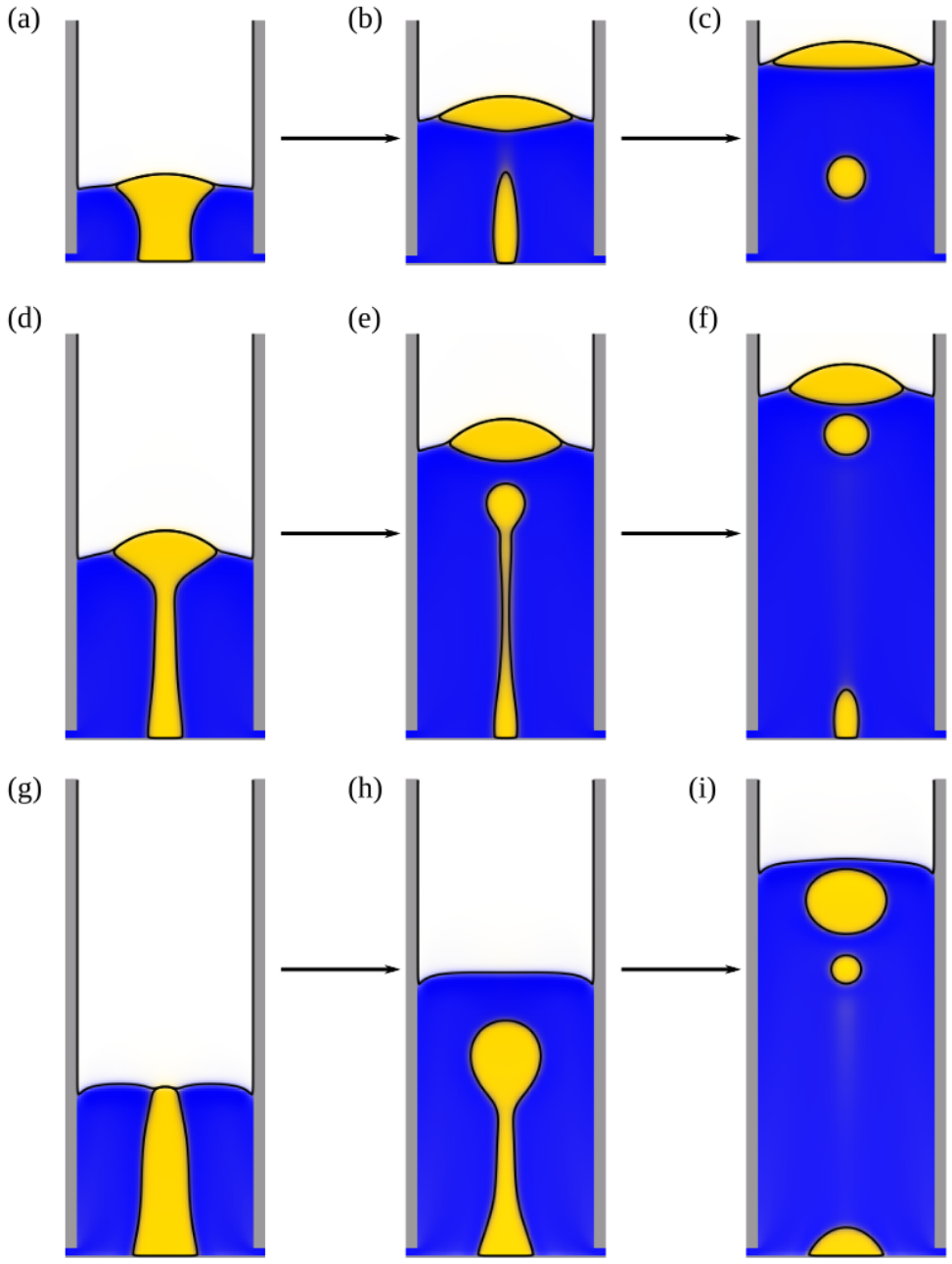

Figure 4.10: Examples on the relevance of momentum driven droplet lift-off. (a-c) A fully de-wetting state where the initial droplet remnant bounces off the surface. (d-f) A partially de-wetting state with a satellite droplet formed and lifted due to the fluid momentum. (g-i) A partially de-wetting state without any initial droplet fraction captured at the gas interface.

Our observation further suggests that some states which are no de-wetting in the quasi-static limit can be at least partially de-wetted by introducing more kinetic energy. This is confirmed in Fig. 4.11 when we double the inlet velocity. For concave shaped droplets, formulations (1)-(3), de-wettability becomes worse for increasing velocity as more resultant states turn from full to partially de-wetted states. However, interestingly, most of the no de-wetting states become partially de-wetting for the convex droplets, for formulations (4)-(6).

Velocity can thus be seen as an aid for de-wetting in some cases while a hindrance in others. From our current set of results, velocity can thus been seen as a leveller to some degree as the results for all formulae become much more similar, but there is still some dependency on the formulation, contact angles, and viscosity. Practically speaking, one could use this knowledge to aid in optimising a strategy for cleaning. In scenarios where the soil can be de-wetted by ternary lift-off then the formulation velocity should be minimised and vice-versa. In cases where there is a mixture of soils, cleaning could be divided into multi-stage processes. As a very qualitative example of cleaning in a washing machine, this would mean that an optimal strategy could be to introduce water very slowly to begin with, then rinsing and re-introducing water at a faster rate. However, the precise physics here would of course be very different due to difficulties in introducing a thin layer of formulation, so very extensive further studies will need to be made to concretely draw this conclusion.

4.4.0.4 Varying Density Ratios

Here we consider varying the density ratio between the droplet and the film. We choose density ratios of $\rho_d/\rho_l = 0.8$ and 1.5 to identify any general trends.

For the lower density ratio, as shown in Fig. 4.12, the droplet de-wettability is enhanced. In fact, we notice the phase diagram are ostensibly very similar and we no longer observed no de-wetting states. This is due to the buoyancy force as

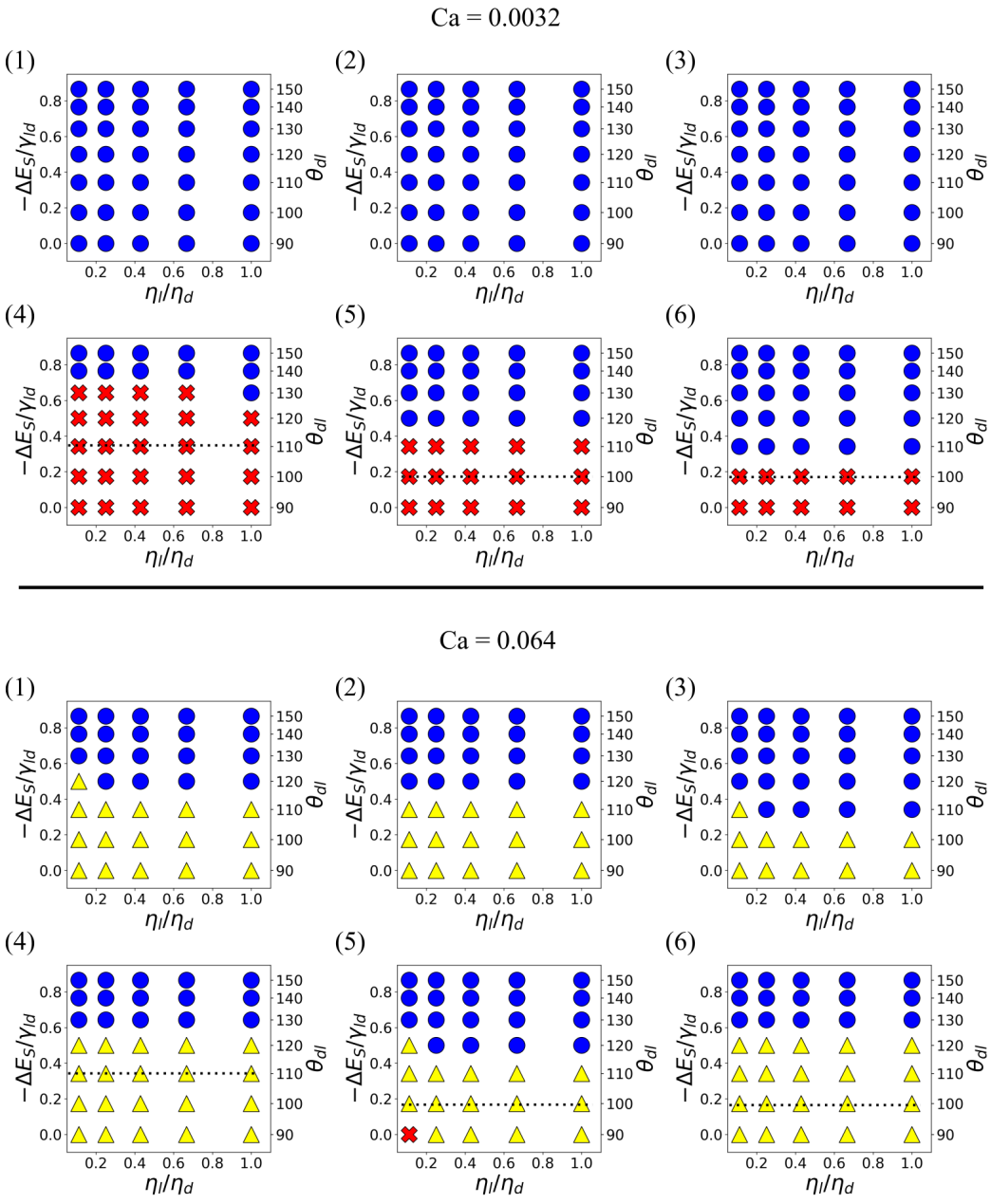

Figure 4.11: De-wetting states as a function of droplet-formulation viscosity ratio and contact angle for formulations 1-6. The top section utilizes a characteristic capillary number of Ca = 0.0032, while the bottom section Ca = 0.064. The densities of the soil droplet and liquid formulation are the same.

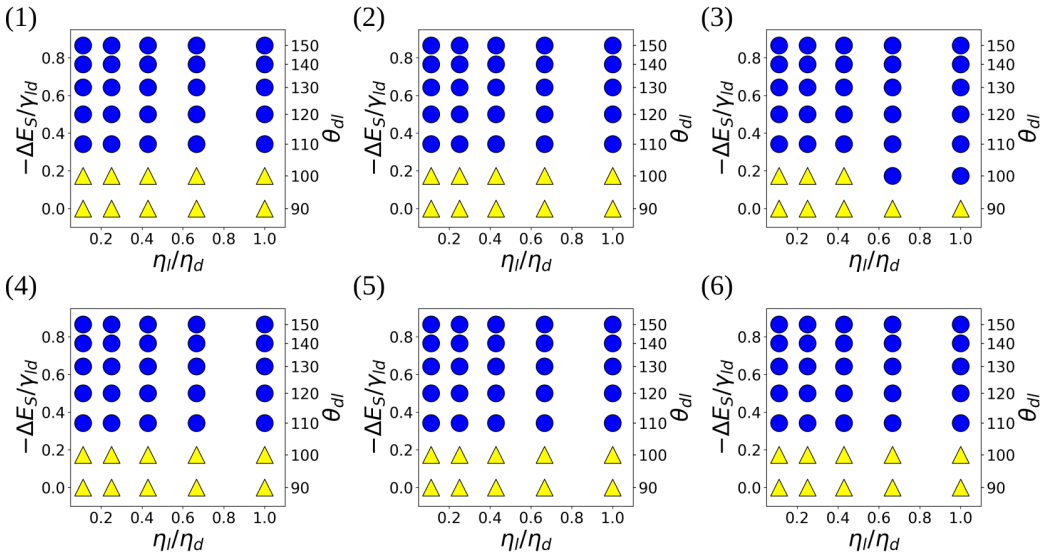

Figure 4.12: De-wetting states as a function of varying viscosity ratios and contact angles for formulations (1)-(6). All of the above systems utilize a characteristic capillary number of Ca = 0.0032, and the density ratio of droplet over formulation is 0.8.

the soil droplet has a lower density compared to the formulation. Due to buoyancy effects, any droplet residue also has a maximum size for the partially de-wetting states.

Perhaps more interesting are the results for the higher density ratio case, as shown in Fig. 4.13, where downward gravitational force inhibits droplet lift-off. We highlight how formulations (1), (2) and (3) are classified as partially de-wetting states, while formulations (4), (5) and (6) only have no de-wetting states. When we track the typical dynamical process for formulation (1)-(3), we observe only a very small amount of droplet is actually detaching, see Fig. 4.14. For formulations (4)-(6), no amount of detached droplet can be detected.

4.5 Conclusion

In this work we have studied a novel de-wetting phenomenon that exploits the upward capillary force resulting from the triple contact line between the droplet, film and surrounding gas phases. By introducing the film formulation in a controlled

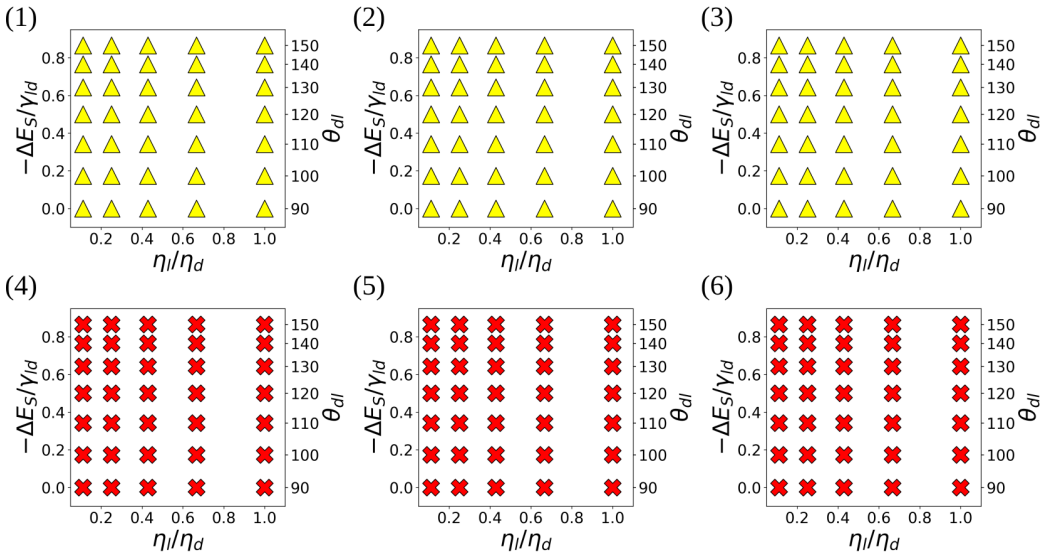

Figure 4.13: De-wetting states as a function of varying viscosity ratios and contact angles for formulations (1)-(6). All of the above systems utilize a characteristic capillary number of Ca = 0.0032, and the density ratio of droplet over formulation is 1.5.

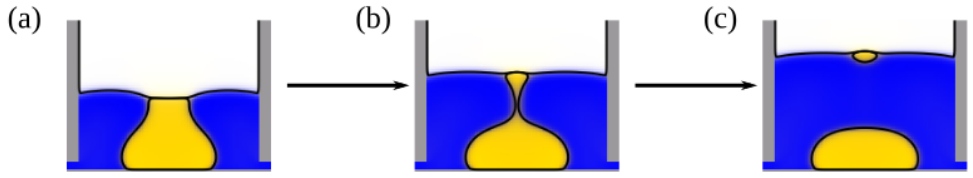

Figure 4.14: Typical dynamic evolution for the partially de-wetted state for a density ratio of $\rho_d/\rho_l = 1.5$.

manner, we demonstrated that we can achieve droplet removal from the substrate, i.e. cleaning, without the need to flood the system with the formulation liquid. In fact, the required film thickness is comparable to the size of the droplet. We believe this is a promising mechanism to consider for cleaning under constrained resources, where we would like to reduce the amount of water and surfactants used.

We further showed that the film velocity has a complex, non-monotonic influence on the efficacy of droplet lift-off. For small velocities, increasing the film in-flow generally makes the de-wetting process less effective because it reduces the time for which capillary forces deform and lift the droplet. For larger velocities, however, we find that the momentum imparted to the droplet can either helps (typ-

ically, for convex shaped droplets) or works against (typically, for concave shaped droplets) the de-wetting of the droplet.

The effectiveness of the lift-off mechanisms also depend strongly on the droplet wettability on the surface, θ_{dl}, and the surface tension ratios between the fluid phases involved. In particular, for the latter, we argued their relevance can be captured using the notion of an effective contact angle, θ_t, at the air interface. Droplet de-wettability is better the smaller θ_t is compared to θ_{dl}.

We hope this systematic simulation study will inspire experimental demonstrations of the ternary de-wetting mechanism. In this respect, it will be interesting to develop cleaning formulations that optimise for this droplet lift-off mechanism. Future work could also involve more detailed studies on the effect of density variations between the droplet and the formulation, and when the droplet and/or formulation are viscoelastic. Another possible direction for future work is to consider adding external mechanical perturbations to aid droplet removal.

Chapter 5

Ternary Phase Separation

5.1 Introduction

Spontaneous phase separation of fluid mixtures is important for a wide range of processes. For example, in nature, it is known to give rise to structural colours in living creatures, such as observed in birds and butterflies [211, 212]. More recently, it has also been shown to play fundamental roles in volcanic eruptions [213, 214] and in the organisation of cellular matters, leading to the formation of the so-called biomolecular condensates or membraneless organelles [215, 11, 216]. In industry, better understanding of the phase separation process is necessary, among others, for tuning the formation of fractures in alloys in the field of metallurgy [27, 28], for manipulating the structure of polymer blends which in turn affect their mechanical and electrical properties [64, 65, 66], and for controlling the morphology of complex emulsions for applications in drug delivery [19, 20] and in the food industry [21, 22, 23].

Extensive theoretical and experimental studies on phase separation have been carried out in the case where the fluid mixtures separate into two distinct, immiscible fluid components [217, 73, 218, 219]. For such binary fluid case, it is now generally well understood when spontaneous phase separation occurs, what the resulting morphologies are, and how the separated domains coarsen, both with

and without the influence of hydrodynamics [220, 218, 221]. However, the general problem of phase separation is significantly more complex, and there are numerous instances where the fluid mixtures separate into more than two immiscible components. These scenarios, in contrast, have received less attention and remain poorly understood.

Our focus in this work is on phase separation of three immiscible fluid components. In the literature, this ternary fluid case has primarily been studied in the context of thin films of polymer blends [222, 223, 224] where the evolution of their morphologies for a number of specific polymer compositions have been tabulated experimentally [68]. There is also growing interest in ternary fluid phase separation for other applications, such as a novel route for the production of complex droplet emulsions and nanoparticles [225, 95, 226]. In addition, from the modelling side, there have been efforts to simulate phase separation pathways that reproduce the experimental observations [68, 99], including scaling analysis on the domain coarsening [227, 228, 229]. Yet, despite these advances, there is still limited understanding in one of the most fundamental aspects of ternary fluid phase separation: how to predict and characterise the different possible distinct morphologies and phase separation pathways as function of the fluid composition. To provide insights, surprisingly, works to date have primarily relied on a simple linear stability analysis to demarcate the ternary phase diagram into regions with zero, one and two positive eigenvalues [68, 99, 93]. As we will demonstrate here, considering only the sign of the eigenvalues do not allow qualitative, let alone quantitative, predictions for the morphologies that can form.

Our contribution here is three-fold. First, we group the possible morphologies and separation pathways into 4 distinct families. Second, we rationalise these groupings by extending the prevailing linear stability analysis and harnessing information provided by the resulting eigenvalues and eigenvectors. Third, we study the ternary fluid phase separation mechanism where the minor fluid component is enriched and undergoes an instability at the interfaces between the two more

major components to determine the quantity of enrichment above which instability occur. We also found that this mechanism is the dominant mechanism across the composition phase space. We further show that the theoretical framework can be applied when the interfaces all have the same surface tension, as well as when they all take different values.

In contrast with the previous result chapters where solid interface effects had significant impact on the results, in this chapter we study phase separation to isolate any ternary fluid features resulting from fluid-fluid interactions only. From this we can conclude that bulk ternary fluid interactions also lead to genuine differences from the binary case without the need for solid interfaces.

In all situations studied in this work, we initialise each simulation by introducing small random concentration perturbations (white noise) on top of a homogeneous mixture at a given composition, typically with an amplitude of 10^{-4} of the fluid density. In this range, we verify the simulation results do not sensitively depend on the choice of noise amplitude. The simulation method used here is the lattice Boltzmann method, using the bulk free energy as described in Eq. 2.7 in Chapter 2.

5.2 Equal Surface Tension Case

We first focus on the simplest scenario where the surface tensions between any two pair of liquids are equal. We will consider the more general case in the next section.

5.2.1 Morphologies and Pathways

Let us start by considering the structures which can occur as the ternary fluid mixtures undergo phase separation. We find there are four distinct types of separation pathways, which typically lead to four morphology classes.

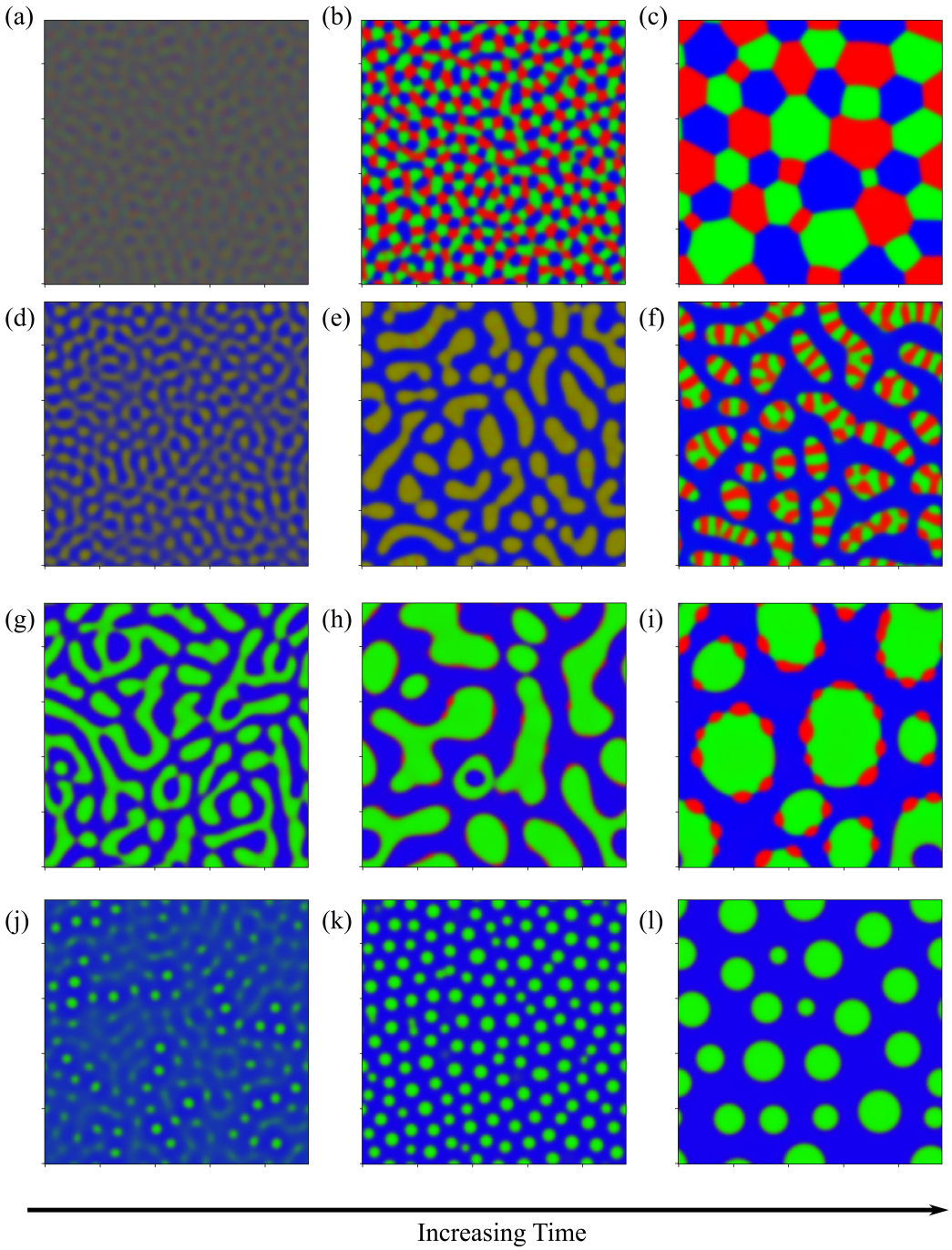

Figure 5.1: Four types of spontaneous phase separation pathways for ternary fluid mixtures: (a-c) direct ternary separation, (d-f) primary and secondary bulk phase separation, (g-i) enrichment and instability at interface, and (j-l) binary-like phase separation.

Type I of ternary phase separation is when all three fluid components begin to simultaneously separate. This is exemplified in Fig. 5.1(a-c), leading to what we term a lattice morphology. Here, separate domains corresponding to the three fluids are interspersed among each other, and domain coarsening occurs due to rearrangement and coalescence of alike domains.

For types II and III of ternary phase separation, the pathways consist of two stages, in contrast to only one stage for type I above. Fig. 5.1(d-f) illustrate type II where primary and secondary bulk separation (spinodal decomposition) occur consecutively. This most commonly leads to what we term the worm morphology, where there is a chain of alternating fluid domains. During the primary spinodal (panel e), two components (e.g. without any loss of generality, C_1 and C_2) remain mixed and together they separate out from the third (e.g. C_3) component. During the secondary bulk phase separation (panel f), the two initially mixed components undergo another spinodal decomposition.

An example of type III of ternary phase separation is shown in Fig. 5.1(g-i). Despite being the most occurring pathway (see phase diagrams in the following sections), surprisingly it has not been systematically described. If we focus on non-nucleation effects, unlike for the binary phase separation where spinodal decomposition is the sole driving mechanism for spontaneous phase separation, in ternary fluid case, we have an alternative mechanism. Here, the primary spinodal is followed by the enrichment of the minority component at the interface (panel h). When there is sufficient third component at the interface, this component eventually becomes unstable and form small droplets at the fluid-fluid interface (panel i). This type of ternary phase separation gives rise to patchy droplet morphology.

Finally, for type IV, as in Fig. 5.1(j-l), when there is insufficient minor component at the interface, the phase separation pathway is akin to the binary fluid case. Here, the smallest minority component is never fully phase separates but it is typically concentrated at the interface between the two more major components.

Our simulation results are consistent with previous works describing ternary phase separation pathways [68, 99]. However, many of the extensive morphologies and pathways previously tabulated are not fundamental and a result of stochastic collision and coalescence of different fluid structures. In contrast, here we have elucidated the four fundamental types of phase separation mechanisms.

5.2.2 Phase Diagram

Building on the four fundamental phase separation mechanisms identified in the previous sub-section, a natural question arises: can we predict which pathway and morphology will form given the mixture composition? In the literature to date, the phase diagram for ternary phase separation is commonly interpreted by performing a linear instability analysis and looking into the eigenvalues. This is a standard tool to understand phase separation via spinodal decomposition [27, 28, 230].

Suppose the system is initialised as a homogeneous mixture with small perturbations in composition, such that, in 1-D,

$$C_m(x, t = 0) = A_m + \sum_k^{\infty} \cos(kx)\alpha_{mk}(t = 0), \tag{5.1}$$

where the A_m's are the initial concentrations, and the $\alpha_{mk}(t)$'s describe the amplitudes of the perturbations, and k represents the wave vectors of the infinitely many possible modes for the perturbations. If we substitute the above equation into the Cahn-Hilliard equation, with zero initial velocity, to linear order we obtain (the prime denotes a time derivative)

$$\begin{pmatrix} \alpha'_{1k}(t) \\ \alpha'_{2k}(t) \end{pmatrix} = \begin{pmatrix} D_1 + F_{11} & F_{12} \\ F_{21} & D_2 + F_{22} \end{pmatrix} \begin{pmatrix} \alpha_{1k}(t) \\ \alpha_{2k}(t) \end{pmatrix} \tag{5.2}$$

with

$$D_i = \frac{-3}{4}\varepsilon k^4 - \frac{12}{\varepsilon}(6A_i^2 - 6A_i + 1)k^2, \tag{5.3}$$

$$F_{i1} = \frac{12\delta}{\varepsilon\Sigma_i}(A_2(1 - 2A_1 - A_2))k^2, \tag{5.4}$$

$$F_{i2} = \frac{12\delta}{\varepsilon\Sigma_i}(A_1(1 - 2A_2 - A_1))k^2. \tag{5.5}$$

Without any loss of generality, we have explicitly considered variations in C_1 and C_2. The third concentration can be obtained by using the constraint $C_3 = 1 - C_1 - C_2$. From Eqn. 5.2, the eigenvalues can then be determined:

$$\lambda^{\pm} = \frac{-b \pm \sqrt{b^2 - 4c}}{2}, \tag{5.6}$$

$$b = -(D_1 + F_{11} + D_2 + F_{22}), \tag{5.7}$$

$$c = (D_1 + F_{11})(D_2 + F_{22}) - F_{12}F_{21}. \tag{5.8}$$

The eigenvalues can be used to differentiate between three regions in the phase diagram: (i) where both eigenvalues are negative, (ii) where one is positive and one negative, and (iii) where both eigenvalues are positive. These regions are shown in Fig. 5.2 (a) in green, blue and red respectively. In our phase diagrams the corners of the triangle correspond to when one component is maximal, i.e. $C_1 = 1.0$ for the bottom right corner, $C_2 = 1.0$ for the top corner, and $C_3 = 1.0$ for the bottom left corner.

Numerically, we can also construct a phase diagram by varying the initial fluid composition and observing the resulting fluid structures in the simulations. This phase diagram is shown in Fig. 5.2 (b). Here, we have used red to represent direct ternary phase separation, gray for two-step primary and secondary spinodal decomposition, orange for enrichment and instability at interface, and blue for binary-like phase separation. When comparing the the two phase diagrams in Fig. 5.2 (a) and (b), we can immediately conclude that knowing only the eigenvalues is far from adequate for predicting ternary fluid phase separation. Hence, our next aim is to develop a simple phenomenological model that better describe the numerical phase diagram shown in Fig. 5.2(b).

From the numerical results, while the red region in Fig. 5.2(a) with two positive eigenvalue covers a significant area, we find the direct ternary phase separation scenario is very limited. Across all surface tension values we have studied, direct ternary phase separation is limited to compositions where all the concentrations satisfy $\frac{1}{3} \pm 5\%$. This is the region marked as red in Fig. 5.2(c). Geometrically, the

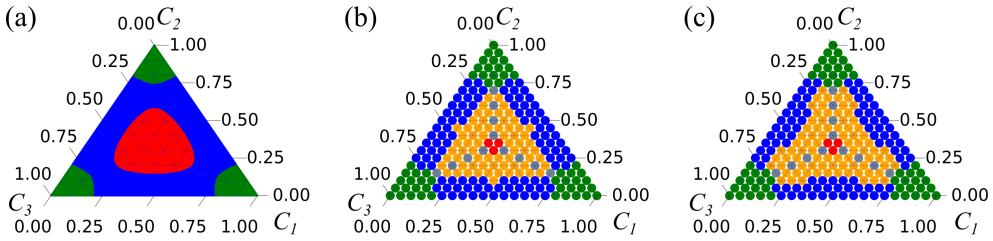

Figure 5.2: Phase diagrams obtained (a) from considering the signs of the eigenvalues from linear instability analysis, (b) from lattice Boltzmann simulation results, and (c) from the phenomenological model proposed in this work. In panel (a), the red, blue and green regions have two, one, and zero positive eigenvalues. In panels (b) and (c), red denotes the direct ternary phase separation mechanism, gray the primary and secondary bulk phase separation mechanism, orange the enrichment and instability at the interface mechanism, blue the binary-like mechanism, and green no phase separation. Note that the colour scheme for the eigenvalues, panel (a), is not equivalent to the colour scheme used for the other two, panels (b) and (c).

lattice morphology is favoured for such composition as there simply is not enough space for the other types of morphologies to form.

Next, we will study the two-step primary and secondary spinodal decomposition scenario. To do this, it is useful to consider the full linearised solution for the evolution of the perturbation amplitude, given by

$$\underline{\alpha}(t) = B^{+} \exp^{\lambda^{+} t}\, \underline{e}^{+} + B^{-} \exp^{\lambda^{-} t}\, \underline{e}^{-}, \tag{5.9}$$

where $B^{\pm}$ are fixed by the initial conditions, and $\underline{e}^{\pm}$ are the two eigenvectors corresponding to eigenvalues $\lambda^{\pm}$, as given in Eq. (5.6). For equal surface tension considered in this section, when $A_1 = A_2 = A$, we find $D_1 = D_2 = D$ and $F_{i1} = F_{i2} = F$, and the full linearised solution simplifies to

$$\underline{\alpha}(t) = B^{+} \exp^{\lambda^{+} t} \begin{pmatrix} 1 \\ 1 \end{pmatrix} + B^{-} \exp^{\lambda^{-} t} \begin{pmatrix} 1 \\ -1 \end{pmatrix} \tag{5.10}$$

with eigenvalues

$$\lambda^{\pm} = D + 2F, \qquad D. \tag{5.11}$$

The λ^{-} mode is the standard binary mode of separation where $D > 0$ leads to unstable situation. Here, the perturbations in C_1 and C_2 grow with opposite signs.

In contrast, for the λ^+ mode, the two components grow together at the same rate. Looking at the equation for F, its sign depends on a term proportional to $(1-3A)$. Hence, if $A < \frac{1}{3}$, $F > 0$, and $\lambda^+ > \lambda^-$. This condition corresponds to the gray points in Fig. 5.2(c). In fact, this condition should be a continuous line, but it appears discrete due to how we sample the phase diagram for consistency with the full numerical results in Fig. 5.2(b).

Dominant λ^+ mode explains the primary spinodal observed in Fig. 5.1(d-f), where two components grow together for a significant period and separate from the third fluid component. If the initial condition satisfies $A_1+A_2 < A_3$, as is the case in Fig. 5.1(d-f), the third component forms the background, while we observe droplets composed of C_1 and C_2 components. In contrast, if $A_1 + A_2 > A_3$, we find the opposite with C_3 droplets and a continuous phase of C_1 and C_2 mixture. However, these mixed domains cannot grow together indefinitely. At some point, they will enter the spinodal region for the binary mixture and the two components will undergo the secondary bulk phase diagram. As we step off from the $A_1 = A_2 < \frac{1}{3}$ line, we can derive that the eigenvectors do not support any two components to co-grow at the same rate. This limits the region in the ternary phase diagram that phase separates via the two step spinodal pathway.

For the rest of the phase diagram where there is at least one positive eigenvalue, considering the full linear solution leads to the conclusion that ternary phase separation is dominated by the two more major components, in agreement with the numerical results. Further, from energetic arguments, it is favourable for the minor component to be enriched at the interface, instead of uniformly diffused in the bulk of the major components. The remaining task in this case is to understand if and how the instability at interface takes place. Enrichment and instability at the interface is a novel mechanism that is not present is spontaneous phase separation of binary fluids.

To study this we simulate fluid strips in 2-D initialised with the following

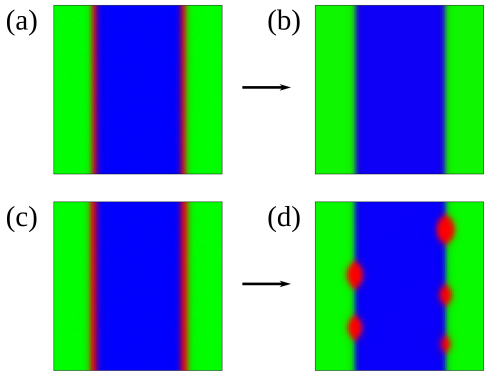

Figure 5.3: Evolution of the minority component initialised at the interface for (a-b) $a = 3\varepsilon/8$ and (c-d) $a = \varepsilon/2$.

concentration profile, as shown in Fig. 5.3:

$$C_1(r) = 1 - C_2(r) - C_3(r), \tag{5.12}$$

$$C_2(r) = \frac{1}{2}\left(1 + \tanh\left(\frac{2(r-R+a)}{\varepsilon}\right)\right), \tag{5.13}$$

$$C_3(r) = \frac{1}{2}\left(1 - \tanh\left(\frac{2(r-R-a)}{\varepsilon}\right)\right), \tag{5.14}$$

where r is the distance from the centre of a fluid strip, R is half the thickness of the strip, and a is the shift from an equilibrium hyperbolic tangent profile for a strip of C_2 surrounded by C_3. With increasing $a > 0$, we effectively introduce additional minority fluid component C_1 at the interface between C_2 and C_3. Numerically we find the minority component at the interface is stable for small a, Fig. 5.3(a-b), but it becomes unstable for large a, Fig. 5.3(a-b). The transition occurs as $a \sim \epsilon/2$, irrespective of the thickness of the strip. Hence, this instability is primarily determined by the amount of the minority component at the interface, relative to the interface length between the two major components. In addition, since this mode of phase separation requires an instability to form droplets, it is only possible when the spatial dimension is larger than two. It cannot occur in 1-D.

With this observation we can make a simple phenomenological model for when patchy droplets will occur. We first determine when spinodal decomposition will occur, i.e. when at least one of the eigenvalues is positive. Then we consider the

cases where type I and II do not occur. In these cases there are two possibilities left for phase separation, either following type III or IV pathway.

To predict the boundary between types III and IV, we make the following approximations. We assume that the minor component is evenly distributed at the interfaces. Without any loss of generality, here we have chosen fluid component 1 to be the minor component. Given the total amount of minor component present is V_1, and the interface length is L_I, then we can approximate the thickness of the minor component layer at the interfaces between C_2 and C_3 to be $w \sim V_1/L_I$. Following the results shown in Fig. 5.3, we expect instability leading to droplets formation to occur above $w \sim 2a \sim \varepsilon$.

If phase separation between the two major components (e.g. C_2 and C_3) continues indefinitely, L_I will decrease and w will increase monotonically with time. Hence, eventually we can expect the enrichment and instability mechanism to take place. However, in our simulations, we often observe meta-stable states where the phase separated droplets are well separated and they do not coalesce further. This limits the decrease in L_I and the increase in w. If the number of such droplets is N, then the total interface length is $L_I \sim 2\pi r_d N$, where r_d is the characteristic radius of the droplet given by $r_d \sim (V_1/\pi N)^{1/2}$. Combining this with the relations derived in the previous paragraph we find the enrichment and instability mechanism to be observed when

$$\varepsilon \sim \left(2\pi \frac{V_1}{N}\right)^{1/2} \sim \left(2\pi \frac{V_1}{V_T}\frac{V_T}{N}\right)^{1/2} \sim \left(2\pi \frac{A_1}{n}\right)^{1/2}. \tag{5.15}$$

Here A_1 is the average concentration of the C_1 component in the system, V_T is the total volume of the simulation, and n is the typical density of isolated droplets. Fitting n to obtain the best comparison between the phase diagrams in Fig. 5.2(b-c), we obtain $n \sim 1.7$ x10^{-4}. In practice, the number of isolated droplets observed does vary depending on the initial concentrations. However, they are in the same order as the fitted value of n. Importantly, as n is an intensive variable, our argument holds independent of the system size.

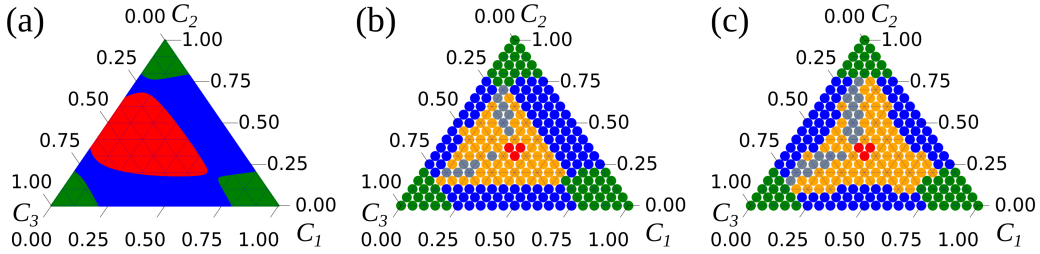

Figure 5.4: Phase diagrams for non equal surface tensions where $\Sigma_3 = 9\Sigma_1$, $\Sigma_2 = 4\Sigma_1$. In panel (a), the red, blue and green regions have two, one, and zero positive eigenvalues. Panel (b) is the numerically obtained phase diagram, while panel (c) is our theoretical prediction. In panels (b) and (c), red denotes the direct ternary phase separation mechanism, gray the primary and secondary bulk phase separation mechanism, orange the enrichment and instability at the interface mechanism, blue the binary-like mechanism, and green no phase separation. Note that the colour scheme for the eigenvalues, panel (a), is not equivalent to the colour scheme used for the other two, panels (b) and (c).

5.3 Non-Equal Surface Tensions

Having elucidated the case for equal surface tensions, we now generalise our argument for the non equal surface tensions case. As a representative example, here we choose $\Sigma_3 = 9\Sigma_1$, $\Sigma_2 = 4\Sigma_1$ in the free energy model, such that $\gamma_{23}/\gamma_{12} = 2.6$ and $\gamma_{13}/\gamma_{12} = 2.0$. This set of parameters corresponds to the formation of Neumann angles $\theta_1 = 63.9°$, $\theta_2 = 136.3°$, and $\theta_3 = 159.8°$ at the three phase contact line.

A major difference for non-equal surface tensions is the occurrence of secondary bulk separation. The criteria needs to be broadened, as it is possible for secondary bulk separation to occur even if the eigenvector components are not equal. This is because the different surface tensions give rise to varying growth rates for each of the fluid component, and this has a complex interplay with the initial fluid concentrations. Similar to the equal surface tension criteria, we focus on the largest positive eigenvalue and its corresponding eigenvector. Following Eq. (5.10), with e_1 and e_2 the components of the eigenvector with the largest positive eigenvalue, we consider two possible conditions for secondary bulk phase separation to be observed. First, if $C_1 = C_2$ and $e_1 = e_2$, where the two components grow together. This is the same condition as discussed in the previous section, but in fact this condition is rare

to achieve when the surface tensions of the fluid interfaces are not equal. As before, without any loss of generality, we explicitly consider concentration variations in C_1 and C_2, and the third component can be obtained via $C_3 = 1 - C_1 - C_2$. Second, if one component has a lower initial concentration ($C_1 < C_2$), but its fluctuation has a faster growth rate $e_1 > e_2$ (or vice versa for $C_2 < C_1$). In such a case, the two components are mixed together for some period before eventually phase separating.

Using this updated condition for the secondary bulk phase separation, along with the other conditions as described for equal surface tensions, we can compare the resulting phase diagrams. Fig. 5.4 (a) shows the eigenvalue analysis, while (b) and (c) which represent the numerical and theoretical results respectively. As before, the eigenvalue analysis has little predictive value for the morphologies observed in the simulations. Comparing Figs. 5.4(b) and (c), we further find that our analysis extends to general surface tension values. It is clear that the key trends are captured for each phase separation mechanism, even though the boundaries of the different regions are less accurate when compared to the equal surface tension case.

The deviations observed are mainly due to two reasons. First, at the boundary between binary-like and enrichment mechanisms, the minor component does not always enrich at the interface, especially when its total amount is very small compared to the simulation size. Here, the minor component remains mixed in the background components. Such tendency is more common with increasing surface tension, as it becomes more costly energetically to create interfaces.

Second, at the boundary between enrichment and secondary bulk phase separation mechanisms, there are several sources of uncertainties to classify the phase separation mechanism. In particular, the separation between the two more minor components may take place within a small droplet and before the components clearly reach their expected bulk values. Furthermore, the condition $C_1 < C_2$ and $e_1 > e_2$ may not be sufficient to induce secondary bulk separation as e_1 may need to be significantly larger than our algorithm would predict.

To further highlight the importance of the eigenvectors in the phase separation dynamics, consider the results shown in Fig. 5.5. Here, we initialise the simulation with $A_1 = 0.1$ (red), $A_2 = 0.7$ (green), and $A_3 = 0.2$ (blue), and the normalised eigenvector corresponding to the largest positive eigenvalue is calculated to be $(e_1, e_2, e_3) = (-0.580, 0.788, -0.208)$. In agreement with our updated condition, both C_1 and C_3 remain mixed together for a significant length of time as the composite droplets emerge from the C_2 background. Then, despite the C_1 component being the most minor component, we observe it separates out before the second minor component C_3. This is precisely because the eigenvector component for C_1 is twice larger compared to C_3. The component C_3 eventually begins to enrich at the interfaces to form patches.

Finally, we make a geometric observation of why the worm morphology is not possible here during phase separation. Since the Neumann angle $\theta_1 < 90°$, the domains enriched in C_1 will form concave capillary bridges with negative pressure compared to their surroundings. These will lead to the surrounding domains quickly merging together, and as a result, the worm morphology cannot be supported.

5.4 Conclusion

In this work, we have systematically simulated spontaneous phase separation of ternary fluid mixtures across the composition space, both when all the fluid surface tensions are equal and when they all have different values. We have identified four fundamental phase separation mechanisms, which we term as (I) direct ternary phase separation, (II) primary and secondary bulk phase separation, (III) enrichment and instability at interface, and (IV) binary-like. Typically, these mechanisms respectibely lead to lattice, worm, patchy droplet and droplet morphologies.

In contrast to binary phase separation, to understand the phase separation pathways, we have shown that the eigenvalues alone are insufficient, and it is important to consider both the eigenvalues and eigenvectors. Such consideration is

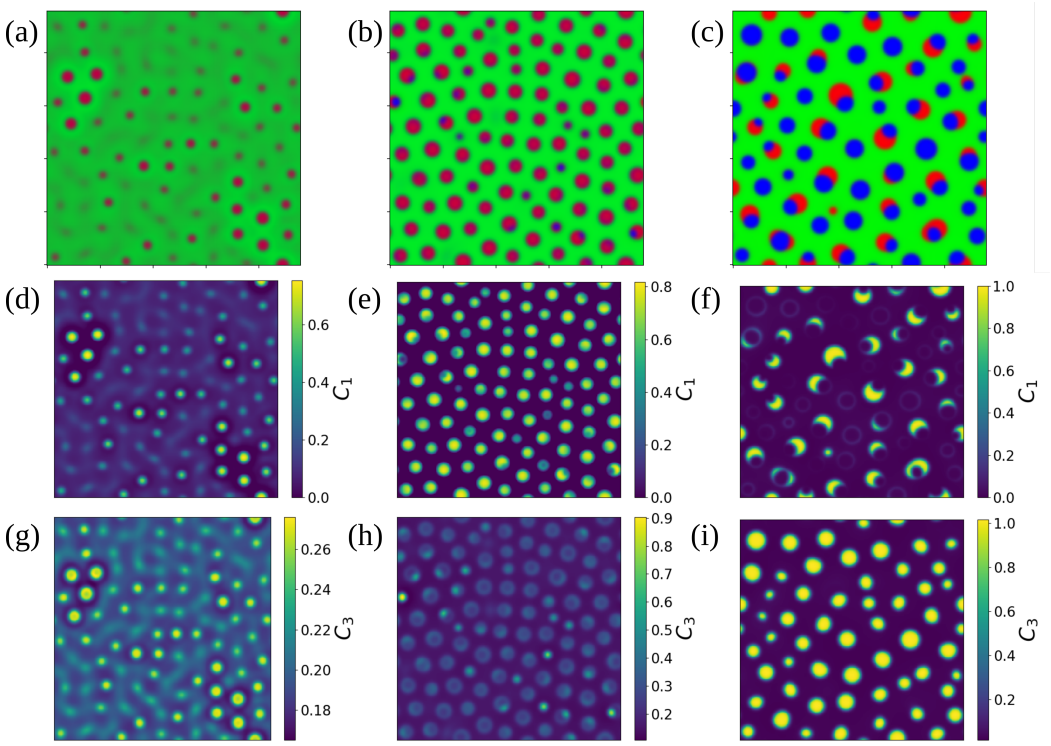

Figure 5.5: Phase separation dynamics for initial concentrations: $C_1 = 0.1$ (red), $C_2 = 0.7$ (green), and $C_3 = 0.2$ (blue), with time evolving from left to right. Panels (a-c) show all components at once, while panels (d-f) and (g-i) only show C_1 and C_3.

in good agreement with direct simulation results, and it leads us to the conclusion that the enrichment and instability at interface mechanism is the dominant mechanism in ternary fluid phase separation. Yet, surprisingly, to our knowledge, it has been overlooked so far in the literature.

We have also studied a range of viscosity ratios (up to a maximum of 10, data not shown). We find no significant changes in the resulting separation pathways, though it remains an open question how larger ratios may affect the phase separation dynamics. In the future, it will also be interesting to extend the study to three dimensional phase separation and to consider more than three fluid components, including when the components are all immiscible and when they are partially miscible.

Chapter 6

Conclusion

In this thesis, we were interested in key interfacial phenomena where key ternary fluid effects are seen, which have no analogy from the binary system. We studied three problems: capillary bridges, de-wetting and phase separation.

First, we studied how the force of a capillary bridge between two liquid infused surfaces (LIS) compared with a capillary bridge between two smooth surfaces at varying interfacial tensions and contact angles. For single component liquid capillary bridges, the capillary force, in the absence of external forces such as gravity, can be determined by three factors: the interfacial tension of the droplet-gas interface, the Young's contact angle of the droplet and the volume of the droplet. For capillary bridges on liquid-infused surfaces, there are two liquid components. We found that in addition to the interfacial tensions, contact angles and volumes of the liquids, the interaction between the three fluids characterised by the Neumann angles also play a significant role in determining the capillary force.

By using the concept of an apparent contact angle, we attempted to create one to one comparisons with the single component capillary bridge. Our observations highlighted that the apparent contact angle alone could not describe the capillary force behaviour, reinforcing the notion that there are ternary effects which cannot be captured using purely binary concepts. The Neumann angles have a significant impact on the shape of the lubricant ridge where the flatter the lubricant ridge the

closer the capillary force would behave like the binary case. However, we found for sharp lubricant ridges the capillary force can be enhanced. Additionally we found several capillary bridge morphologies which have no analogue with the single liquid component capillary bridges. Again, we found that the Neumann angles and apparent contact angle both play a critical role in whether such capillary bridge morphologies are possible.

We also introduced a novel mechanism for cleaning by studying the de-wetting of a soil droplet from a flat substrate using the triple fluid contact to pull the and stretch droplet away from the surface. Our approach relies on the physics at the triple fluid junction differing from a binary fluid system.

By explicitly simulating the movement of the liquid-gas interfaces, our studies showed how such a scenario can be understood to some degree as a capillary bridge, but with the surrounding gas acting as the top surface. Drawing from our knowledge of Neumann angles and apparent contact angles, we can understand qualitatively why certain interfacial tension formulations can result in soil droplets de-wetting (or not). Importantly the Young's contact angles on the solid surface are insufficient to determine the de-wettability of the droplet. The Neumann angles at the droplet-formulation-gas triplet point also play a significant factor on the droplet's de-wettability.

We further found that when significant momentum is inputted into the system the momentum can aid or hinder de-wetting. we saw two categories of behaviour: for convex droplets momentum is usually beneficial to partially remove the soil in comparison to when little momentum is inputted; while momentum is detrimental for concave droplets. Crudely, the criteria for convex and concave droplets can be determined from the Neumann angles and the surface contact angles, which again highlights the importance of the triple contact junction, and further reinforces that this mechanism is truly a ternary fluid effect.

From the perspective of resource usage, we found such a controlled input of

cleaning formulation has the potential to minimise their use, both in raw materials and energy in comparison to more traditional methods of cleaning. This differs from a binary approach which would typically involve flooding the system with cleanser fluid and then relying on momentum and altering the contact angles of the soil droplet to induce de-wetting. Practically speaking, the formulation could be introduced slowly by soaking or slowly submerging the surface. So long as the three fluid contact line has enough time to form, then ternary lift-off should be possible.

Finally, we studied how phase separation is affected by three fluid interactions. We have categorised the possible structures which can result, identifying four separation pathways and morphologies. This contrasts with phase separation in binary fluids which can be thought of having only one type of separation pathway.

We highlight how in a ternary mixture there are two scenarios which involve two stages of phase separation: secondary bulk separation, and enrichment and instability at interface. Such scenarios are simply not possible in binary fluids mixtures. By performing linear stability analysis we gained an understanding of when such structures and separation pathways occur. Unlike for the binary case, we highlighted the importance of considering the eigenvector components which result when performing linear stability analysis, and not just the eigenvalues alone as is typical in the literature.

6.1 Future Work

There are several possibilities for future research. From the modelling perspective, it will be interesting to develop a fully consistent free energy model and method for both the bulk fluid physics and fluid-solid interactions that can be extended to N-component cases. There are already several works in the literature in this direction [108, 106, 107, 104]. A good N-component model will need to be reducible and avoid

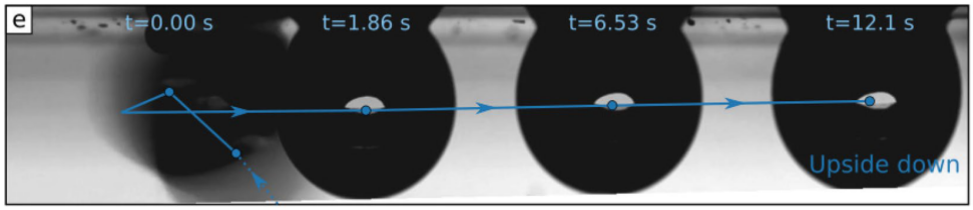

Figure 6.1: Here we show experimental results of a droplet moving upside down on a liquid infused surface. Used under Creative Commons Attribution 4.0 International License license from Nature, Scientific Reports, Self-propelled droplet transport on shaped-liquid surfaces, G Launay et al. Copyright 2020.

spurious condensation at the interface and/or contact line. It must also allow the interfacial tensions to be freely varied including for complete spreading cases.

Thus far liquid infused surfaces have been considered primarily for its slippery properties. However, we have highlighted that such surfaces are only slippery in the direction parallel to the surface, and they can be quite sticky in the perpendicular direction. There are already some studies which highlight this stickiness [231], but more in depth experimental evidence of the effect of varying interfacial tensions is needed. For example, see Fig. 6.1 where a droplet is shown moving upside down on LIS [231], highlighting the sticky nature of LIS. It would also be optimal for future experimental research to focus on regimes where the surface structures are well wetted to provide enough lubricant to form a large lubricant ridge to emphasise any effects varying surface tension would have. Precise experiments could be performed to verify the force curves. These could follow the method used by de Souza et al [54], but this time using LIS as the substrates. Here they attach the upper substrate to a cantilever mechanism, and measure the deflection to calculate the capillary force. Care however, must be taken to ensure the effect of gravity is minimised by ensuring the droplet size is well below the relevant capillary length.

We envision that LIS being sticky and slippery can open up new areas for applications. An example could be the atmospheric capture of water vapour [232], where the strong capillary adhesion combined with the slippery could be used to capture water vapour and its slippery surface to transport the captured water.

In this thesis, a novel mechanism for de-wetting droplets has been studied numerically, but experimental verification is also required. To verify our results, it would be optimal to study small droplets such that gravity effects are minimised, so the lift-off mechanism is more apparent. If it is necessary to study larger droplets, it would be ideal to begin with scenarios where the soil and formulation have equal or similar density. We have already shown that buoyancy can play a significant role in affecting the outcome, and to isolate the lift-off mechanism, these factors cannot be ignored.

As part of the overall strategy on resource constrained cleaning, we could consider other related methods to de-wet a droplet. In cases where full de-wetting is not possible, we can consider adding kinetic energy from other external perturbations. For example, one can consider oscillating the solid substrate or inducing pressure waves to the system. If such a method does allow for de-wetting, then significant reductions in resources, such as water and surfactant usage, could be attained even in cases where spontaneous ternary lift-off is not possible.

In such a study one would need to take care that oscillations are applied at different liquid film thicknesses, as the ternary lift-off mechanism has been shown to stretch droplets similar to a capillary bridge. We have shown that the energy barrier between a de-wetted and a stretched droplet decreases as the thickness of the liquid film is increased. One could infer from such an observation that less kinetic energy would be needed to de-wet the droplet if the liquid film thickness is increased. An experiment could be performed where a soil droplet is resting on a substrate. Formulation could be introduced in two ways. One method could be to place the substrate in a box with an inlet for the formulation very similar to the method modelled here. Another could be to have a bath of the formulation and slowly submerge the substrate with the soil droplet into the bath, thereby simulating the scenario of a formulation film lifting the soil droplet.

We have also studied phase separation in 2D for ternary mixtures. Perhaps the next simplest step is to verify if our results have analogues when undergoing phase

separation in 3D. It seems plausible that secondary bulk separation is likely to occur in a similar manner. However, it is not so obvious the enrichment and instability of the interface mechanism would be completely analogous. In our analysis we highlighted that such a process is dependent on the interface length. Naturally, when extended to 3D this would have to become an interfacial area. We have also highlighted that instability at interfaces is not possible in 1D as there is no direction for the minor component to flow to coalesce and separate out from the interface. Hence, it seems likely that the extra dimension may have much more of a significant impact here.

To verify these experimentally we could follow the method by Nauman et al. [68], where for 2D cases they studied a film composed of a mixture of polymers and solvents to verify some of the structures which can form. A similar set of studies can be performed, for greater variety of polymers and solvents. However, the difficulty lies in any potential 3D experiments. Here, it is not obvious how easy it would be to verify structures visually if the various fluids are not transparent. This may lead to a strong limitation in the variety of fluids studied which can lead to concrete results. To alleviate this to some degree 3D simulations can be studied in tandem, especially if the 3D structures found numerically produces characteristic cross-sectional profiles.

More broadly, we can also study phase separation for N-component fluid mixtures. The key questions here would be if similar separation pathways are possible, and whether there may even be a limit to how complicated structures can form. For instance, there is a mathematical theorem known as the four colour theorem [233], which states that no more than four colours are needed to cover a 2D space with no two adjacent areas being the same colour. It would be interesting to study whether quaternary mixtures may be the limit to possible structural complexity when mixtures phase separate.

Another open question is what would be the equivalent of Neumann angles in higher order mixtures. Is it even possible to have anything more complicated,

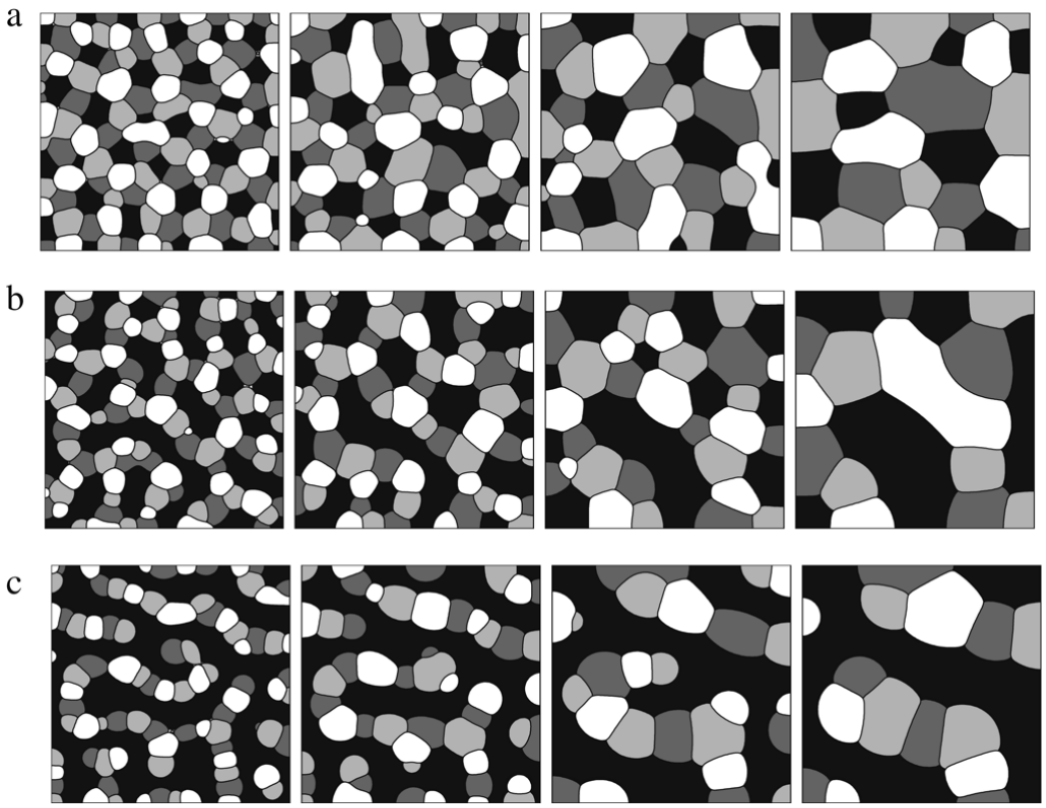

Figure 6.2: Here we show numerical results for quaternary fluid mixtures undergoing phase separation for equal surface tensions . Each different shade from white to black is a separate fluid. Reprinted from Physica A: Statistical Mechanics and its Applications, 387, H. G. Lee et al., A second-order accurate non-linear difference scheme for the N -component Cahn–Hilliard system, volume 13, Copyright 2008, with permission from Elsevier.

such as a four phase junction. Fig. 6.2 shows numerical simulations obtained for quaternary fluid mixtures undergoing phase separation by Kim et al. [234]. From their work they do not observe any four-fluid junction. However, we must note that such simulations by Kim et al. [234] did not test significant variations on the phase space, rather they used the simulations to validate the numerical method they developed.

Bibliography

[1] T. S. Bowers and H. C. Helgeson, "Calculation of the thermodynamic and geochemical consequences of nonideal mixing in the system h2o-co2-nacl on phase relations in geologic systems: Equation of state for h2o-co2-nacl fluids at high pressures and temperatures," *Geochimica et Cosmochimica Acta*, vol. 47, pp. 1247–1275, 1983.

[2] S. Mao, Z. Duan, and W. Hu, "A vapor–liquid phase equilibrium model for binary co2–h2o and ch4–h2o systems above 523 k for application to fluid inclusions," *The Journal of Supercritical Fluids*, vol. 50, pp. 13–21, 2009.

[3] V.-H. Le, M.-C. Caumon, A. Tarantola, A. Randi, P. Robert, and J. Mullis, "Calibration data for simultaneous determination of pvx properties of binary and ternary co2-ch4-n2 gas mixtures by raman spectroscopy over 5–600 bar: Application to natural fluid inclusions," *Chemical Geology*, vol. 552, p. 119783, 2020.

[4] R. Freedman, S. Lo, M. Flaum, G. Hirasaki, A. Matteson, and A. Sezginer, "A new nmr method of fluid characterization in reservoir rocks: Experimental confirmation and simulation results," *Society of Petroleum Engineers Journal*, vol. 6, pp. 452–464, 2001.

[5] G. Duan, B. Chen, X. Zhang, and Y. Wang, "A multiphase mps solver for

modeling multi-fluid interaction with free surface and its application in oil spill," *Computer Methods in Applied Mechanics and Engineering*, vol. 320, pp. 133–161, 2017.

[6] J. Xu, J. Kou, L. Guo, H. Jin, Z. Peng, and C. Ren, "Experimental study on oil-containing wastewater gasification in supercritical water in a continuous system," *International Journal of Hydrogen Energy*, vol. 44, pp. 15871–15881, 2019.

[7] N. Andersson and G. Comer, "A flux-conservative formalism for convective and dissipative multi-fluid systems, with application to newtonian superfluid neutron stars," *Classical and Quantum Gravity*, vol. 23, p. 5505, 2006.

[8] S. M. Mahajan and M. Lingam, "Multi-fluid systems—multi-beltrami relaxed states and their implications," *Physics of Plasmas*, vol. 22, p. 092123, 2015.

[9] S. Gondal, M. Iqbal, A. H. Khosa, and G. Murtaza, "Quadruple beltrami fields in three component plasmas," *Physics of Plasmas*, vol. 24, p. 062903, 2017.

[10] M.-T. Wei, S. Elbaum-Garfinkle, A. S. Holehouse, C. C.-H. Chen, r. Feric, C. B. Arnold, R. D. Priestley, R. V. Pappu, and C. P. Brangwynne, "Phase behaviour of disordered proteins underlying low density and high permeability of liquid organelles," *Nature Chemistry*, vol. 9, pp. 1118–1125, 2017.

[11] S. Boeynaems, S. Alberti, N. L. Fawzi, T. Mittag, M. Polymenidou, F. Rousseau, J. Schymkowitz, J. Shorter, B. Wolozin, L. Van Den Bosch, *et al.*, "Protein phase separation: a new phase in cell biology," *Trends in Cell Biology*, vol. 28, pp. 420–435, 2018.

[12] D. Bracha, M. T. Walls, and C. P. Brangwynne, "Probing and engineering liquid-phase organelles," *Nature Biotechnology*, vol. 37, pp. 1435–1445, 2019.

[13] C. Chatelain, T. Balois, P. Ciarletta, and M. B. Amar, "Emergence of microstructural patterns in skin cancer: a phase separation analysis in a binary mixture," *New Journal of Physics*, vol. 13, p. 115013, 2011.

[14] E. Tjhung, A. Tiribocchi, D. Marenduzzo, and M. E. Cates, "A minimal physical model captures the shapes of crawling cells," *Nature Communications*, vol. 6, pp. 1–9, 2015.

[15] P. Sahu, D. M. Sussman, M. Rübsam, A. F. Mertz, V. Horsley, E. R. Dufresne, C. M. Niessen, M. C. Marchetti, M. L. Manning, and J. M. Schwarz, "Small-scale demixing in confluent biological tissues," *Soft Matter*, vol. 16, pp. 3325–3337, 2020.

[16] W. Federle, M. Riehle, A. S. Curtis, and R. J. Full, "An integrative study of insect adhesion: mechanics and wet adhesion of pretarsal pads in ants," *Integrative and Comparative Biology*, vol. 42, pp. 1100–1106, 2002.

[17] L. Xue, A. Kovalev, A. Eichler-Volf, M. Steinhart, and S. N. Gorb, "Humidity-enhanced wet adhesion on insect-inspired fibrillar adhesive pads," *Nature Communications*, vol. 6, pp. 1–9, 2015.

[18] Y. Song, Z. Dai, Z. Wang, A. Ji, and S. N. Gorb, "The synergy between the insect-inspired claws and adhesive pads increases the attachment ability on various rough surfaces," *Scientific Reports*, vol. 6, pp. 1–9, 2016.

[19] L. J. De Cock, S. De Koker, B. G. De Geest, J. Grooten, C. Vervaet, J. P. Remon, G. B. Sukhorukov, and M. N. Antipina, "Polymeric multilayer capsules in drug delivery," *Angewandte Chemie International Edition*, vol. 49, pp. 6954–6973, 2010.

[20] S. De Koker, R. Hoogenboom, and B. G. De Geest, "Polymeric multilayer capsules for drug delivery," *Chemical Society Reviews*, vol. 41, pp. 2867–2884, 2012.

[21] D. Guzey and D. J. McClements, "Formation, stability and properties of multilayer emulsions for application in the food industry," *Advances in Colloid and Interface Science*, vol. 128, pp. 227–248, 2006.

[22] O. Benjamin, P. Silcock, M. Leus, and D. Everett, "Multilayer emulsions as delivery systems for controlled release of volatile compounds using ph and salt triggers," *Food Hydrocolloids*, vol. 27, pp. 109–118, 2012.

[23] C. Burgos-Díaz, T. Wandersleben, A. M. Marqués, and M. Rubilar, "Multilayer emulsions stabilized by vegetable proteins and polysaccharides," *Current Opinion in Colloid & Interface Science*, vol. 25, pp. 51–57, 2016.

[24] M. E. Paulaitis, V. J. Krukonis, R. T. Kurnik, and R. C. Reid, "Supercritical fluid extraction.," *Reviews in Chemical Engineering*, vol. 1, pp. 179–250, 1983.

[25] S. K. Luther and A. Braeuer, "High-pressure microfluidics for the investigation into multi-phase systems using the supercritical fluid extraction of emulsions (sfee)," *The Journal of Supercritical Fluids*, vol. 65, pp. 78–86, 2012.

[26] B. Pavlić, O. Bera, N. Teslić, S. Vidović, G. Parpinello, and Z. Zeković, "Chemical profile and antioxidant activity of sage herbal dust extracts obtained by supercritical fluid extraction," *Industrial Crops and Products*, vol. 120, pp. 305–312, 2018.

[27] J. W. Cahn, "On spinodal decomposition," *Acta Metallurgica*, vol. 9, pp. 795–801, 1961.

[28] J. W. Cahn, "Phase separation by spinodal decomposition in isotropic systems," *The Journal of Chemical Physics*, vol. 42, pp. 93–99, 1965.

[29] Y. Gelbstein, J. Davidow, S. N. Girard, D. Y. Chung, and M. Kanatzidis, "Controlling metallurgical phase separation reactions of the ge0. 87pb0.

13te alloy for high thermoelectric performance," *Advanced Energy Materials*, vol. 3, pp. 815–820, 2013.

[30] M. C. Oh, A. Sharma, H. Lee, and B. Ahn, "Phase separation and mechanical behavior of alcocrfeni-x (x= cu, mn, ti) high entropy alloys processed via powder metallurgy," *Intermetallics*, vol. 139, p. 107369, 2021.

[31] S. P. Adiga and D. W. Brenner, "Flow control through polymer-grafted smart nanofluidic channels: molecular dynamics simulations," *Nano Letters*, vol. 5, pp. 2509–2514, 2005.

[32] X. Yong and L. T. Zhang, "Thermostats and thermostat strategies for molecular dynamics simulations of nanofluidics," *The Journal of Chemical Physics*, vol. 138, p. 084503, 2013.

[33] X. Chen, "Molecular dynamics simulation of nanofluidics," *Reviews in Chemical Engineering*, vol. 34, pp. 875–885, 2018.

[34] C. Liu and Z. Li, "On the validity of the navier-stokes equations for nanoscale liquid flows: The role of channel size," *American Institute of Physics Advances*, vol. 1, p. 032108, 2011.

[35] X. Zhang, F. Shi, J. Niu, Y. Jiang, and Z. Wang, "Superhydrophobic surfaces: from structural control to functional application," *Journal of Materials Chemistry*, vol. 18, pp. 621–633, 2008.

[36] X. Zhang, L. Wang, and E. Levänen, "Superhydrophobic surfaces for the reduction of bacterial adhesion," *Royal Society of Chemistry Advances*, vol. 3, pp. 12003–12020, 2013.

[37] W. Carter, "The forces and behavior of fluids constrained by solids," *Acta Metallurgica*, vol. 36, pp. 2283–2292, 1988.

[38] E. De Souza, M. Brinkmann, C. Mohrdieck, and E. Arzt, "Enhancement of capillary forces by multiple liquid bridges," *Langmuir*, vol. 24, pp. 8813–8820, 2008.

[39] H. Kusumaatmaja and J. Yeomans, "Modeling contact angle hysteresis on chemically patterned and superhydrophobic surfaces," *Langmuir*, vol. 23, p. 6019, 2007.

[40] J. R. Landel and D. I. Wilson, "The fluid mechanics of cleaning and decontamination of surfaces," *Annual Review of Fluid Mechanics*, vol. 53, pp. 147–171, 2021.

[41] A. Cassie and S. Baxter, "Wettability of porous surfaces," *Transactions of the Faraday Society*, vol. 40, pp. 546–551, 1944.

[42] R. N. Wenzel, "Resistance of solid surfaces to wetting by water," *Industrial & Engineering Chemistry*, vol. 28, pp. 988–994, 1936.

[43] L. Gao and T. J. McCarthy, "Contact angle hysteresis explained," *Langmuir*, vol. 22, pp. 6234–6237, 2006.

[44] J. Joanny and P.-G. De Gennes, "A model for contact angle hysteresis," *The Journal of Chemical Physics*, vol. 81, pp. 552–562, 1984.

[45] D. I. Yu, S. W. Doh, H. J. Kwak, H. C. Kang, H. S. Ahn, H. S. Park, M. Kiyofumi, and M. H. Kim, "Wetting state on hydrophilic and hydrophobic micro-textured surfaces: Thermodynamic analysis and x-ray visualization," *Applied Physics Letters*, vol. 106, p. 171602, 2015.

[46] J. Bico, U. Thiele, and D. Quéré, "Wetting of textured surfaces," *Colloids and Surfaces A: Physicochemical and Engineering Aspects*, vol. 206, pp. 41–46, 2002.

[47] W. Barthlott and C. Neinhuis, "Purity of the sacred lotus, or escape from contamination in biological surfaces," *Planta*, vol. 202, pp. 1–8, 1997.

[48] A. Marmur, "The lotus effect: superhydrophobicity and metastability," *Langmuir*, vol. 20, pp. 3517–3519, 2004.

[49] Y.-T. Cheng and D. E. Rodak, "Is the lotus leaf superhydrophobic?," *Applied Physics Letters*, vol. 86, p. 144101, 2005.

[50] R. J. Vrancken, H. Kusumaatmaja, K. Hermans, A. M. Prenen, O. Pierre-Louis, C. W. Bastiaansen, and D. J. Broer, "Fully reversible transition from wenzel to cassie- baxter states on corrugated superhydrophobic surfaces," *Langmuir*, vol. 26, pp. 3335–3341, 2010.

[51] B.-X. Zhang, S.-L. Wang, and X.-D. Wang, "Wetting transition from the cassie–baxter state to the wenzel state on regularly nanostructured surfaces induced by an electric field," *Langmuir*, vol. 35, pp. 662–670, 2019.

[52] D. Murakami, H. Jinnai, and A. Takahara, "Wetting transition from the cassie–baxter state to the wenzel state on textured polymer surfaces," *Langmuir*, vol. 30, pp. 2061–2067, 2014.

[53] W. Barthlott, M. Mail, and C. Neinhuis, "Superhydrophobic hierarchically structured surfaces in biology: evolution, structural principles and biomimetic applications," *Philosophical Transactions of the Royal Society A: Mathematical, Physical and Engineering Sciences*, vol. 374, p. 20160191, 2016.

[54] E. De Souza, M. Brinkmann, C. Mohrdieck, A. Crosby, and E. Arzt, "Capillary forces between chemically different substrates," *Langmuir*, vol. 24, pp. 10161–10168, 2008.

[55] E. De Souza, L. Gao, T. McCarthy, E. Arzt, and A. Crosby, "Effect of contact angle hysteresis on the measurement of capillary forces," *Langmuir*, vol. 24, pp. 1391–1396, 2008.

[56] H. Lee, B. P. Lee, and P. B. Messersmith, "A reversible wet/dry adhesive inspired by mussels and geckos," *Nature*, vol. 448, pp. 338–341, 2007.

[57] M. J. Vogel and P. H. Steen, "Capillarity-based switchable adhesion," *Proceedings of the National Academy of Sciences U.S.A*, vol. 107, pp. 3377–3381, 2010.

[58] H. W. Kang, H. J. Sung, T.-M. Lee, D.-S. Kim, and C.-J. Kim, "Liquid transfer between two separating plates for micro-gravure-offset printing," *Journal of Micromechanics and Microengineering*, vol. 19, p. 015025, 2008.

[59] S. Dodds, M. Carvalho, and S. Kumar, "Stretching liquid bridges with moving contact lines: The role of inertia," *Physics of Fluids*, vol. 23, p. 092101, 2011.

[60] J. H. Snoeijer and B. Andreotti, "Moving contact lines: scales, regimes, and dynamical transitions," *Annual Review of Fluid Mechanics*, vol. 45, pp. 269–292, 2013.

[61] Y. D. Shikhmurzaev, "Singularities at the moving contact line. mathematical, physical and computational aspects," *Physica D: Nonlinear Phenomena*, vol. 217, pp. 121–133, 2006.

[62] D. M. Huang, C. Sendner, D. Horinek, R. R. Netz, and L. Bocquet, "Water slippage versus contact angle: A quasiuniversal relationship," *Physical Review Letters*, vol. 101, p. 226101, 2008.

[63] M. Wörner, X. Cai, H. Alla, and P. Yue, "A semi-analytical method to estimate the effective slip length of spreading spherical-cap shaped droplets using cox theory," *Fluid Dynamics Research*, vol. 50, p. 035501, 2018.

[64] J. Goldsbrough, "The spinodal—its impact on metallurgy, glass technology and polymer science," *Science Progress (1933-)*, pp. 281–297, 1972.

[65] S.-H. Si, H. Zhang, Y.-Z. He, M.-X. Li, and S. Guo, "Liquid phase separation and the aging effect on mechanical and electrical properties of laser rapidly solidified cu100- xcrx alloys," *Metals*, vol. 5, pp. 2119–2127, 2015.

[66] X. Kuang, F. Pan, J. Cao, C. Liang, M. R. Suchomel, F. Porcher, and M. Allix, "Defect structure, phase separation, and electrical properties of nonstoichiometric tetragonal tungsten bronze ba0. 5–x tao3–x," *Inorganic Chemistry*, vol. 52, pp. 13244–13252, 2013.

[67] O. J. Cayre and S. Biggs, "Hollow microspheres with binary porous membranes from solid-stabilised emulsion templates," *Journal of Materials Chemistry*, vol. 19, pp. 2724–2728, 2009.

[68] E. B. Nauman and D. Q. He, "Morphology predictions for ternary polymer blends undergoing spinodal decomposition," *Polymer*, vol. 35, pp. 2243–2255, 1994.

[69] X. Liu, N. Bhandaru, M. Banik, X. Wang, A. M. Al-Enizi, A. Karim, and R. Mukherjee, "Capillary force lithography pattern-directed self-assembly (cfl-pdsa) of phase-separating polymer blend thin films," *American Chemical Society Omega*, vol. 3, pp. 2161–2168, 2018.

[70] S. Biria and I. D. Hosein, "Superhydrophobic microporous substrates via photocuring: coupling optical pattern formation to phase separation for process-tunable pore architectures," *American Chemical Society Applied Materials & Interfaces*, vol. 10, pp. 3094–3105, 2018.

[71] W. Ma, M. Li, X. Zhou, J. Li, Y. Dong, and M. Zhu, "Three-dimensional porous carbon nanotubes/reduced graphene oxide fiber from rapid phase separation for a high-rate all-solid-state supercapacitor," *American Chemical Society Applied Materials & Interfaces*, vol. 11, pp. 9283–9290, 2019.

[72] H. Tanaka, "Viscoelastic phase separation," *Journal of Physics: Condensed Matter*, vol. 12, p. R207, 2000.

[73] A. Wagner and J. Yeomans, "Phase separation under shear in two-dimensional binary fluids," *Physical Review E*, vol. 59, p. 4366, 1999.

[74] A. J. Wagner and J. Yeomans, "Breakdown of scale invariance in the coarsening of phase-separating binary fluids," *Physical Review Letters*, vol. 80, p. 1429, 1998.

[75] H. F. Bohn and W. Federle, "Insect aquaplaning: Nepenthes pitcher plants capture prey with the peristome, a fully wettable water-lubricated anisotropic surface," *Proceedings of the National Academy of Sciences U.S.A*, vol. 101, pp. 14138–14143, 2004.

[76] A. Lafuma and D. Quéré, "Slippery pre-suffused surfaces," *Europhysics Letters*, vol. 96, p. 56001, 2011.

[77] J. D. Smith, R. Dhiman, S. Anand, E. Reza-Garduno, R. E. Cohen, G. H. McKinley, and K. K. Varanasi, "Droplet mobility on lubricant-impregnated surfaces," *Soft Matter*, vol. 9, pp. 1772–1780, 2013.

[78] T.-S. Wong, S. H. Kang, S. K. Tang, E. J. Smythe, B. D. Hatton, A. Grinthal, and J. Aizenberg, "Bioinspired self-repairing slippery surfaces with pressure-stable omniphobicity," *Nature*, vol. 477, p. 443, 2011.

[79] C. Wang and Z. Guo, "A comparison between superhydrophobic surfaces (shs) and slippery liquid-infused porous surfaces (slips) in application," *Nanoscale*, vol. 12, pp. 22398–22424, 2020.

[80] S. Nishimoto and B. Bhushan, "Bioinspired self-cleaning surfaces with superhydrophobicity, superoleophobicity, and superhydrophilicity," *Royal Society of Chemistry Advances*, vol. 3, pp. 671–690, 2013.

[81] C. Huang and Z. Guo, "Fabrications and applications of slippery liquid-infused porous surfaces inspired from nature: A review," *Journal of Bionic Engineering*, vol. 16, pp. 769–793, 2019.

[82] J. D. Smith, R. Dhiman, A. T. Paxson, C. J. Love, B. R. Solomon, and K. K. Varanasi, "Self-lubricating surfaces for food packaging and food processing equipment," Sept. 17 2013. US Patent 8,535,779.

[83] X. Zhou, Y.-Y. Lee, K. S. L. Chong, and C. He, "Superhydrophobic and slippery liquid-infused porous surfaces formed by the self-assembly of a hybrid abc triblock copolymer and their antifouling performance," *Journal of Materials Chemistry B*, vol. 6, pp. 440–448, 2018.

[84] L. Zhao, R. Li, R. Xu, D. Si, Y. Shang, H. Ye, Y. Zhang, H. Ye, and Q. Xin, "Antifouling slippery liquid-infused membrane for separation of water-in-oil emulsions," *Journal of Membrane Science*, vol. 611, p. 118289, 2020.

[85] H. Tsuchiya, M. Tenjimbayashi, T. Moriya, R. Yoshikawa, K. Sasaki, R. Togasawa, T. Yamazaki, K. Manabe, and S. Shiratori, "Liquid-infused smooth surface for improved condensation heat transfer," *Langmuir*, vol. 33, pp. 8950–8960, 2017.

[86] J. Ho, K. Rabbi, S. Sett, T. Wong, and N. Miljkovic, "Dropwise condensation of low surface tension fluids on lubricant-infused surfaces: droplet size distribution and heat transfer," *International Journal of Heat and Mass Transfer*, vol. 172, p. 121149, 2021.

[87] M. J. Kratochvil, M. A. Welsh, U. Manna, B. J. Ortiz, H. E. Blackwell, and D. M. Lynn, "Slippery liquid-infused porous surfaces that prevent bacterial surface fouling and inhibit virulence phenotypes in surrounding planktonic cells," *American Chemical Society Infectious Diseases*, vol. 2, pp. 509–517, 2016.

[88] R. Deng, T. Shen, H. Chen, J. Lu, H.-C. Yang, and W. Li, "Slippery liquid-infused porous surfaces (slipss): a perfect solution to both marine fouling and corrosion?," *Journal of Materials Chemistry A*, vol. 8, pp. 7536–7547, 2020.

[89] M. J. Kreder, J. Alvarenga, P. Kim, and J. Aizenberg, "Design of anti-icing surfaces: smooth, textured or slippery?," *Nature Reviews Materials*, vol. 1, pp. 1–15, 2016.

[90] Y. Long, X. Yin, P. Mu, Q. Wang, J. Hu, and J. Li, "Slippery liquid-infused porous surface (slips) with superior liquid repellency, anti-corrosion, anti-icing and intensified durability for protecting substrates," *Chemical Engineering Journal*, vol. 401, p. 126137, 2020.

[91] S. K. Laney, M. Michalska, T. Li, F. V. Ramirez, M. Portnoi, J. Oh, I. G. Thayne, I. P. Parkin, M. K. Tiwari, and I. Papakonstantinou, "Delayed lubricant depletion of slippery liquid infused porous surfaces using precision nanostructures," *Langmuir*, vol. 37, pp. 10071–10078, 2021.

[92] S. Peppou-Chapman, J. K. Hong, A. Waterhouse, and C. Neto, "Life and death of liquid-infused surfaces: a review on the choice, analysis and fate of the infused liquid layer," *Chemical Society Reviews*, vol. 49, pp. 3688–3715, 2020.

[93] S. Sugathan and S. Bhattacharya, "A phase-field study of elastic stress effects on phase separation in ternary alloys," *Computational Materials Science*, vol. 172, p. 109284, 2020.

[94] M. F. Haase and J. Brujic, "Tailoring of high-order multiple emulsions by the liquid–liquid phase separation of ternary mixtures," *Angewandte Chemie*, vol. 126, pp. 11987–11991, 2014.

[95] H. Zhang, Y. Wu, F. Wang, F. Guo, and B. Nestler, "Phase-field modeling of multiple emulsions via spinodal decomposition," *Langmuir*, vol. 37, pp. 5275–5281, 2021.

[96] X. Cao, W. Li, T. Ma, and H. Dong, "One-step fabrication of polymeric hybrid particles with core–shell, patchy, patchy janus and janus architectures via a microfluidic-assisted phase separation process," *Rsc Advances*, vol. 5, pp. 79969–79975, 2015.

[97] E. E. Ekanem, Z. Zhang, and G. T. Vladisavljevič, "Facile production of biodegradable bipolymer patchy and patchy janus particles with controlled morphology by microfluidic routes," *Langmuir*, vol. 33, pp. 8476–8482, 2017.

[98] S. Bhattacharyya and T. Abinandanan, "A study of phase separation in ternary alloys," *Bulletin of Materials Science*, vol. 26, pp. 193–197, 2003.

[99] L.-q. Chen, "Computer simulation of spinodal decomposition in ternary systems," *Acta Metallurgica et Materialia*, vol. 42, pp. 3503–3513, 1994.

[100] C. Huang, M. O. de La Cruz, and B. Swift, "Phase separation of ternary mixtures: Symmetric polymer blends," *Macromolecules*, vol. 28, pp. 7996–8005, 1995.

[101] R. H. H. Abadi, M. H. Rahimian, and A. Fakhari, "Conservative phase-field lattice-boltzmann model for ternary fluids," *Journal of Computational Physics*, vol. 374, pp. 668–691, 2018.

[102] L. Zheng, S. Zheng, and Q. Zhai, "Reduction-consistent axisymmetric lattice boltzmann equation method for n-phase fluids," *Computers & Fluids*, vol. 218, p. 104857, 2021.

[103] J. Yang and J. Kim, "Numerical study of the ternary cahn–hilliard fluids by using an efficient modified scalar auxiliary variable approach," *Communications in Nonlinear Science and Numerical Simulation*, vol. 102, p. 105923, 2021.

[104] L. Liu and T. Lee, "Wall free energy based polynomial boundary conditions for non-ideal gas lattice boltzmann equation," *International Journal of Modern Physics C*, vol. 20, pp. 1749–1768, 2009.

[105] T. Lee and L. Liu, "Lattice boltzmann simulations of micron-scale drop impact on dry surfaces," *Journal of Computational Physics*, vol. 229, pp. 8045–8063, 2010.

[106] F. Boyer and C. Lapuerta, "Study of a three component cahn-hilliard flow model," *European Series in Applied and Industrial Mathematics: Mathematical Modelling and Numerical Analysis*, vol. 40, pp. 653–687, 2006.

[107] F. Boyer and S. Minjeaud, "Hierarchy of consistent n-component cahn–hilliard systems," *Mathematical Models and Methods in Applied Sciences*, vol. 24, pp. 2885–2928, 2014.

[108] S. Dong, "Wall-bounded multiphase flows of n immiscible incompressible fluids: Consistency and contact-angle boundary condition," *Journal of Computational Physics*, vol. 338, pp. 21–67, 2017.

[109] C. Merkle and C. Rohde, "The sharp-interface approach for fluids with phase change: Riemann problems and ghost fluid techniques," *European Series in Applied and Industrial Mathematics: Mathematical Modelling and Numerical Analysis*, vol. 41, pp. 1089–1123, 2007.

[110] H. Liu, S. Krishnan, S. Marella, and H. Udaykumar, "Sharp interface cartesian grid method ii: A technique for simulating droplet interactions with surfaces of arbitrary shape," *Journal of Computational Physics*, vol. 210, pp. 32–54, 2005.

[111] D. M. Anderson, G. B. McFadden, and A. A. Wheeler, "Diffuse-interface methods in fluid mechanics," *Annual Review of Fluid Mechanics*, vol. 30, pp. 139–165, 1998.

[112] J. Zhu, T. Wang, S. Zhou, Z. Liu, and L. Chen, "Quantitative interface models for simulating microstructure evolution," *Acta Materialia*, vol. 52, no. 4, pp. 833–840, 2004.

[113] B. Li and Y. Zhao, "Variational implicit solvation with solute molecular mechanics: from diffuse-interface to sharp-interface models," *Society for Industrial and Applied Mathematics: Journal on Applied Mathematics*, vol. 73, pp. 1–23, 2013.

[114] G. Son and V. K. Dhir, "Numerical Simulation of Film Boiling Near Critical Pressures With a Level Set Method," *Journal of Heat Transfer*, vol. 120, pp. 183–192, 1998.

[115] J. Strain, "Semi-lagrangian methods for level set equations," *Journal of Computational Physics*, vol. 151, pp. 498–533, 1999.

[116] M. Zhang and X.-L. Deng, "A sharp interface method for sph," *Journal of Computational Physics*, vol. 302, pp. 469–484, 2015.

[117] D. Juric and G. Tryggvason, "Computations of boiling flows," *International Journal of Multiphase Flow*, vol. 24, pp. 387–410, 1998.

[118] J. Hua, J. F. Stene, and P. Lin, "Numerical simulation of 3d bubbles rising in viscous liquids using a front tracking method," *Journal of Computational Physics*, vol. 227, pp. 3358–3382, 2008.

[119] L. Liu, X. Yao, A. Zhang, and Y. Chen, "Numerical analysis of the jet stage of bubble near a solid wall using a front tracking method," *Physics of Fluids*, vol. 29, p. 012105, 2017.

[120] S. W. Welch and J. Wilson, "A volume of fluid based method for fluid flows with phase change," *Journal of Computational Physics*, vol. 160, pp. 662–682, 2000.

[121] M. Renardy, Y. Renardy, and J. Li, "Numerical simulation of moving contact line problems using a volume-of-fluid method," *Journal of Computational Physics*, vol. 171, pp. 243–263, 2001.

[122] N. K. Singh and B. Premachandran, "A coupled level set and volume of fluid method on unstructured grids for the direct numerical simulations of two-phase flows including phase change," *International Journal of Heat and Mass Transfer*, vol. 122, pp. 182–203, 2018.

[123] Y. Sato and B. Ničeno, "A sharp-interface phase change model for a mass-conservative interface tracking method," *Journal of Computational Physics*, vol. 249, pp. 127–161, 2013.

[124] H. Wang, X. Yuan, H. Liang, Z. Chai, and B. Shi, "A brief review of the phase-field-based lattice boltzmann method for multiphase flows," *Capillarity*, vol. 2, pp. 33–52, 2019.

[125] D. Jacqmin, "Calculation of two-phase navier–stokes flows using phase-field modeling," *Journal of Computational Physics*, vol. 155, pp. 96–127, 1999.

[126] W. L. George and J. A. Warren, "A parallel 3d dendritic growth simulator using the phase-field method," *Journal of Computational Physics*, vol. 177, pp. 264–283, 2002.

[127] D. Lee and J. Kim, "Comparison study of the conservative allen–cahn and the cahn–hilliard equations," *Mathematics and Computers in Simulation*, vol. 119, pp. 35–56, 2016.

[128] J.-H. Jeong, N. Goldenfeld, and J. A. Dantzig, "Phase field model for three-dimensional dendritic growth with fluid flow," *Physical Review E*, vol. 64, p. 041602, 2001.

[129] S. Zhang and M. Wang, "A nonconforming finite element method for the cahn–hilliard equation," *Journal of Computational Physics*, vol. 229, pp. 7361–7372, 2010.

[130] J. Hua, P. Lin, C. Liu, and Q. Wang, "Energy law preserving c0 finite element schemes for phase field models in two-phase flow computations," *Journal of Computational Physics*, vol. 230, pp. 7115–7131, 2011.

[131] C. Liu and J. Shen, "A phase field model for the mixture of two incompressible fluids and its approximation by a fourier-spectral method," *Physica D: Nonlinear Phenomena*, vol. 179, pp. 211–228, 2003.

[132] J. Shen and X. Yang, "An efficient moving mesh spectral method for the phase-field model of two-phase flows," *Journal of Computational Physics*, vol. 228, pp. 2978–2992, 2009.

[133] X. He and L.-S. Luo, "Theory of the lattice boltzmann method: From the boltzmann equation to the lattice boltzmann equation," *Physical Review E*, vol. 56, p. 6811, 1997.

[134] C. K. Aidun and J. R. Clausen, "Lattice-boltzmann method for complex flows," *Annual Review of Fluid Mechanics*, vol. 42, pp. 439–472, 2010.

[135] A. Fakhari and M. H. Rahimian, "Phase-field modeling by the method of lattice boltzmann equations," *Physical Review E*, vol. 81, p. 036707, 2010.

[136] V. Khatavkar, P. Anderson, P. Duineveld, and H. Meijer, "Diffuse-interface modelling of droplet impact," *Journal of Fluid Mechanics*, vol. 581, pp. 97–127, 2007.

[137] M. Brinkmann and R. Lipowsky, "Wetting morphologies on substrates with striped surface domains," *Journal of Applied Physics*, vol. 92, pp. 4296–4306, 2002.

[138] H. Kusumaatmaja and R. Lipowsky, "Equilibrium morphologies and effective spring constants of capillary bridges," *Langmuir*, vol. 26, pp. 18734–18741, 2010.

[139] C. Semprebon, G. McHale, and H. Kusumaatmaja, "Apparent contact angle and contact angle hysteresis on liquid infused surfaces," *Soft Matter*, vol. 13, pp. 101–110, 2017.

[140] M. S. Sadullah, C. Semprebon, and H. Kusumaatmaja, "Drop dynamics on liquid-infused surfaces: The role of the lubricant ridge," *Langmuir*, vol. 34, pp. 8112–8118, 2018.

[141] M. S. Sadullah, G. Launay, J. Parle, R. Ledesma-Aguilar, Y. Gizaw, G. McHale, G. G. Wells, and H. Kusumaatmaja, "Bidirectional motion of droplets on gradient liquid infused surfaces," *Communications Physics*, vol. 3, pp. 1–7, 2020.

[142] M. J. Kreder, D. Daniel, A. Tetreault, Z. Cao, B. Lemaire, J. V. Timonen, and J. Aizenberg, "Film dynamics and lubricant depletion by droplets moving on lubricated surfaces," *Physical Review X*, vol. 8, p. 031053, 2018.

[143] D. Daniel, J. V. Timonen, R. Li, S. J. Velling, and J. Aizenberg, "Oleoplaning droplets on lubricated surfaces," *Nat. Phys.*, vol. 13, pp. 1020–1025, 2017.

[144] K. A. Brakke, "The surface evolver," *Experimental Mathematics*, vol. 1, pp. 141–165, 1992.

[145] K. A. Brakke, "The surface evolver and the stability of liquid surfaces," *Philosophical Transactions of the Royal Society of London. Series A: Mathematical, Physical and Engineering Sciences*, vol. 354, pp. 2143–2157, 1996.

[146] C. Semprebon, T. Krüger, and H. Kusumaatmaja, "Ternary free-energy lattice boltzmann model with tunable surface tensions and contact angles," *Physical Review E*, vol. 93, p. 033305, 2016.

[147] J. R. Panter, *Exploring Stability Landscapes for Optimal Material Design: Application to Wetting of Structured Surfaces.* PhD thesis, Durham University, 2019.

[148] A. J. Ladd, "Numerical simulations of particulate suspensions via a discretized boltzmann equation. part 1. theoretical foundation," *Journal of Fluid Mechanics*, vol. 271, pp. 285–309, 1994.

[149] A. J. Ladd, "Numerical simulations of particulate suspensions via a discretized boltzmann equation. part 2. numerical results," *Journal of Fluid Mechanics*, vol. 271, pp. 311–339, 1994.

[150] L. Hao and P. Cheng, "Lattice boltzmann simulations of liquid droplet dynamic behavior on a hydrophobic surface of a gas flow channel," *Journal of Power Sources*, vol. 190, pp. 435–446, 2009.

[151] Q. Lou, Z. Guo, and B. Shi, "Evaluation of outflow boundary conditions for two-phase lattice boltzmann equation," *Physical Review E*, vol. 87, p. 063301, 2013.

[152] A. Klingner, J. Buehrle, and F. Mugele, "Capillary bridges in electric fields," *Langmuir*, vol. 20, pp. 6770–6777, 2004.

[153] D. J. Broesch and J. Frechette, "From concave to convex: capillary bridges in slit pore geometry," *Langmuir*, vol. 28, pp. 15548–15554, 2012.

[154] L. Wang and T. J. McCarthy, "Capillary-bridge–derived particles with negative gaussian curvature," *Proceedings of the National Academy of Sciences U.S.A*, vol. 112, pp. 2664–2669, 2015.

[155] M. M. Kohonen, D. Geromichalos, M. Scheel, C. Schier, and S. Herminghaus, "On capillary bridges in wet granular materials," *Physica A*, vol. 339, pp. 7–15, 2004.

[156] A. De Lazzer, M. Dreyer, and H. Rath, "Particle- surface capillary forces," *Langmuir*, vol. 15, pp. 4551–4559, 1999.

[157] O. Pakarinen, A. Foster, M. Paajanen, T. Kalinainen, J. Katainen, I. Makkonen, J. Lahtinen, and R. Nieminen, "Towards an accurate description of the capillary force in nanoparticle-surface interactions," *Modelling and Simulation in Materials Science and Engineering*, vol. 13, p. 1175, 2005.

[158] N. Mitarai and F. Nori, "Wet granular materials," *Advances in Physics*, vol. 55, pp. 1–45, 2006.

[159] M. Scheel, R. Seemann, M. Brinkmann, M. Di Michiel, A. Sheppard, B. Breidenbach, and S. Herminghaus, "Morphological clues to wet granular pile stability," *Nature Materials*, vol. 7, p. 189, 2008.

[160] L. Xu, A. Lio, J. Hu, D. F. Ogletree, and M. Salmeron, "Wetting and capillary phenomena of water on mica," *The Journal of Physical Chemistry B*, vol. 102, pp. 540–548, 1998.

[161] X. Xiao and L. Qian, "Investigation of humidity-dependent capillary force," *Langmuir*, vol. 16, pp. 8153–8158, 2000.

[162] Z. Wei and Y.-P. Zhao, "Growth of liquid bridge in afm," *Journal of Physics D: Applied Physics*, vol. 40, p. 4368, 2007.

[163] R. G. Beutel and S. Gorb, "Ultrastructure of attachment specializations of hexapods (arthropoda): evolutionary patterns inferred from a revised ordinal phylogeny," *Journal of Zoological Systematics and Evolutionary Research*, vol. 39, pp. 177–207, 2001.

[164] W. Federle, E. L. Brainerd, T. A. McMahon, and B. Hölldobler, "Biomechanics of the movable pretarsal adhesive organ in ants and bees," *Proceedings of the National Academy of Sciences U.S.A*, vol. 98, pp. 6215–6220, 2001.

[165] M. Prakash, D. Quéré, and J. W. Bush, "Surface tension transport of prey by feeding shorebirds: the capillary ratchet," *Science*, vol. 320, pp. 931–934, 2008.

[166] M. Nosonovsky and B. Bhushan, "Capillary effects and instabilities in nanocontacts," *Ultramicroscopy*, vol. 108, pp. 1181–1185, 2008.

[167] J. Zhuang and Y. S. Ju, "A combined experimental and numerical modeling study of the deformation and rupture of axisymmetric liquid bridges under coaxial stretching," *Langmuir*, vol. 31, pp. 10173–10182, 2015.

[168] S. Banerjee, P. Mulder, J. M. Kleijn, and M. A. Cohen Stuart, "Effect of surface roughness and softness on water capillary adhesion in apolar media," *The Journal of Physical Chemistry A*, vol. 116, pp. 6481–6488, 2012.

[169] J. Gui and B. Marchon, "A stiction model for a head-disk interface of a rigid disk drive," *Journal of Applied Physics*, vol. 78, pp. 4206–4217, 1995.

[170] X.-M. Li, D. Reinhoudt, and M. Crego-Calama, "What do we need for a superhydrophobic surface? a review on the recent progress in the preparation of superhydrophobic surfaces," *Chemical Society Reviews*, vol. 36, pp. 1350–1368, 2007.

[171] P. Kim, T.-S. Wong, J. Alvarenga, M. J. Kreder, W. E. Adorno-Martinez, and J. Aizenberg, "Liquid-infused nanostructured surfaces with extreme anti-ice and anti-frost performance," *American Chemical Society Nano*, vol. 6, pp. 6569–6577, 2012.

[172] S. Anand, A. T. Paxson, R. Dhiman, J. D. Smith, and K. K. Varanasi, "Enhanced condensation on lubricant-impregnated nanotextured surfaces," *American Chemical Society Nano*, vol. 6, pp. 10122–10129, 2012.

[173] J. S. Wexler, I. Jacobi, and H. A. Stone, "Shear-driven failure of liquid-infused surfaces," *Physical Review Letter*, vol. 114, p. 168301, 2015.

[174] M. Villegas, Y. Zhang, N. Abu Jarad, L. Soleymani, and T. F. Didar, "Liquid-infused surfaces: A review of theory, design, and applications," *American Chemical Society Nano*, vol. 13, pp. 8517–8536, 2019.

[175] F. Schellenberger, J. Xie, N. Encinas, A. Hardy, M. Klapper, P. Papadopoulos, H.-J. Butt, and D. Vollmer, "Direct observation of drops on slippery lubricant-infused surfaces," *Soft Matter*, vol. 11, pp. 7617–7626, 2015.

[176] G. McHale, B. V. Orme, G. G. Wells, and R. Ledesma-Aguilar, "Apparent contact angles on lubricant-impregnated surfaces/slips: From superhydrophobicity to electrowetting," *Langmuir*, vol. 35, pp. 4197–4204, 2019.

[177] P. Roach, N. J. Shirtcliffe, and M. I. Newton, "Progess in superhydrophobic surface development," *Soft Matter*, vol. 4, pp. 224–240, 2008.

[178] D. Quéré, "Wetting and roughness," *Annual Review of Materials Research*, vol. 38, pp. 71–99, 2008.

[179] W. Aouad, J. Landel, S. B. Dalziel, J. Davidson, and D. Wilson, "Particle image velocimetry and modelling of horizontal coherent liquid jets impinging on and draining down a vertical wall," *Experimental Thermal and Fluid Science*, vol. 74, pp. 429–443, 2016.

[180] A. J. Prosser and E. I. Franses, "Adsorption and surface tension of ionic surfactants at the air–water interface: review and evaluation of equilibrium models," *Colloids and Surfaces A: Physicochemical and Engineering Aspects*, vol. 178, pp. 1–40, 2001.

[181] D. Peregrine and S. Kalliadasis, "Filling flows, cliff erosion and cleaning flows," *Journal of Fluid Mechanics*, vol. 310, pp. 365–374, 1996.

[182] J. Eggers, "Nonlinear dynamics and breakup of free-surface flows," *Reviews of modern physics*, vol. 69, p. 865, 1997.

[183] J. J. Higdon, "Stokes flow in arbitrary two-dimensional domains: shear flow over ridges and cavities," *Journal of Fluid Mechanics*, vol. 159, pp. 195–226, 1985.

[184] D. Hartley and W. Murgatroyd, "Criteria for the break-up of thin liquid layers flowing isothermally over solid surfaces," *International Journal of Heat and Mass Transfer*, vol. 7, pp. 1003–1015, 1964.

[185] A. Gupta and S. Basu, "Deformation of an oil droplet on a solid substrate in simple shear flow," *Chemical engineering science*, vol. 63, pp. 5496–5502, 2008.

[186] G. Hassan, B. S. Yilbas, A. Al-Sharafi, and H. Al-Qahtani, "Self-cleaning of a hydrophobic surface by a rolling water droplet," *Scientific reports*, vol. 9, pp. 1–14, 2019.

[187] M. J. Rosen and J. T. Kunjappu, *Surfactants and interfacial phenomena*. John Wiley & Sons, 2012.

[188] D. Bajpai, "Laundry detergents: an overview," *Journal of oleo science*, vol. 56, pp. 327–340, 2007.

[189] J.-F. Yan, A. E. Sáez, and C. S. Grant, "Removal of oil films from stainless steel tubes," *AIChE journal*, vol. 43, pp. 251–259, 1997.

[190] P. Boomkamp and R. Miesen, "Classification of instabilities in parallel two-phase flow," *International Journal of Multiphase Flow*, vol. 22, pp. 67–88, 1996.

[191] M. J. Scott and M. N. Jones, "The biodegradation of surfactants in the environment," *Biochimica et Biophysica Acta (BBA)-Biomembranes*, vol. 1508, pp. 235–251, 2000.

[192] E. Olkowska, Z. Polkowska, and J. Namiesnik, "Analytics of surfactants in the environment: problems and challenges," *Chemical Reviews*, vol. 111, pp. 5667–5700, 2011.

[193] G. B. Beekman, "Water conservation, recycling and reuse," *International Journal of Water Resources Development*, vol. 14, pp. 353–364, 1998.

[194] S. Koop, A. Van Dorssen, and S. Brouwer, "Enhancing domestic water conservation behaviour: A review of empirical studies on influencing tactics," *Journal of Environmental Management*, vol. 247, pp. 867–876, 2019.

[195] D. Saurí, "Water conservation: Theory and evidence in urban areas of the developed world," *Annual Review of Environment and Resources*, vol. 38, pp. 227–248, 2013.

[196] A. Boretti and L. Rosa, "Reassessing the projections of the world water development report," *NPJ Clean Water*, vol. 2, pp. 1–6, 2019.

[197] P. W. Mayer, "Water research foundation study documents water conservation potential and more efficiency in households," *Journal-American Water Works Association*, vol. 108, pp. 31–40, 2016.

[198] T. Ivanković and J. Hrenović, "Surfactants in the environment," *Arh Hig Rada Toksikol*, vol. 61, pp. 95–110, 2010.

[199] M. Patel, A. Theiß, and E. Worrell, "Surfactant production and use in germany: resource requirements and co2 emissions," *Resources, Conservation and Recycling*, vol. 25, pp. 61–78, 1999.

[200] A. M. Edwards, R. Ledesma-Aguilar, M. I. Newton, C. V. Brown, and G. McHale, "Not spreading in reverse: The dewetting of a liquid film into a single drop," *Science Advances*, vol. 2, p. e1600183, 2016.

[201] S. Kim, J. Kim, and H.-Y. Kim, "Dewetting of liquid film via vapour-mediated marangoni effect," *Journal of Fluid Mechanics*, vol. 872, pp. 100–114, 2019.

[202] M. Baglioni, T. Guaragnone, R. Mastrangelo, F. H. Sekine, T. Ogura, and P. Baglioni, "Nonionic surfactants for the cleaning of works of art: insights on acrylic polymer films dewetting and artificial soil removal," *American Chemical Society applied materials & interfaces*, vol. 12, pp. 26704–26716, 2020.

[203] J. Nocedal, "Updating quasi-Newton matrices with limited storage," *Mathematics of Computation*, vol. 35, pp. 773–782, 1980.

[204] D. Liu and J. Nocedal, "On the limited memory BFGS method for large scale optimization," *Mathematical Programming*, vol. 45, pp. 503–528, 1989.

[205] W. E, W. Ren, and E. Vanden-Eijnden, "Simplified and improved string method for computing the minimum energy paths in barrier-crossing events," *The Journal of Chemical Physics*, vol. 126, p. 164103, 2007.

[206] N. Wang, C. Semprebon, H. Liu, C. Zhang, and H. Kusumaatmaja, "Modelling double emulsion formation in planar flow-focusing microchannels," *Journal of Fluid Mechanics*, vol. 895, 2020.

[207] J. Bostwick and P. Steen, "Stability of constrained capillary surfaces," *Annual Review of Fluid Mechanics*, vol. 47, pp. 539–568, 2015.

[208] D. M. Slater, M. J. Vogel, A. M. Macner, and P. H. Steen, "Beetle-inspired adhesion by capillary-bridge arrays: pull-off detachment," *Journal of Adhesion Science and Technology*, vol. 28, pp. 273–289, 2014.

[209] T. P. Farmer and J. C. Bird, "Asymmetric capillary bridges between contacting spheres," *Journal of Colloid and Interface Science*, vol. 454, pp. 192–199, 2015.

[210] Y. Wang, S. Michielsen, and H. J. Lee, "Symmetric and asymmetric capillary bridges between a rough surface and a parallel surface," *Langmuir*, vol. 29, pp. 11028–11037, 2013.

[211] V. Narasimhan, R. H. Siddique, J. O. Lee, S. Kumar, B. Ndjamen, J. Du, N. Hong, D. Sretavan, and H. Choo, "Multifunctional biophotonic nanostructures inspired by the longtail glasswing butterfly for medical devices," *Nature Nanotechnology*, vol. 13, pp. 512–519, 2018.

[212] Z. Chen, Z. Zhang, Y. Wang, D. Xu, and Y. Zhao, "Butterfly inspired functional materials," *Materials Science and Engineering: R: Reports*, vol. 144, p. 100605, 2021.

[213] A. Allabar and M. Nowak, "Message in a bottle: Spontaneous phase separation of hydrous vesuvius melt even at low decompression rates," *Earth and Planetary Science Letters*, vol. 501, pp. 192–201, 2018.

[214] C. E. De Ronde, S. E. Humphris, T. W. Höfig, A. G. Reyes, and I. E. . Scientists, "Critical role of caldera collapse in the formation of seafloor mineralization: The case of brothers volcano," *Geology*, vol. 47, pp. 762–766, 2019.

[215] S. Alberti, "Phase separation in biology," *Current Biology*, vol. 27, pp. R1097–R1102, 2017.

[216] H. B. Schmidt and D. Görlich, "Transport selectivity of nuclear pores, phase separation, and membraneless organelles," *Trends in Biochemical Sciences*, vol. 41, pp. 46–61, 2016.

[217] N. A. Verhaegh, J. S. van Duijneveldt, J. K. Dhont, and H. N. Lekkerkerker, "Fluid-fluid phase separation in colloid-polymer mixtures studied with small angle light scattering and light microscopy," *Physica A: Statistical Mechanics and its Applications*, vol. 230, pp. 409–436, 1996.

[218] H. Tanaka, "Interplay between wetting and phase separation in binary fluid mixtures: roles of hydrodynamics," *Journal of Physics: Condensed Matter*, vol. 13, p. 4637, 2001.

[219] M. E. Cates and E. Tjhung, "Theories of binary fluid mixtures: from phase-separation kinetics to active emulsions," *Journal of Fluid Mechanics*, vol. 836, 2018.

[220] G. Pätzold and K. Dawson, "Numerical simulation of phase separation in the presence of surfactants and hydrodynamics," *Physical Review E*, vol. 52, p. 6908, 1995.

[221] R. Matas-Navarro, R. Golestanian, T. B. Liverpool, and S. M. Fielding, "Hydrodynamic suppression of phase separation in active suspensions," *Physical Review E*, vol. 90, p. 032304, 2014.

[222] H. Wang and R. J. Composto, "Thin film polymer blends undergoing phase separation and wetting: Identification of early, intermediate, and late stages," *The Journal of Chemical Physics*, vol. 113, pp. 10386–10397, 2000.

[223] H.-J. Chung, A. Taubert, R. Deshmukh, and R. J. Composto, "Mobile nanoparticles and their effect on phase separation dynamics in thin-film polymer blends," *Europhysics Letters*, vol. 68, p. 219, 2004.

[224] S. Reich and Y. Cohen, "Phase separation of polymer blends in thin films," *Journal of Polymer Science: Polymer Physics Edition*, vol. 19, pp. 1255–1267, 1981.

[225] Y. Chao, S. Y. Mak, S. Rahman, S. Zhu, and H. C. Shum, "Generation of high-order all-aqueous emulsion drops by osmosis-driven phase separation," *Small*, vol. 14, p. 1802107, 2018.

[226] S. Park, S. S. Lee, and S.-H. Kim, "Photonic multishells composed of cholesteric liquid crystals designed by controlled phase separation in emulsion drops," *Advanced Materials*, vol. 32, p. 2002166, 2020.

[227] H. Tanaka and T. Araki, "Spontaneous double phase separation induced by rapid hydrodynamic coarsening in two-dimensional fluid mixtures," *Physical Review Letters*, vol. 81, p. 389, 1998.

[228] T. Rogers and R. C. Desai, "Numerical study of late-stage coarsening for off-critical quenches in the cahn-hilliard equation of phase separation," *Physical Review B*, vol. 39, p. 11956, 1989.

[229] M. Tateno and H. Tanaka, "Power-law coarsening in network-forming phase separation governed by mechanical relaxation," *Nature Communications*, vol. 12, pp. 1–12, 2021.

[230] E. D. Siggia, "Late stages of spinodal decomposition in binary mixtures," *Physical review A*, vol. 20, no. 2, p. 595, 1979.

[231] G. Launay, M. S. Sadullah, G. McHale, R. Ledesma-Aguilar, H. Kusumaatmaja, and G. G. Wells, "Self-propelled droplet transport on shaped-liquid surfaces," *Scientific Reports*, vol. 10, pp. 1–8, 2020.

[232] R. Peeters, H. Vanderschaeghe, J. Rongé, and J. A. Martens, "Energy performance and climate dependency of technologies for fresh water production from atmospheric water vapour," *Environmental Science: Water Research & Technology*, vol. 6, pp. 2016–2034, 2020.

[233] N. Robertson, D. Sanders, P. Seymour, and R. Thomas, "The four-colour theorem," *Journal of Combinatorial Theory, Series B*, vol. 70, pp. 2–44, 1997.

[234] J. Kim, "Phase-field models for multi-component fluid flows," *Communications in Computational Physics*, vol. 12, pp. 613–661, 2012.